ESTIMATION OF PARAMETERS OF DYNAMIC LOAD MODELS FOR VOLTAGE STABILITY STUDIES

A thesis submitted to The University of Manchester for the degree of

Doctor of Philosophy

In the Faculty of Engineering and Physical Science

2012

PAWEL REGULSKI

SCHOOL OF ELECTRICAL AND ELECTRONIC ENGINEERING

Table of Contents

Final Count: 32,600

List of Figures

List of Tables

List of Abbreviations

AI	Artificial Intelligence
AVR	Automatic Voltage Regulator
CL	Composite Load
CPU	Central Processing Unit
DFT	Discrete Fourier Transform
EKF	Extended Kalman Filter
EL	Exponential Load
ERL	Exponential Recovery Load
FIR	Finite Impulse Response
GA	Genetic Algorithm
HV	High Voltage
IDFT	Interpolated Discrete Fourier Transform
IM	Induction Motor
IPSO	Improved Particle Swarm Optimization
KF	Kalman Filter
LS	Least Squares
LV	Low Voltage
NLS	Nonlinear Least Squares
NTA	Newton-Type Algorithm
OLTC	On-Load Tap Changer
OXL	Over-Excitation Limiter
PSO	Particle Swarm Optimization
RMS	Root Mean Square
STLS	Self-Tuning Least Squares
UKF	Unscented Kalman Filter
UT	Unscented Transform
WAMS	Wide Area Monitoring Systems

Abstract

The University of Manchester
Faculty of Engineering and Physical Science

PhD Thesis
Estimation of Parameters of Dynamic Load Models for Voltage Stability Studies

Pawel Regulski
May, 2012

Current environmental and economic trends have forced grid operators to maximize the utilization of the existing assets, which is causing systems to be operated closer to their stability limits than ever before. This requires, among other things, better knowledge and modelling of the existing power system equipment to increase the accuracy of the assessment of current stability margins.

This research investigates the possibility of improving the quality of load modeling. The thesis presents a review of the traditional methods for estimation of load model parameters and proposes to use Improved Particle Swarm Optimization. Different algorithms are tested and compared in terms of accuracy, reliability and CPU requirements using computer simulations and real-data captured in a power system.

Estimation of frequency and power components has also been studied in this thesis. A review of the existing methods has been provided and the use of an Unscented Kalman Filter proposed. This nonlinear recursive algorithm has been thoroughly tested and compared against selected traditional techniques in a number of experiments involving computer-generated signals as well as measurements obtained in laboratory conditions.

Declaration

No portion of the work referred to in the thesis has been submitted in support of an application for another degree or qualification of this or any other university or other institute of learning.

Copyright Statement

To Karolina and my family

Acknowledgements

I would like to thank my supervisor, Prof. Vladimir Terzija, for his help and guidance throughout my PhD studies.

Special thanks to my colleagues for all those long inspirational discussions that helped me gain a broader view not only of science but also of life.

Finally, I would like to thank my parents and my fiancée Karolina for all their support and encouragement when I needed it the most.

1. Introduction

1.1. Voltage Stability

In the past the issue of Voltage Instability was mostly associated with weak systems and long lines. However, the problem has now begun to occur in highly developed networks due to the ever increasing load placed on power systems [1]. What is more, current environmental and economic trends have forced grid operators to maximize the utilization of the existing assets, which is causing systems to be operated closer to their stability limits than ever before [2]. This requires, among other things, better knowledge and modelling of the existing power system equipment to increase the accuracy of the assessment of current stability margins.

As described in [1], *Voltage Stability is the ability of a power system to maintain steady acceptable voltages at all busses in the system under normal conditions and after being subjected to a disturbance*. Furthermore, the following condition must be satisfied: at a given operating point for every bus in the system, bus voltage magnitude increases as the reactive power injection is increased [1]. This definition shows that Voltage Stability is directly related to the reactive power demand at a given bus. In [3] Voltage Instability is defined as *an attempt of load dynamics to restore power consumption beyond the capabilities of the combined transmission and generation system*. For this reason Voltage Instability is also called Load Instability, to emphasize the particular contribution of loads to this phenomenon. This contribution has been addressed in [3]-[15].

A system is considered voltage unstable if any bus has a negative Q-V characteristic. Therefore, in general, voltage instability is a local phenomenon. However, a more complex and dangerous scenario involving voltage instability is known as Voltage Collapse [1], [3]. This scenario involves a sequence of events that lead to a low voltage profile in a significant part of a power system and may eventually cause a blackout.

1.2. Load Modelling

The work produced in the field of Load Modelling addresses the issues related to the representation of power system loads in computer simulations and stability analysis. The application of this work is not limited to Voltage Stability, although it does receive the majority of the attention due to the strong relationship between reactive power demand and voltage. In [16]-[19] it is shown that the behaviour of power system loads also has an impact on transient stability and [14] demonstrates the influence of loads on under voltage load shedding. Moreover, knowledge of load characteristics may be invaluable for utilities during planning and expansion of distribution networks.

In general, the modelling of loads can be divided into two stages: selection of the appropriate models and determination of their parameters. A particularly practical approach to this process is offered by the measurement-based approach [23]-[41]. This technique employs different estimation tools to extract useful information about power system loads from measurements of voltage and current taken in the field. In other words, these field measurements are used to tune parameters of an assumed load model to minimize the difference between the model output and the measurements (curve fitting approach).

One of the current trends in power system development is an increase in the number of intelligent electronic devices deployed in the system. This includes the newly emerging Wide Area Monitoring Systems (WAMS) [42], [43], which are capable of concentrating huge quantities of measurement data in real-time. Such archives of measurement data could serve as an invaluable resource for the estimation of load model parameters, by providing detailed information about load behaviour and characteristics under different operating conditions. The process for determining load model parameters from field measurements is depicted in Figure 1-1, where the subscript *m* denotes the measurements and the subscript *e* denotes the values estimated by the model.

Selection of a load model depends on the expected nature of the load which is being estimated and on the time frame of interest. For example, loads which tend to reach a new steady state immediately after a disturbance in the system can be approximated with a simple static model like the well known polynomial or exponential models [1], [3]. However, the main concern in the field of load modelling is the accurate modelling of loads that tend to recover power over an extended time frame. This phenomenon requires dynamic models, which can accurately imitate the behaviour of such loads [4]-[7].

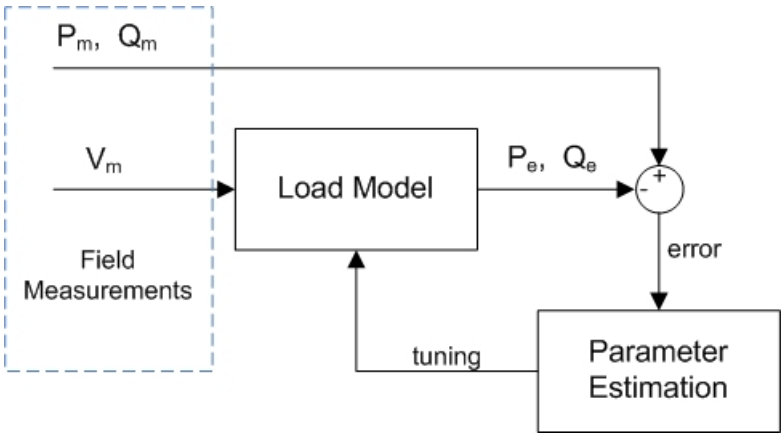

Figure 1-1: Block diagram of measurement-based load modelling

Voltage dependent dynamic load models are more complex than static models and for this reason satisfactory parameter estimation for these models is more challenging. Traditionally, the Nonlinear Least Squares (NLS) method [28]-[33] has been employed to find the unknown parameter values of a load model. However, this algorithm, being a local minimizer, is very sensitive to the initial guess of the parameter values. For this reason, Artificial Intelligence (AI) techniques [19]-[22] have recently received significant attention, since they are better at solving complex optimization problems than NLS methods. Genetic Algorithms (GA) are the most popular of the AI techniques [20], [21]. However, this method struggles with issues like premature convergence and weak fine-tuning properties. Hybrid methods [23]-[27] have been introduced in an attempt to overcome these problems. These Hybrid methods combine the global searching abilities of GA with the speed and accuracy of NLS. A drawback of this is approach is that, despite the considerable improvement in the results, the final solution still depends upon the reliability of GA, and this property

of GA is not always acceptable. For this reason there is still room for improvement in this field.

1.3. System Measurements

The measurement-based approach to load modelling requires field measurements of voltage and current to perform the estimation of the unknown model parameters (Figure 1-1). However, the procedures developed use *RMS* values of *P*, *Q* and *V*, which means that the instantaneous voltage and current measured in the system need to be processed before the estimation can be performed. Figure 1-2 shows a single-line diagram of a configuration in which the measurements are taken.

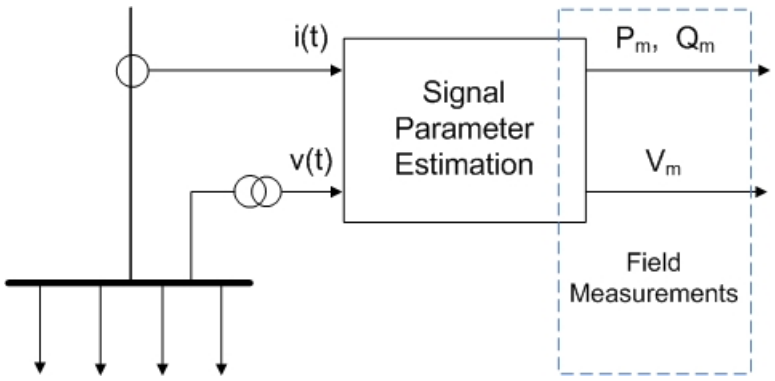

Figure 1-2: Block diagram of measurement configuration

From Figure 1-1 and Figure 1-2 it is clear that measurement-based load modelling will be very sensitive to the signal processing of the measurements. This means that the quality of the tracking of the signal parameters will affect the accuracy with which the unknown parameters of the load models can be estimated.

Traditionally, the magnitude of a sinusoidal signal has been obtained using the Discrete Fourier Transform (DFT), the Least Squares (LS) method or the Kalman Filter (KF) [44]-[47]. The biggest shortcoming of these approaches is the assumption of a constant fundamental frequency (50Hz or 60Hz), which is not valid in practical applications. During system frequency deviations these methods introduce a significant error in to the estimated signal parameters. To overcome these problems new approaches have been proposed, like the Extended Kalman Filter (EKF) [48], the Interpolated DFT [49], [50], the Newton-type algorithm (NTA) [51], [52], the

Nonlinear Least Squares (NLS) method [53], the maximum likelihood method [54], [55] or methods based on adaptive Finite Impulse Response (FIR) filtering [56]-[60]. In this way, the sensitivity to frequency deviations has been limited or even eliminated. Still, most of the methods introduce a delay, related to the observation window, which is usually greater than the length of the fundamental period.

1.4. Aims of the Research

The first goal of this reasearch was to investigate and possibly improve the reliability and accuracy of the estimation of load model parameters. Accurate modelling of power system loads may be one of the key factors in satisfying the demands imposed by the current environmental and economical trends, where the intention is to push the system closer to its stability limits and utilize the existing reserve instead of building new transmission lines, in a secure fashion.

The second aim of the project was to develop a method that ensures accurate estimation of power components, which are required in the process of extracting the parameters of load models from field measurements. The proposed method should also be applicable in real-time to enable future implementation in devices such as Phasor Measurement Units (PMU) [2], [42], [43].

1.5. Methodology

Both of the problems tackled in this project are very similar in nature – namely, the estimation of parameters of a model based on observed data. Figure 1-3 presents a block diagram of how the work has been carried out. The observed data consists of measurements captured in a substation or under laboratory conditions as well as simulated data obtained from the DIgSILENT PowerFactory software [61]. These measurements, being saved either in an MS Excel spreadsheet or a comtrade file [62], consist of columns of uniformly sampled data with time-tags. The data is then imported to Matlab [63], where all the numerical algorithms have been implemented. This includes initial data preparation (trimming, normalization), filtering (e. g.

moving average filter) as well as visualization of the results (plotting). The core of the work consists of the implementation of all the tested methods in Matlab.

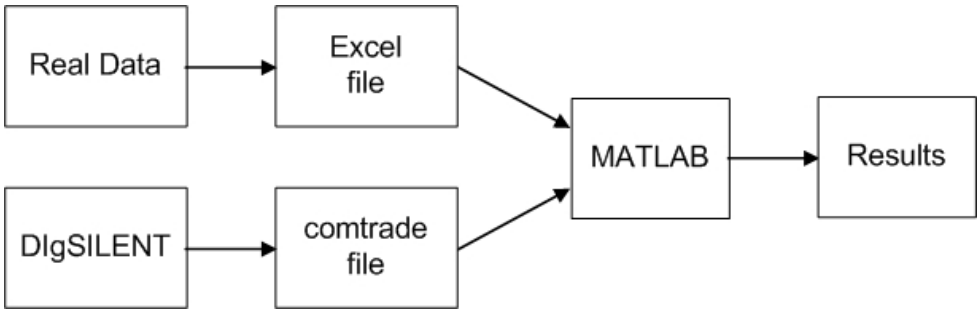

Figure 1-3: Methodology of research

1.6. Contribution

The main contribution of this thesis consists of:

- Estimation of Signal Model Parameters:
  - proposal of a simple state-space model for the instantaneous power signal model
  - implementation of the Unscented Kalman Filter for the fast tracking of power components and frequency

- Estimation of Load Model Parameters:
  - application of the Improved Particle Swarm Optimization for the estimation of load model parameters
  - assessment of the reliability of IPSO and other traditionally used estimation methods

1.7. Outline of the Thesis

Chapter 1 briefly describes the problems tackled in the thesis. It gives a short overview of parameter estimation for a sinusoidal signal, measurement-based load modelling and emphasizes the importance of the latter in voltage stability.

Chapter 2 explains in more detail the phenomenon of voltage stability, emphasising in particular the contribution of loads. Basic ideas and definitions are provided, including an explanation of dynamic and static load characteristics. Then, this theory is demonstrated using computer simulations of a 10-bus test system in DIgSILENT.

Chapter 3 is devoted to the estimation of power components and frequency based on the instantaneous power signal. A recursive method is proposed, thoroughly tested in a number of experiments and then compared against two other methods using computer simulations and measurements obtained under laboratory conditions.

Chapter 4 focuses on the estimation of load model parameters. An AI method is proposed and tested using two dynamic load models of different complexity. The results are compared against two traditional methods in terms of reliability and accuracy using computer simulations and real-data obtained at a substation.

Chapter 5 provides final conclusions and recommendations for possible future work

2. Loads and Voltage Stability

2.1. Introduction

In general, voltage instability can be described as the inability of the combined generation and transmission system to meet the load demand. For this reason the phenomenon can be considered to be load-driven. Additionally, loads are an element that is beyond the control of the network operator. It is the customer who decides the size of the load and when it is connected. Of course, in extreme cases, protection devices may take action and shed some load. However, this is to prevent the system from transitioning to a much more severe state (e. g. uncontrolled islanding, blackout) and it is not used to control the network during normal operation.

In addition, the parameters of the system's elements are usually known or can be easily determined. Parameters of loads on the other hand are most often unknown and they can change in a wide range over time (from daily to seasonal deviations) and for this reason loads are very challenging in terms of modelling. At this moment, loads are one of the variables the determination of which could help maximize the utilization of the available assets and push the system operation closer to its stability limits without increasing the risk of a cascading event. This chapter will show how different types of loads behave and how they can affect the voltage profile of the system.

2.2. Maximum Power Transfer

This section introduces an important concept of Maximum Power Transfer and explains how it relates to the Voltage Stability of a power system. For simplicity, a single-load infinite-bus system is assumed. It can be treated as a Thevenin equivalent of the network as seen from the load bus [3]. Generation is represented as an AC voltage source E with constant amplitude and frequency and the transmission line is modelled as an impedance $Z = R + jX$. Shunt capacitance is ignored for simplicity. Figure 2-1 depicts a single-line diagram of the above described circuit.

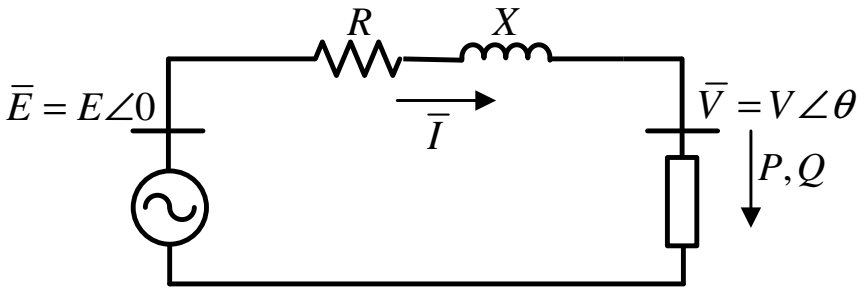

Figure 2-1: Representation of a single-load infinite-bus system

Additionally, the load power factor is defined as follows:

$$PF = \frac{P}{S} = \frac{P}{\sqrt{P^2 + Q^2}} = \cos\varphi \tag{2.1}$$

where P, Q and S are the active, reactive and apparent powers and φ is the angle between the vectors of active and apparent powers. Now, assuming a constant power factor, the load can be defined in the following way:

$$Z_l = R_l + jX_l = R_l + jR_l \tan\varphi \tag{2.2}$$

It should be noted that without defining a constant power factor, equation (2.2) would have had two variables with respect to which the power transfer could be maximized. As shown in [3], this approach would yield an unrealistic solution in which the load resistance is equal to the transmission system's resistance and the load reactance is equal to the negative transmission system's reactance. Taking into account that, in practice, the transmission system's impedance is dominated by reactance, the same thing would apply to the load and this would result in a negligible active power transfer.

The current flowing through the circuit depicted in Figure 2-1 is defined as:

$$\bar{I} = \frac{\bar{E}}{(R + R_l) + j(X + R_l \tan\varphi)} \tag{2.3}$$

and the active power consumed by the load is defined as:

$$P = R_l I^2 = \frac{R_l E^2}{(R + R_l)^2 + (X + R_l \tan\varphi)^2} \tag{2.4}$$

To find the desired extremum (maximum power transfer) the following condition needs to be fulfilled:

$$\frac{\partial P}{\partial R_l} = 0 \tag{2.5}$$

which, after some calculations, gives:

$$R_l^2 + R_l^2 \tan^2\varphi = R^2 + X^2 \tag{2.6}$$

and this is equivalent to:

$$|Z_l| = |Z| \tag{2.7}$$

This solution shows that the maximum power transfer will occur when the magnitude of the load impedance is equal to the magnitude of the network's impedance, which means that the optimal load resistance and reactance are given by:

$$R_{lmaxP} = |Z|\cos\varphi \tag{2.8}$$

$$X_{lmaxP} = |Z|\sin\varphi \tag{2.9}$$

where the index *maxP* indicates a value under maximum power transfer. This is confirmed by Figure 2-2, which depicts how voltage *V*, current *I* and active power *P* vary with the load impedance, assuming a constant power factor of 0.8. Starting with light loading conditions (high load impedance) and slowly increasing the demand (moving from right to left on Figure 2-2) shows that the active power consumed increases until the maximum power transfer is reached. Any further increase in demand will cause a drop in active power, because after this point the voltage drop

across the line begins to dominate the increase in current. This holds true for a constant impedance load, which was assumed in this example. Different types of loads and their characteristics will be introduced later in this chapter.

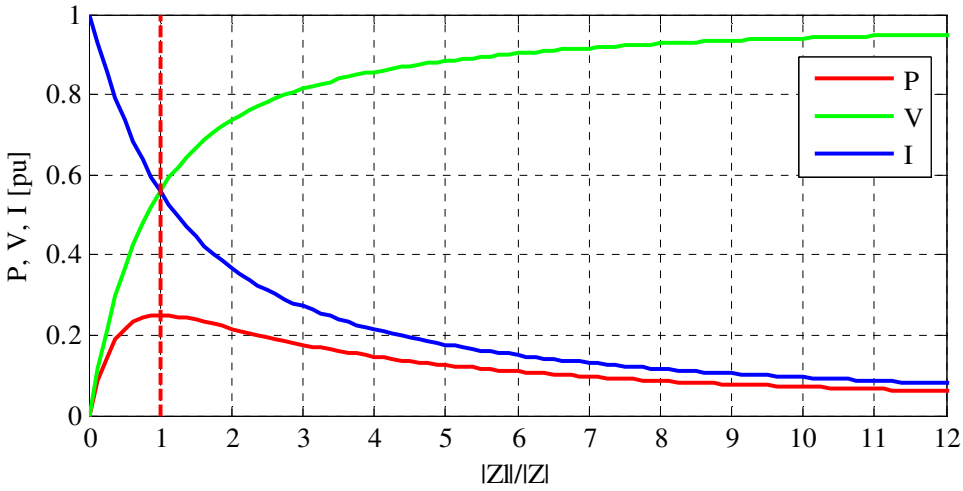

Figure 2-2: Voltage, current and active power as a function of the load impedance

For a lossless transmission system (resistance R = 0), the maximum active power transfer can be obtained from [3]:

$$P_{max} = \frac{\cos\varphi E^2}{(1+\sin\varphi)2X} \tag{2.10}$$

the corresponding reactive power:

$$Q_{\max P} = \frac{\sin\varphi E^2}{(1+\sin\varphi)2X} \tag{2.11}$$

and the corresponding voltage:

$$V_{\max P} = \frac{E}{\sqrt{2}\sqrt{1+\sin\varphi}} \tag{2.11}$$

It should be noted that the maximum active power transfer, and the corresponding reactive power and voltage, does not depend on load but only on the network

parameters. It indicates the transmission capacity of the network and defines a critical point in the system's characteristic. It is important to remember that if the load demand increases beyond this point the active power transfer will start decreasing with the voltage, which will cause unstable behaviour in the network.

2.3. PV and VQ Curves

In voltage stability analysis the relationships between active power and voltage and between reactive power demand and voltage are crucial. PV and VQ curves characterize the transmission system from the perspective of the load bus. This provides valuable information about the active power transmission capabilities of the system and the requirements regarding reactive power compensation, all in relation to the voltage at the load. In the simple case where the transmission line is lossless (i.e. $R = 0$), the load voltage for the system shown in Figure 2-1 can be defined as:

$$\overline{V} = \overline{E} - jX\overline{I} \tag{2.12}$$

and the apparent power consumed by the load can be defined as:

$$\overline{S} = \overline{V}\overline{I}^{*} = \overline{V}\frac{\overline{E}^{*} - \overline{V}^{*}}{-jX} = \frac{j}{X}\left(EV\cos\theta + jEV\sin\theta - V^{2}\right) \tag{2.13}$$

Taking into account that $\overline{S} = P + jQ$, (2.13) can be decomposed into:

$$P = -\frac{EV}{X}\sin\theta \tag{2.14}$$

$$Q = -\frac{V^{2}}{X} + \frac{EV}{X}\cos\theta \tag{2.15}$$

Equations (2.14) and (2.15) are the load flow equations of a lossless system and for a given P and Q they need to be solved with respect to V and θ [3]. Eliminating θ from (2.14) and (2.15) results in:

$$(V^{2})^{2} + (2QX - E^{2})V^{2} + X^{2}(P^{2} + Q^{2}) = 0 \tag{2.16}$$

which is a second order equation with respect to V^2 that gives a clear relationship between the three key quantities – load voltage V, active power P and reactive power Q. *PV* curves, also known as *nose curves*, depict the network characteristics for a given power factor (Figure 2-3). These curves provide information about the power transfer capabilities of a network and indicate the *voltage stability margin*, which is the amount of active power between the current operating point and the maximum power transfer (Figure 2-4). The location of the operating point 'A' indicates, assuming a constant power factor, that there is a considerable reserve of active power transfer secured by the current configuration of the transmission system.

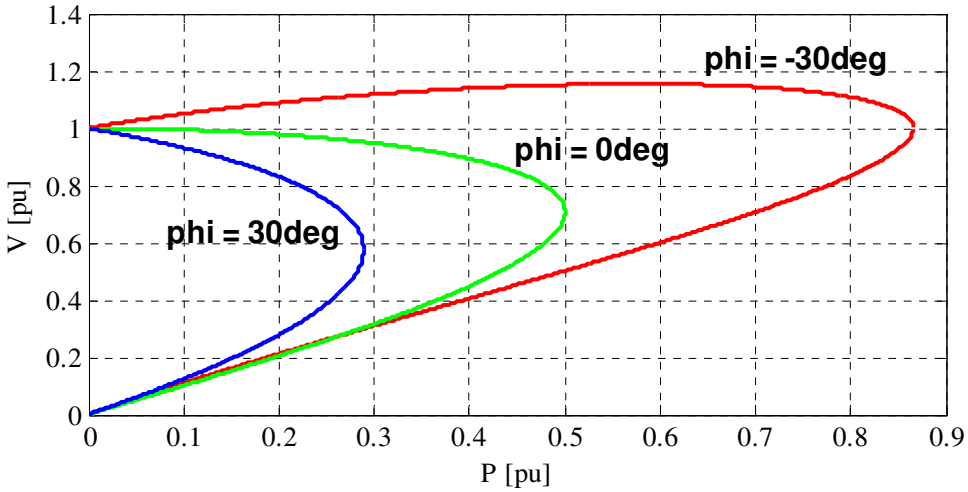

Figure 2-3: Nose curves for different power factors

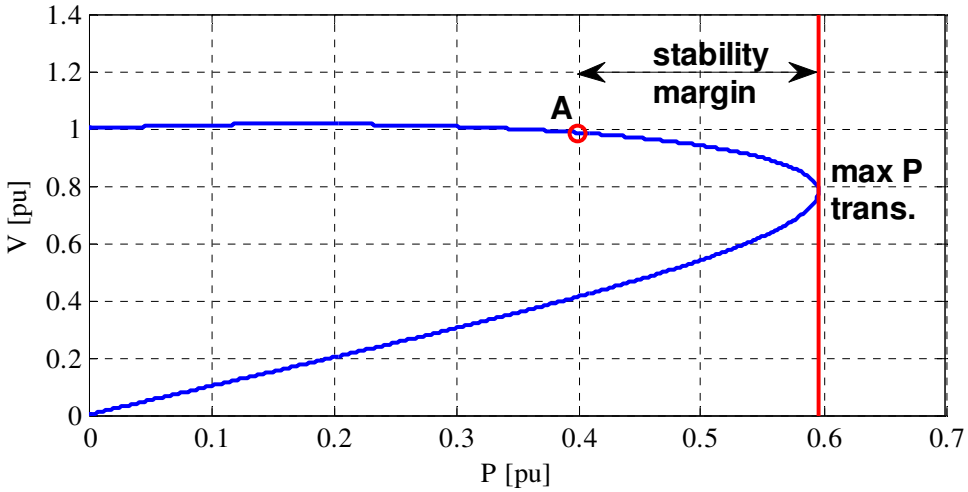

Figure 2-4: Stability margin on a *PV* curve

The operating point (A) on the network characteristic is obtained through finding a common point with the load characteristic, which will be explained in detail after the introduction of load types in the next section.

The situation is slightly different in the case of VQ curves because they are obtained for a specific loading condition. In the simplest case, where a constant power load is assumed, for a given (*P*, *Q*) condition the voltage is varied and a required reactive power compensation is calculated. Figure 2-5 presents example VQ curves for three different loading conditions, where each curve represents the amount of reactive power compensation required to obtain the desired voltage level.

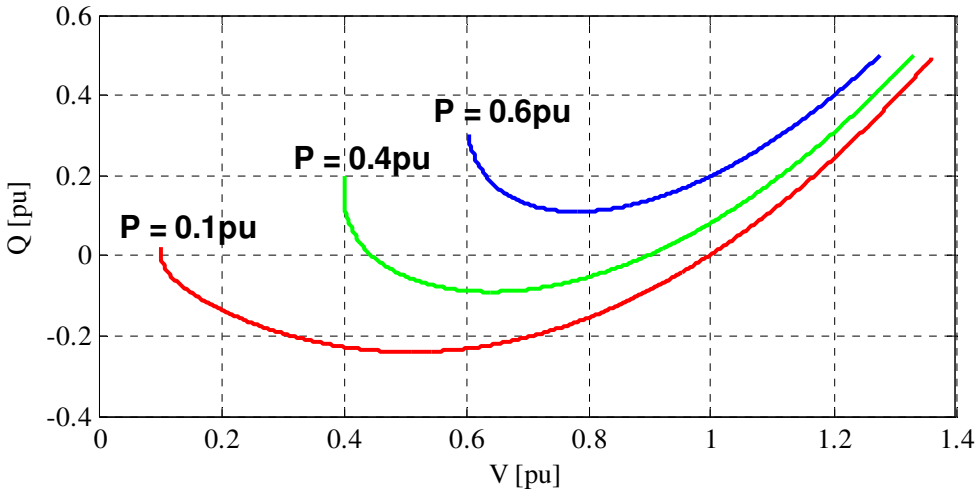

Figure 2-5: VQ curves for different loading conditions

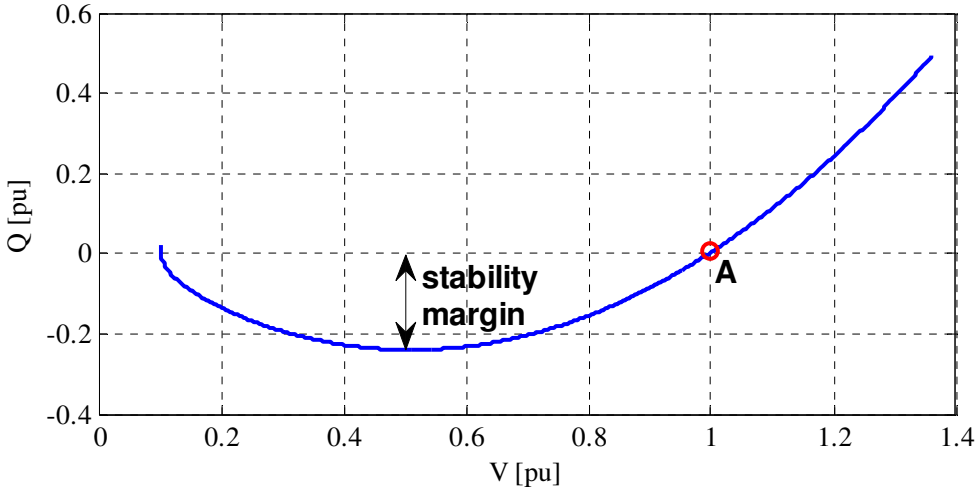

Figure 2-6: Stability margin on a VQ curve

It is clear from the figure that maintaining the same voltage level for a higher loading condition will require more reactive power compensation. Additionally, Figure 2-6 shows the stability margin in a lightly loaded case. This margin is a reactive power reserve which can accommodate an unfavourable network event (e.g. the loss of a line resulting in an increase in the system's reactance) or an increase in the reactive power demand of the load. It should be noted that this margin will enable the system to maintain a feasible operating point; however, it will not prevent the voltage from decreasing. An increase in the reactive power demand will cause the whole VQ characteristic to move up and change the operating point (the voltage will decrease). A similar rule can be observed in the PV curve in Figure 2-4. An increase in the active power demand will cause the operation point 'A' to move further to the right on the characteristic, this will result in a decrease in the voltage.

Figure 2-7 shows an example of a VQ curve where the reactive power demand has been increased. The new characteristic (curve 2) shows that there is no feasible operating point if reactive power compensation is not provided. Whilst the minimum compensation (comp. 1) will restore the operability of the system, much more compensation (comp. 2) will be required to return to the nominal voltage level.

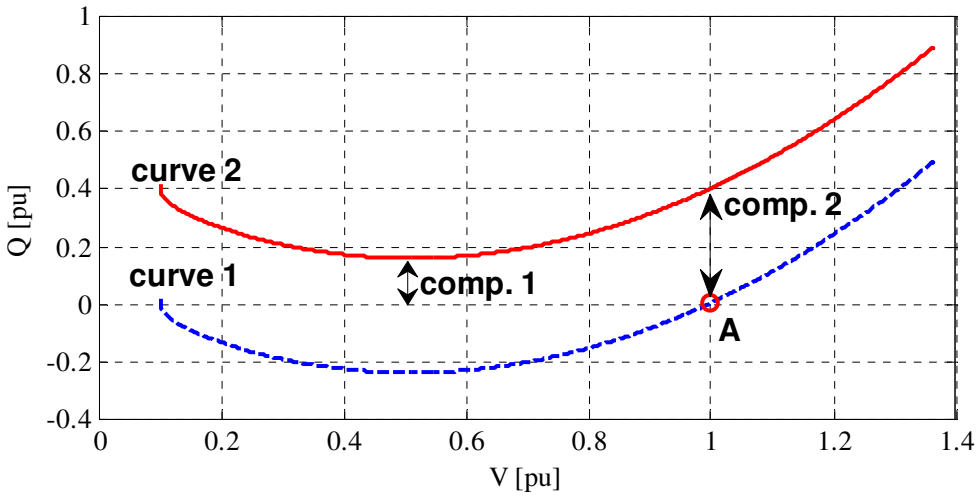

Figure 2-7: VQ for different reactive power demand

Both PV and VQ characteristics are very helpful in analysing the voltage instability mechanisms and scenarios. These curves must be used together to ensure that the system is at a healthy operating point. For example, highly compensated networks

may seem healthy due to acceptable voltage levels, whereas the actual operating point may be very close to the maximum power transfer on the PV curve (Figure 2-3). Combining the valuable insights into the system that can be gained from the PV and VQ curves can help to understand the behaviour of the system and provide appropriate countermeasures, like the proper level of reactive power compensation.

From the point of view of load modelling the most important outcome of this discussion is that the interactions between the network characteristics and the load characteristics will define the operating point of the system, in the case where one exists. Additionally, this has highlighted that plotting load characteristics against network characteristics provides a more accurate evaluation of different scenarios. In simulations it is common to assume that all loads are of a certain type, whereas in practice the characteristics of different loads will be different. This may lead to considerable discrepancies between voltage stability assessments, the origins and nature of which will be explained in detail in the following subsections.

2.4. Load Characteristics

As already mentioned, power system loads have a significant impact on the stability of a system. A proper understanding of load behaviour is crucial in voltage stability analysis, as it can provide information necessary for the accurate assessment of different scenarios, e.g. the voltage profile of a system under different loading conditions or contingency analysis. Load characteristics are the basic representation of loads in stability analysis. They are based on algebraic equations that express the relationship between the power consumed by the load and the load's voltage. Frequency dependency is usually neglected, since in voltage stability incidents the frequency excursions are not of primary concern [3]. An illustrative example of such characteristics, plotted against a PV curve, is shown in Figure 2-8. The selected characteristics correspond to three particular types of load - constant power, constant current and constant impedance. The operating point for each load type corresponds to the intersection of the PV curve and the corresponding load characteristic. From the figure it is clear that, whilst at the nominal voltage level the three loads draw the same amount of power, for lower voltages the consumed power is considerably different for

each of the three load types. For this reason, appropriate modelling of loads is crucial in voltage stability analysis.

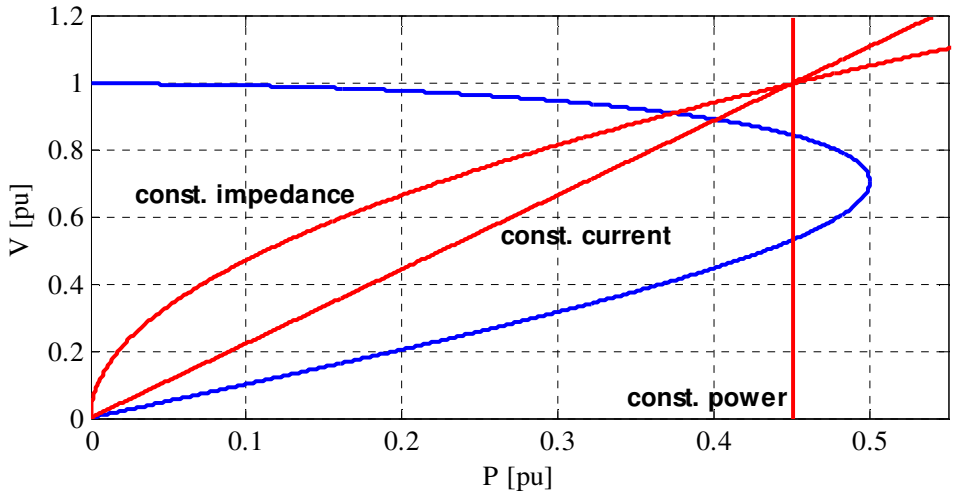

Figure 2-8: Load characteristics against a PV curve

The load connected to a bus in a power system will consist of many types of devices, the characteristics of which may be different. A common practice is to represent such an aggregation of load with a single equivalent model [1], [3]. There are two commonly used load models – the Exponential Load (EL) model and the polynomial model, also known as the ZIP model. The former is represented by the following equations:

$$P_d = P_0\left(\frac{V}{V_0}\right)^{\alpha}$$
$$Q_d = Q_0\left(\frac{V}{V_0}\right)^{\beta} \qquad (2.17)$$

where P_d and Q_d are the active and reactive power consumed by the load, respectively, α and β are the exponents responsible for the shape of the characteristic, V_0 is the reference voltage and P_0 and Q_0 are the active and reactive powers consumed by the load when the voltage is equal to the reference voltage, respectively. The constant power, current and impedance characteristics presented in Figure 2-8 were obtained by substituting the exponents with values of 0, 1 and 2, respectively.

The ZIP model is defined as follows:

$$\begin{aligned} P_d &= P_0\left(P_Z\left(\frac{V}{V_0}\right)^2 + P_I\left(\frac{V}{V_0}\right) + P_P\right) \\ Q_d &= Q_0\left(Q_Z\left(\frac{V}{V_0}\right)^2 + Q_I\left(\frac{V}{V_0}\right) + Q_Q\right) \end{aligned} \tag{2.18}$$

where P_Z, P_I and P_P are the constant impedance, constant current and constant power coefficients of the total active power, respectively, Q_Z, Q_I and Q_Q are the constant impedance, constant current and constant power coefficients of the total reactive power, respectively. Additionally, the coefficients satisfy the following conditions:

$$\begin{aligned} P_Z + P_I + P_P &= 1 \\ Q_Z + Q_I + Q_Q &= 1 \end{aligned} \tag{2.18}$$

Both of the models are suitable for representing aggregate loads, even though they do not produce identical characteristics. However, taking into account that the models are only valid within a certain range around the nominal voltage, both of them can give very similar results. An example comparison is presented in Figure 2-9, where three arbitrarily selected ZIP models have been approximated using EL models. In all of these cases both models produce very similar results for voltage magnitudes of above 0.7 per unit. In practice, at voltage lower than this the load behaviour may be very different, e.g. induction motors may be automatically disconnected and discharge lighting elements will extinguish below a certain voltage [1], [3].

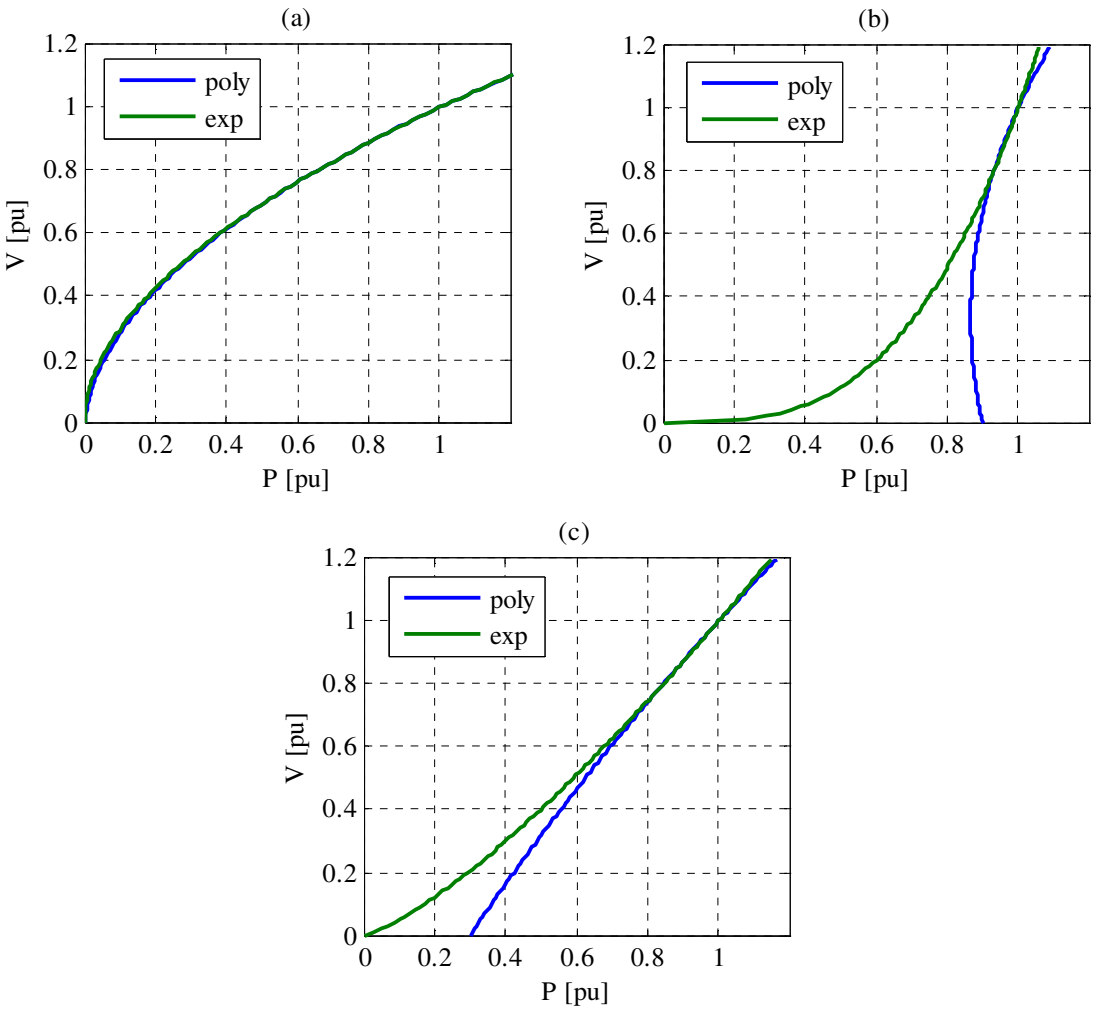

Figure 2-9: Characteristics of the polynomial model with equivalent characteristics of the exponential model: (a) $P_Z = 0.9$, $P_I = 0.1$, $P_P = 0$ and $\alpha = 1.8893$; (b) $P_Z = 0.3$, $P_I = -0.2$, $P_P = 0.9$ and $\alpha = 0.3156$; (c) $P_Z = 0.1$, $P_I = 0.6$, $P_P = 0.3$ and $\alpha = 0.7601$

Table 2-1 presents typical EL model (2.17) characteristics for some common devices [1]. The variety of the exponential coefficients is quite high, especially for reactive power. It should be noted that none of the devices listed in Table 2-1 is connected exclusively to a bus. As mentioned earlier, the load at a bus will consist of an undetermined mix of many different devices that need to be approximated by an equivalent characteristic. One way of representing an aggregated load is presented in Table 2-2 [1]. Equivalent characteristics for different load classes are given for both summer and winter. However, these characteristics are only approximations of the true load, since the composition of each load will be different, even for loads in the same load class. When possible, each load should be treated separately and its parameters should be obtained from measurements and updated whenever possible.

Table 2-1: Static characteristics of typical load components (EL model)

Component	Power factor	α	β
Air conditioner	0.82 - 0.96	0.088 - 0.468	2.3 - 2.5
Heaters	1.00	2.00	0.00
Dishwasher	0.99	1.80	3.60
Cloths washer	0.65	0.08	1.60
Cloths dryer	0.99	2.00	3.20
Refrigerator	0.80	0.77	2.50
Television	0.80	2.00	5.10
Incandescent light	1.00	1.55	0.00
Fluorescent light	0.90	0.96	7.40
Industrial motors	0.88	0.07	0.50
Fan motors	0.87	0.08	1.60
Agricultural pumps	0.85	1.40	1.40
Arc furnace	0.70	2.30	1.60

Table 2-2: Typical static characteristics of different load classes (EL model)

Load class	Power factor	α	β
Residential			
Summer	0.90	1.20	2.90
Winter	0.99	1.50	3.20
Commercial			
Summer	0.85	0.99	3.50
Winter	0.90	1.30	3.10
Industrial	0.85	0.18	6.00

2.5. Load Restoration

The load characteristics that were introduced in the previous section deal with the static behaviour of loads, which means that the transition from one operating point to another, due to a voltage deviation, will occur immediately. This immediate transition will occur for some of the devices connected to the system, but the biggest concern, from the point of view of voltage stability, is with loads that tend to have a delayed transition between operating points. After a voltage drop, the power drawn by these devices will drop immediately, just like in the case of a static load. However, this will not be the new operating point; instead, the power consumption will increase over time until a new steady state is reached. An example of such behaviour is depicted in Figure 2-10. This phenomenon can be interpreted as a static characteristic, the parameters of which are changing in time.

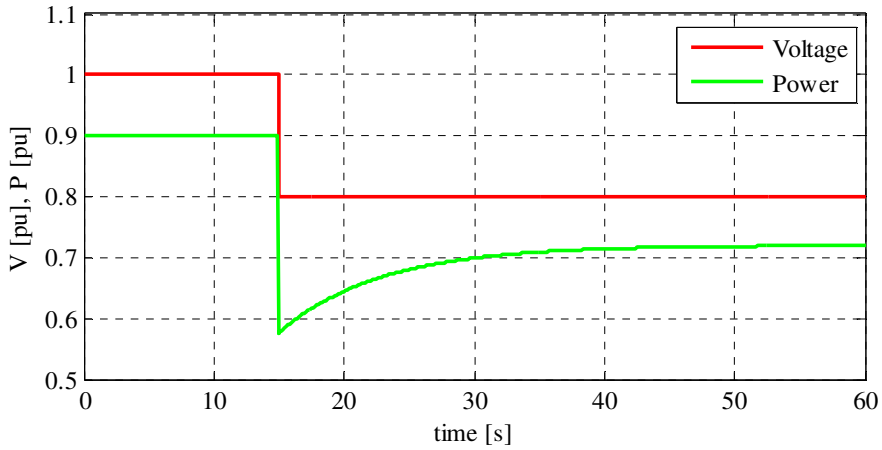

Figure 2-10: An example of power restoration after a voltage step change

A typical example of such a load is an Induction Motor (IM), a very common device, not only in industry but also, as small one-phase machines, in every household. The dynamics related to the inertia of rotating masses mean that an IM will not reach a new internal operating point immediately after a disturbance. For the largest machines it can take up to a few seconds for a new operating point to be reached. For this reason, IMs are modelled in detail for short-term stability analysis, whereas for longer time frames they are represented using static characteristics or a simplified model [3], [7]. Loads that are dominated by IMs are usually modelled using the Composite Load model [10], [21] in stability studies. This model consists of a 3rd order IM model connected in parallel with a Static Load model and will be described in detail in Chapter 4.

In long-term analysis there are several types of loads that tend to restore their power over time. Transformers equipped with On-Load Tap Changers (OLTC) are one example of such a device. Operating in a discrete manner, they act to maintain a fixed voltage on the LV side of the transformer. By doing so, they reduce the effective impedance seen by the system. This in turn increases the power demand every time the OLTC changes its position to recover the bus voltage [1], [3], [4], [7]. The time scale of such an action is usually of the order of tens of seconds. Transformers are normally modelled separately in stability analysis. Figure 2-11 shows a typical example of an OLTC action; this example was obtained using the DIgSILENT software. The plot shows the HV and LV side voltage magnitudes of a transformer, as

well as the active power recorded at the HV side of the transformer. After the loss of a line in the system at t = 80s, the observed voltages and active power (due to a constant impedance load fed through the transformer) drop immediately. After 5 seconds the OLTC begins to act to restore the LV side voltage to the given set point of approximately 1pu. This causes the active power to recover as well, but the HV side voltage will decrease further due to the increased reactive power demand, lowering the voltage profile of the network.

Another type of load that contributes to long-term power recovery are thermostat controlled devices, which are used in different types of heating, e.g. water heaters, space heating, industrial process heating [1], [3], [7]. As it can be seen in Table 2-1, heaters in general are a constant resistance load; however, this is only true for uncontrolled devices. Otherwise, the average power output of a heater will be equal to that necessary for maintaining the required temperature under given conditions [3].

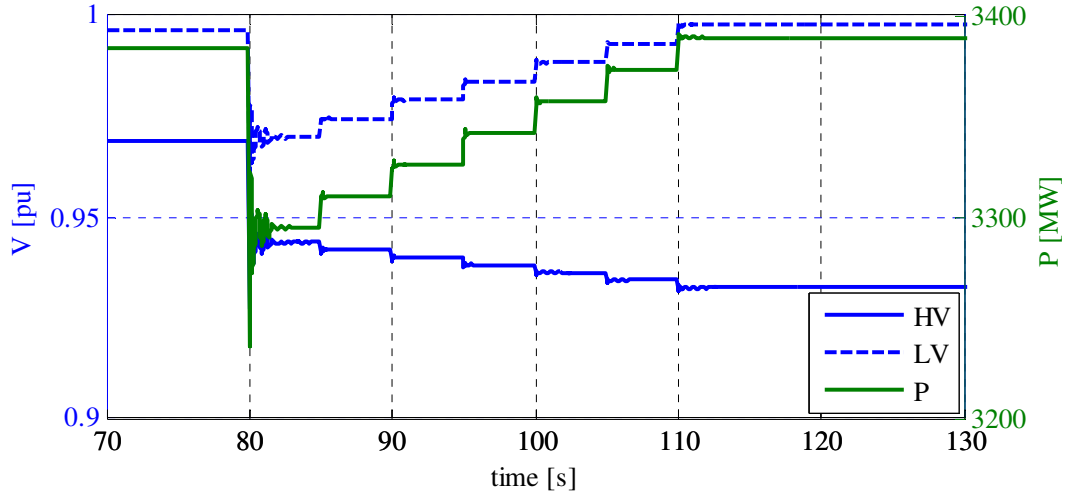

Figure 2-11: Restorative action of a transformer after a loss of a line

Figure 2-12 presents the duty cycle of a thermostat controlled device. The heater is working on full power until the desired temperature is reached and after that it is switched off, waiting for the temperature to drop again. The average power drawn by such a device can be defined as:

$$P_{avg} = \frac{t_{on}}{t_{on} + t_{off}} P_{max} = \frac{t_{on}}{t_{on} + t_{off}} GV^2 \tag{2.19}$$

where G is the conductance of the heater. From (2.19) it can be seen that the maximum power is proportional to the square of voltage. Assuming a load that includes many thermostat controlled heaters, immediately after a voltage drop, the power drawn by all of the connected devices at that moment will drop, just like a constant impedance load would. This means that the total power consumed by the load will drop as well. However, because the maximum power of each device is now lower, the duty cycle will change and keep the heaters on-line for longer to provide the same average power. The time for the original power to be restored will be of the order of several minutes, depending on the size of the heaters and the duty cycle before the disturbance. However, this process has limitations. For example, below a certain voltage the thermostat will keep the device on-line all the time and the average power will become equal to the maximum power in (2.19). This will make further restoration impossible and the load will behave like a constant impedance load until its voltage is restored [3]. Thermostat controlled devices are usually modelled using aggregate dynamic load models, like the Exponential Recovery Load [3], [4], [7], [31], which will be introduced in detail in Chapter 4.

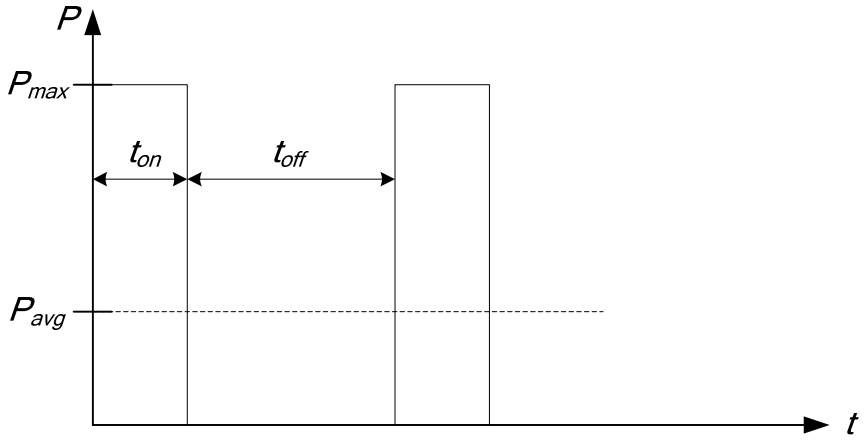

Figure 2-12: Duty cycle of a thermostat controlled device

2.6. Instability Mechanisms

There are two typical voltage instability scenarios. One is related directly to load and it involves a steady increase in the demand. Figure 2-13 depicts this situation on a PV

characteristic for two load types to show how different load characteristics will influence the voltage profile of a network.

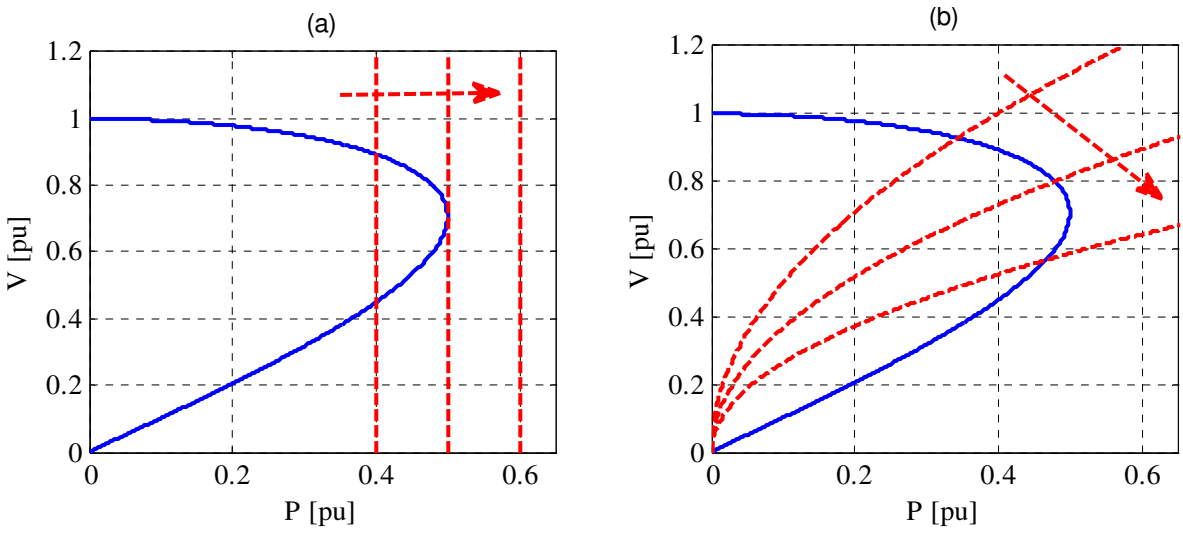

Figure 2-13: Increase of demand on a PV curve: (a) constant power load; (b) constant impedance load

An increase in the demand of a constant power load (Figure 2-13a) will shift the load characteristic to the right, causing increased power consumption, until the maximum transfer is reached. Any further increase in the demand will lead to a loss of equilibrium – a condition under which the network cannot operate anymore [3]. A different situation is presented in Figure 2-13b, where the same scenario of increasing demand is illustrated for a constant impedance load. Under normal operation (on the upper part of the network's PV characteristic), an increase in the demand will cause an increase in the power transfer and a decrease in the load voltage, which is the natural behaviour of a power system. However, contrary to the constant power load, the constant impedance load can still operate after crossing the maximum power transfer on a PV characteristic. From the point of view of stability, a purely static load can operate on the lower part of the network's characteristic, although it will be accompanied by a low voltage. Such an operating point becomes unstable in the case of a controlled load, which tends to restore its power. From Figure 2-13b it is clear that any further increase in the demand, after crossing the maximum transfer point, will cause a simultaneous decrease of both the power transfer and the voltage – a behaviour which may lead to voltage collapse [1], [3].

The second typical scenario is more dramatic and it involves a sudden change in the network, e.g. the loss of a transmission line or the loss of generation. Such a disturbance will be reflected in the equivalent system as an increase in the transmission impedance *X* or a decrease in the voltage source magnitude *E*.

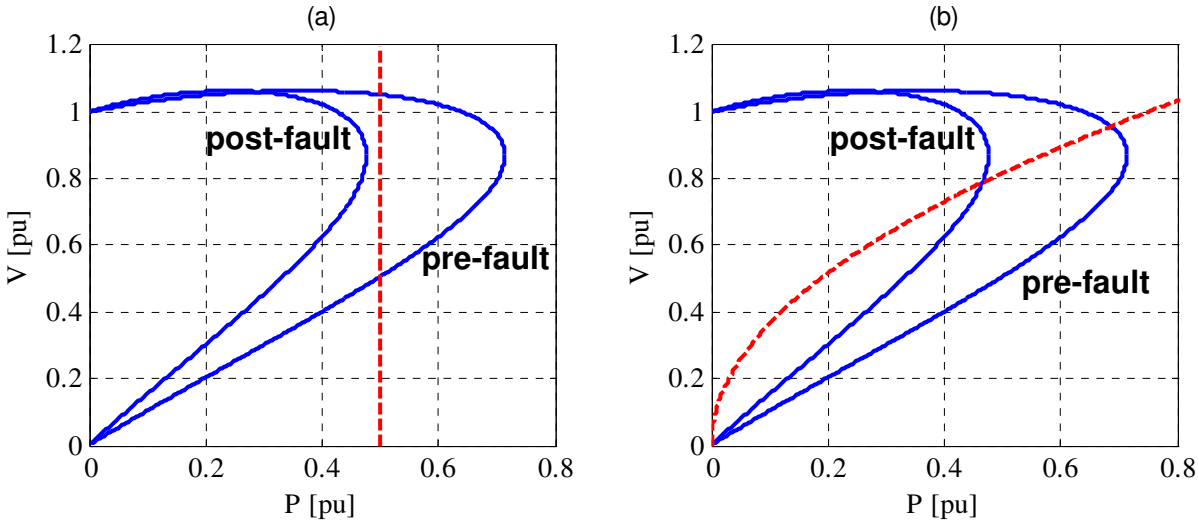

Figure 2-14: Disturbance on a PV curve: (a) constant power load; (b) constant impedance load

Figure 2-14 shows the pre- and post-disturbance network's PV characteristics plotted against constant power (Figure 2-14a) and constant impedance (Figure 2-14b) load characteristics. In the first case, it can be observed that after the disturbance the characteristics no longer intersect one another, which means that no feasible operating point exists. However, for a constant impedance load an operating point exists even after the disturbance, which makes the situation much more favourable. The nature of a constant impedance characteristic means that there will always be an operating point available, the only limitation is the acceptable lower voltage limit [3].

2.7. 10-bus System Case Study

A more practical example that depicts voltage instability mechanisms can be obtained using a 10-bus test system [1] that has been built using DIgSILENT software. This scenario focuses mainly on the load-network relationship; however, the system also includes elements related to generation – Automatic Voltage Regulators (AVRs) and Over-excitation Limiters (OXLs). The former controls the terminal voltage of a generator by regulating the excitation system and the latter protects the generator by

limiting the excitation voltage when the field current exceeds the allowed value. Generator 1 is an infinite bus, generators 2 and 3 are equipped with AVRs and generator 3 has an OXL. The single-line diagram of the system is depicted in Figure 2-15 and its details are provided in Appendix A.

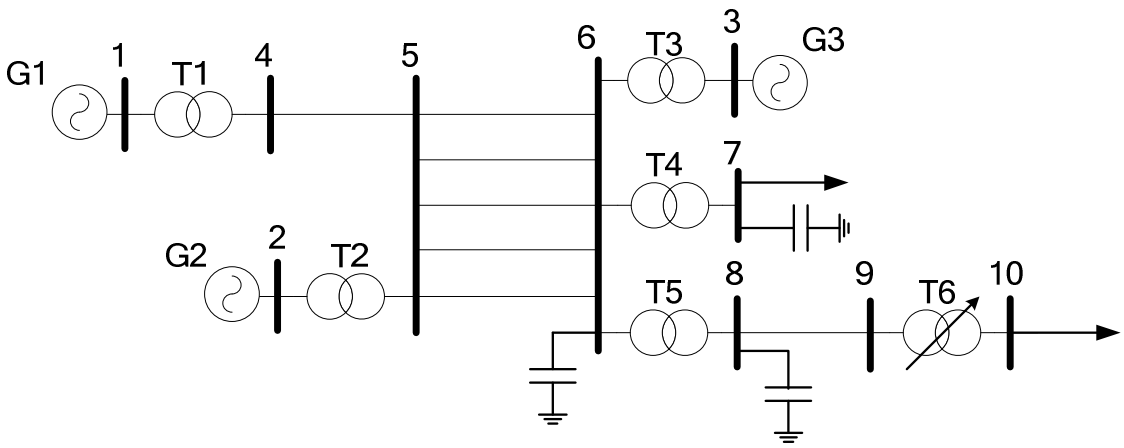

Figure 2-15: Single-line diagram of the 10-bus test system

A typical cascading scenario usually occurs in heavily loaded networks where load centres are remote from the generation [1], [3]. Such a situation may cause some of the transmission lines to become overloaded and they will eventually be disconnected, transferring the stress to the neighbouring lines. This will increase the equivalent system's impedance, which in turn will 'shrink' the PV characteristic. As a consequence, more lines may become overloaded and disconnected. Eventually, due to increased demand for reactive power, generators may reach their reactive power output limits, which will cause a dramatic decrease in the generators' terminal voltage, further worsening the voltage profile of the system. The significance of the contribution of transformers equipped with OLTCs in this scenario will depend on the type of load fed through the transformer. As such, a similar scenario will be presented for three particular types of static load – constant power, current and impedance.

The load of interest is connected at bus 10. Whilst the load characteristic is different, the initial power drawn in each of the three cases is the same. The scenario consists of line outages; starting at t = 80s, every 50s one of the 5 parallel lines is taken out of service, until there is no convergence in the simulation or generator 3 exceeds its

excitation limits. Figure 2-16 and Figure 2-17 present how the voltage at bus 10 changes over time for each of the load characteristics investigated. As expected, after the first line outage the largest voltage drop is seen for the constant power load and smallest for the constant impedance load. Transformer T6 manages to recover the voltage in 6 steps for all three cases, but following the next line outage the network cannot meet the constant power load's demand and the operating point is lost in this case. The remaining two cases withstand the second outage and the OLTC tries to recover the voltage until it reaches its limit.

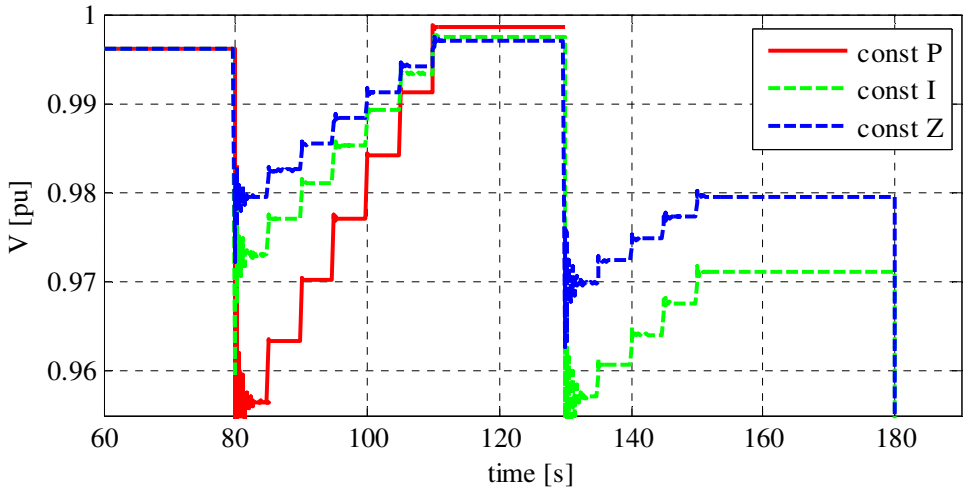

Figure 2-16: Voltage at bus 10 (outage of two lines)

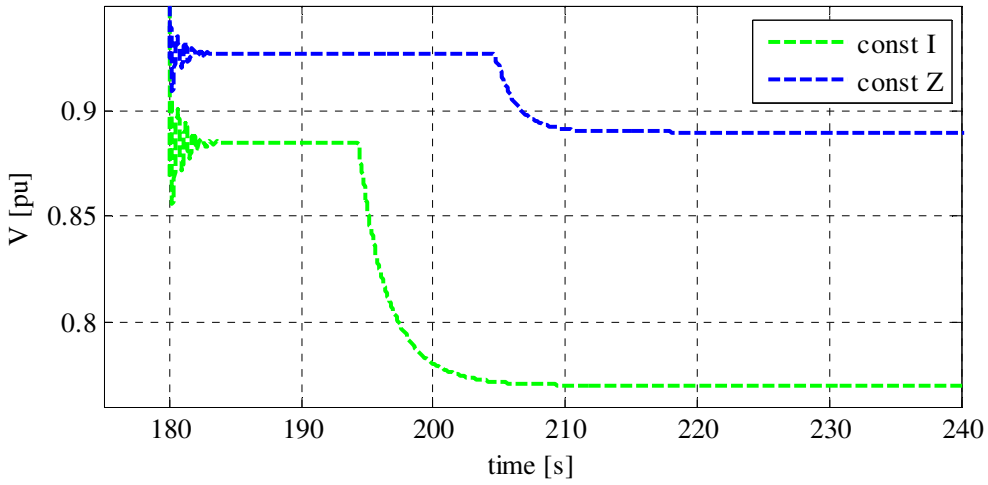

Figure 2-17: Voltage at bus 10 (outage of the third line)

After the third line outage (Figure 2-17) the field current of generator 3 quickly reaches its limits and the OXL sends a signal to the AVR to decrease the excitation

voltage. It should be noted that although the system in both cases is still operating, the constant current load is causing very low voltage at bus 10.

The negative action of the OLTC can be observed in Figure 2-18 and Figure 2-19, where the voltage at bus 9 is presented. Every attempt made by the OLTC to restore the voltage at but 10 increases the active and reactive power demand placed on the network. This in turn is pushing the operating point further towards the maximum power transfer point, which means a lower voltage profile across the network.

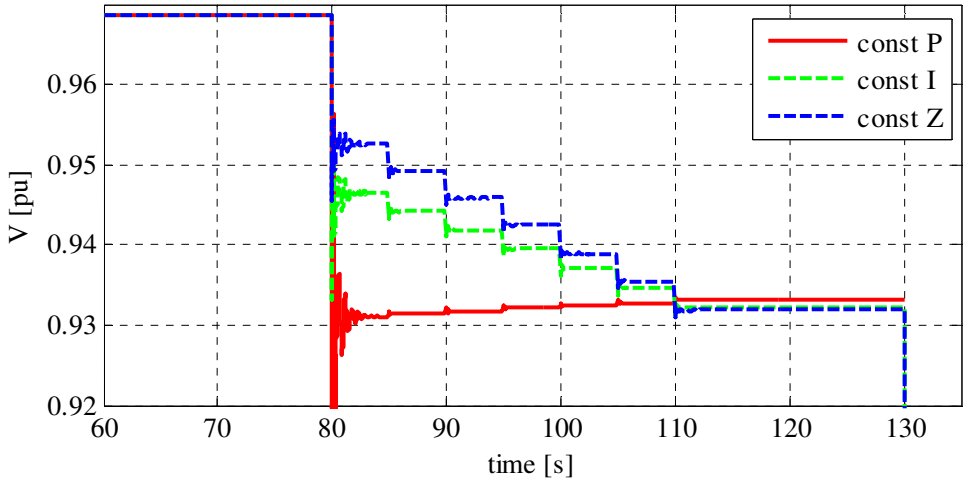

Figure 2-18: Voltage at bus 9 (outage of one line)

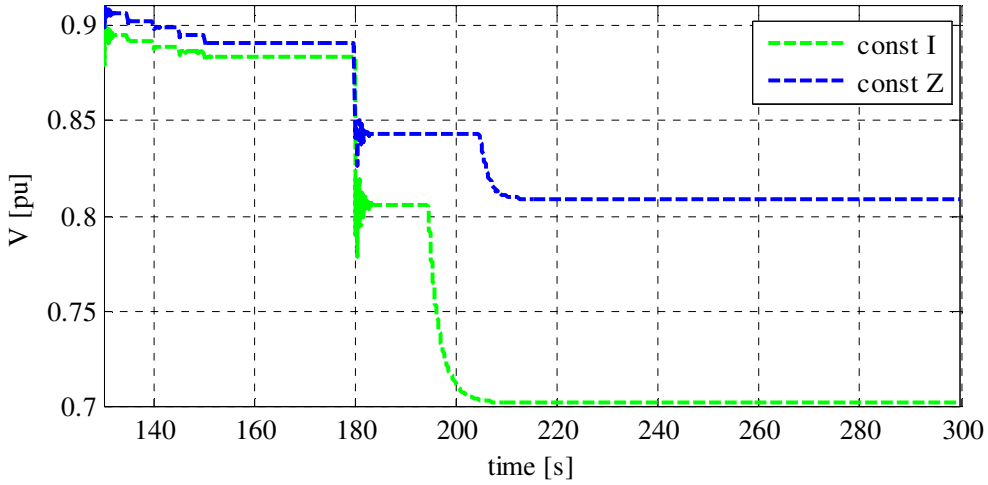

Figure 2-19: Voltage at bus 9 (outage of the second and third lines)

The only exception is the constant power load. In Figure 2-18 it can be seen that the OLTC action is actually causing the voltage at bus 9 to recover, which can be

attributed to reactive losses in the transformer. Constant power load will draw the same amount of power no matter what is the bus voltage, which means that lower voltage at bus 10 will lead to increased current and additional I^2X losses in the transformer. When the load voltage is increased the reactive power demand in the transformer is reduced, and the voltage profile of the rest of the network is slightly improved.

Figure 2-20 depicts the active power consumed by the load at bus 10. As expected, the load behaves according to the selected characteristic in each case. In the case of a constant power load the system continues to operate until the demand does not exceed the maximum power transfer and the remaining two models continue operating but with considerably reduced voltage and power transfer . It should also be noted that, before the OXL action both voltage dependent loads are still operating on the upper part of the network's PV curve, but afterwards the system's characteristic recedes even more and the operating point move to the unstable part of the characteristic. As previously mentioned, such a situation could be dangerous if the load is equipped with a control device that is trying to restore its power. This change in the operating point after the OXL action can be recognised because the constant impedance load starts to draw more power than the constant current load.

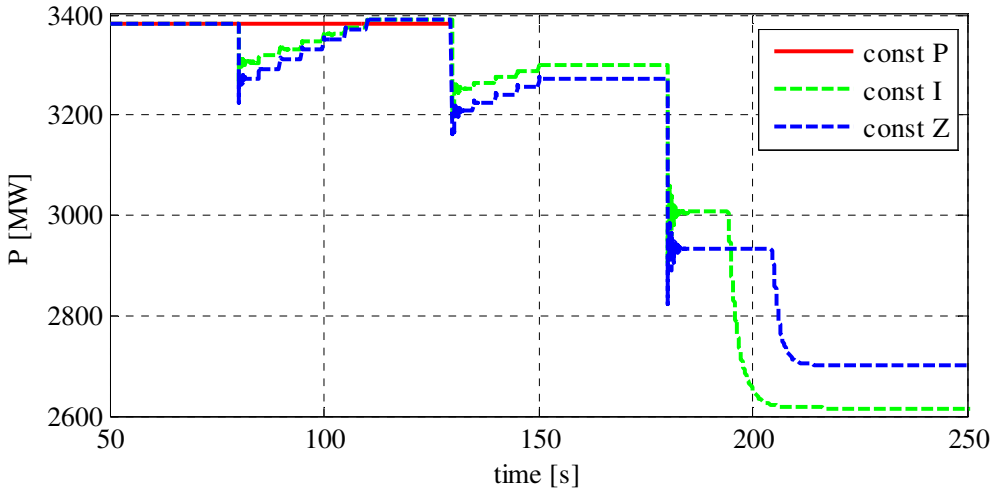

Figure 2-20: Active power consumed by the load at bus 10

This simulation example clearly shows that a single instability scenario can have different outcomes depending on the load characteristics. Accurate assessment of the

voltage security of a given network will require detailed information about the connected loads under different conditions and times, an element which can be provided by the measurement-based approach to load modelling.

2.8. Conclusions

The goal of this chapter was to introduce voltage instability and clarify the contribution of loads to this phenomenon. Although the whole process involves many other elements and interactions between them, loads are the most uncertain component of all, because it belongs to customers and it is beyond the control of network operators.

From the perspective of voltage stability, the key information about loads is held within their characteristics. The voltage dependency of loads has a significant effect on the power demand under off-nominal conditions, which in turn will have a huge effect on the behaviour of the whole network, and especially its voltage profile. This synergy has been explained using a PV plane, where it could be seen that the operating point will change considerably for different load characteristics. A case study simulated on a 10-bus test system confirmed that the three basic load types will produce very different results for the same scenario; the nature of these results included the loss of equilibrium and a very low voltage profile.

The process of power restoration by loads introduces further complications. Some of the loads connected to the system will reach a new steady operating point immediately after a disturbance, whilst others will take some time to reach such an operating point. This phenomenon will intensify the stability problem. However, if the dynamic properties of the load were available beforehand, it would be possible to predict the final result and possibly act in order to alleviate the consequences (e.g. the action of an OLTC could be blocked in some cases to prevent the restoration).

Additionally, the aggregation of many different devices will produce a high variety of characteristics and result in a wide range of possible exponents defining the load model. What is more, the load composition will depend on factors such as weather

conditions and time. The combination of these factors leads to a very important conclusion – assuming a fixed load model without any research conducted in this matter may cause serious errors in the evaluation of the voltage security, especially when operating close to stability margin.

3. Estimation of Power Components

3.1. Introduction

Determination of signal parameters can be considered as a fundamental procedure, since the majority of other applications rely on its quality and accuracy, including estimation of load model parameters. Early approaches to the problem used the well known Discrete Fourier Transform (DFT) algorithm [44]-[47] for spectrum analysis of a signal. The method however is very sensitive to frequency deviations, which were introducing significant errors in to the estimation of signal magnitude. Another shortcoming of the method is sensitivity to noise [64]. A similar problem of sensitivity to frequency deviations characterized early applications of linear methods like Least Squares (LS) or the Kalman Filter (KF), where a constant frequency was assumed [44]-[46]. To overcome these problems it was necessary to consider frequency as one of the unknown variables. In [48] the frequency deviation was included as an unknown parameter and estimated together with magnitude using the Extended Kalman Filter (EKF). A similar approach was used in [51] and [52] but instead of EKF a Newton-type algorithm was used in an iterative procedure. In [53] a Nonlinear Least Squares (NLS) method has been used to estimate signal frequency. However, the signal model does not consider a DC component, which means that in some cases pre-filtering would be necessary. An adaptive algorithm called Self-Tuning Least Squares (STLS) has been proposed in [65] and [66], where a frequency correction step is obtained at each iteration of a linear LS to improve the accuracy of the next step and eliminate the frequency sensitivity from the method. A number of methods based on adaptive filtering have been proposed in [56]-[59], where the filter coefficients have been updated according to the estimated frequency obtained by a recursive maximum likelihood method [54]. The latter has been extended in [55] to also include magnitude estimation. The interpolated DFT [49], [50] offers an improvement over the traditional DFT by using the two strongest spectrum coefficients around the fundamental frequency instead of just using one. In this way the algorithm reduces the frequency sensitivity and at the same time it offers off-nominal frequency estimation.

Most of the aforementioned methods are based on iterative algorithms that require an observation window, which introduces a certain delay in the result. Usually the minimum length of the window is one period of the fundamental frequency, which would result in a delay of at least 20ms in a system operating at a nominal frequency of 50Hz. The recursive method presented in [54], [55] requires only 3 samples to give a result. However, the input signal needs to undergo filtering to eliminate the strong influence of noise and harmonics and like [53] this method does not include a DC component in its signal model.

To overcome the disadvantages present in these other methods, a non-linear Kalman Filter based estimator, the Unscented Kalman Filter (UKF), is used in this project. This method, as opposed to the EKF, is not based on the use of model linearization, so it does not require the model's Jacobian to be calculated, consequently it demonstrates better performance than the EKF [67], [68]. In the problem considered, the instantaneous power signal is used as the algorithm's input. Frequency and power components are estimated directly from the samples of the instantaneous power signal. This is contrary to traditional approaches, in which voltages and currents are processed first, to determine their phasors, from which the unknown power components are determined in the second stage. Using the new approach, the processing requirements are significantly reduced. Furthermore, a high level of algorithm robustness has been achieved. In particular, the measurement sensitivity to power system frequency changes is eliminated and a DC component is included in the model. In this work the higher harmonics are treated as random noise, filtered out by the estimator. The proposed method is compared against Interpolated DFT and the STLS method in a series of computer-simulated and real-data tests.

3.2. Instantaneous Power Signal Model

A simple yet efficient instantaneous power model was introduced in [69]. Using a simple RLC series model (Figure 3-1) the instantaneous voltage and current can be expressed as:

$$v(t) = V_m \cos(\omega t) \tag{3.1}$$

$$i(t) = I_m \cos(\omega t - \varphi) \tag{3.2}$$

where V_m and I_m are voltage and current maximum values and φ is the power angle, i.e. the difference between the voltage and current phase angles. Let us also assume that the power system frequency ω is not strictly equal to its rated value (50, or 60 Hz) and that it can be considered as a variable. Using expressions (3.1) and (3.2), the instantaneous power is defined as:

$$p(t) = v(t) \cdot i(t) = P + S \cos(2\omega t - \varphi) \tag{3.3}$$

where

$$P = VI \cos\varphi \tag{3.4}$$

$$S = VI \tag{3.5}$$

are the active, P, and apparent, S, powers. Note that V and I are the RMS values of voltage and current respectively. Based on equations (3.4) and (3.5), the reactive power can be expressed as follows:

$$Q = \sqrt{S^2 - P^2} \tag{3.6}$$

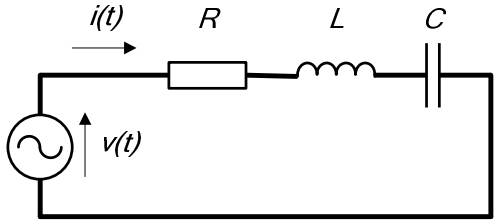

Figure 3-1: Series RLC circuit

The expression for instantaneous power (3.3), called the *instantaneous power parameter model*, is the starting point for developing the estimator. Expression (3.3) defines the instantaneous power parameter model for the fundamental frequency components (e.g. 50, or 60 Hz), without consideration of the effects of higher

harmonics. A significant advantage of such a model is its simplicity. In this model the higher harmonics are considered as random noise that should be filtered out. In the instantaneous power parameter model (3.3) the following unknown model parameters can be identified: active power *P*, apparent power *S*, power angle φ and power system frequency ω.

For the purpose of the estimation of the instantaneous power model parameters described by (3.3), the problem has to be represented in the state-space form required by any Kalman filter type estimator. The proposed model is simpler than the one proposed in [70], yet accurate and effective. The new representation requires estimation of only 2 parameters to obtain the frequency, whereas the model presented in [70] required the estimation of 3 parameters to perform the same task. In this way the proposed model could be used to estimate the DC component (active power in this case) without increasing the dimension of the problem (4 parameters to be estimated in total for both models). For this reason (3.3) was simplified to:

$$p(t) = P + S\cos(\alpha) \tag{3.7}$$

where angle α is a new state substituting the term $(2\omega t - \varphi)$. In this way the state-space model of the instantaneous power consists of one state and three parameters:

$$\begin{aligned} x_1 &= \alpha \\ x_2 &= \Delta\alpha \\ x_3 &= P \\ x_4 &= S \end{aligned} \tag{3.8}$$

which are related through a linear state mapping (3.9) and a nonlinear measurement mapping (3.10):

$$\begin{aligned} x_{1,k+1} &= x_{1,k} + x_{2,k} \\ x_{2,k+1} &= x_{2,k} \\ x_{3,k+1} &= x_{3,k} \\ x_{4,k+1} &= x_{4,k} \end{aligned} \tag{3.9}$$

$$y_{k+1} = x_{3,k+1} + x_{4,k+1}\cos(x_{1,k+1}) \tag{3.10}$$

Taking into account that $\Delta\alpha = 2\omega T_s$ (where T_s is the sampling period), the angular frequency ω at each discrete step *k* can be simply obtained in the following way:

$$\omega_k = \frac{x_{2,k}}{2T_s} \tag{3.11}$$

and the reactive power *Q* can be obtained from (3.6).

The above approach is valid for single-phase systems with undistorted voltages and currents and processing of instantaneous power expressed through equation (3.7). The signal distortions are treated as random noise, filtered out through the estimation process. The approach might be extended to the *n*-phase systems case through simple addition of particular single phase power components.

3.3. Estimation Methods

3.3.1. Interpolated DFT

Assuming a sampled multi-frequency signal with a DC component of the form:

$$x_k = A_0 + \sum_{M=1}^{M_{\max}} A_M \sin(2\pi f_M k T_s + \phi_M) \quad k = 0,1,\cdots,N-1 \tag{3.12}$$

where *N* is the number of samples belonging to the observation window and T_s is the sampling period, the DFT spectrum components can be calculated in the following way:

$$S(i) = \sum_{k=0}^{N-1} x_k \exp(-j\frac{2\pi}{N}ik) \quad i = 0,1,\ldots,N\text{-}1 \tag{3.13}$$

Interpolated DFT, in its basic form [49], is a simple expansion of the traditional DFT. In essence, the two strongest spectrum lines obtained from the DFT are utilized to estimate the fundamental frequency, DC magnitude and the magnitude and phase of the harmonics. The algorithm is of use in cases where the fundamental frequency is not equal to a multiple of the frequency resolution of the DFT expressed by:

$$f_0 = \frac{f_s}{N} \tag{3.14}$$

where $f_s=1/T_s$ is the sampling frequency. Assuming that $|S(l)|$ and $|S(l+1)|$ are the two largest spectrum lines, around the fundamental frequency, that were obtained from the DFT the following ratio can be calculated:

$$\alpha = \frac{|S(l+1)|}{|S(l)|} \tag{3.15}$$

and the fundamental frequency, magnitude and phase can be calculated as follows:

$$f_1 = \left(l + \frac{\alpha}{1+\alpha} \right) \frac{f_s}{N} \tag{3.16}$$

$$A_1 = \frac{2\pi\delta}{N} \frac{|S(l)|}{|\sin(\pi\delta)|} \tag{3.17}$$

$$\phi_1 = \begin{cases} \arg(S(l)) - a\delta + \pi/2 & \text{if } S(l) > S(l+1) \\ \arg(S(l+1)) - a(\delta-1) + \pi/2 & \text{otherwise} \end{cases} \tag{3.18}$$

$$\delta = \frac{\alpha}{1+\alpha} \tag{3.19}$$

$$a = \pi(N-1)/N \tag{3.20}$$

The magnitudes and phases of the harmonic components can be calculated in a similar way [49]. The last step is to calculate the magnitude of the DC component:

$$A_0 = A_{av} - \frac{1}{N} \sum_{M=1}^{M_{\max}} A_M \frac{\sin(\pi\lambda_M)}{\sin(\pi\lambda_M / N)} \sin(a\lambda_M + \phi_M) \tag{3.21}$$

$$\lambda_M = M(l+\delta) \tag{3.22}$$

where M_{max} is the number of harmonics considered in the calculation and A_{av} is the average value of the measured signal over the observation window. A full derivation of the method can be found in [49].

3.3.2. Self-Tuning Least Squares

The Self-Tuning Least Squares (STLS) method is an adaptive linear estimation algorithm based on the traditional Least Squares (LS) method [65], [66]. It was specifically designed to overcome the frequency sensitivity issues present in the estimation of signal parameters using the LS method. The nonlinear signal model given by (3.23) is expanded in to its orthogonal components to remove the nonlinearity related to the phase shift φ_k of the kth harmonic. In the next step the model is linearized using the first two terms of the Taylor series. The DC component was approximated around t=0 and the periodical components were approximated around $\omega=\omega_0$.

$$u(t) = U_0 e^{-\delta t} + \sum_{k=1}^{M} U_k \sin(k\omega t + \varphi_k) = U_0 e^{-\delta t} + \sum_{k=1}^{M} U_{pk} \sin(k\omega t) + \sum_{k=1}^{M} U_{qk} \cos(k\omega t) \tag{3.23}$$

$$\begin{aligned} u(t) = {} & U_0 - U_0 \delta t + \sum_{k=1}^{M} (U_{pk} \sin(k\omega_0 t) + U_{pk} \Delta\omega k t \cos(k\omega_0 t)) \\ & + \sum_{k=1}^{M} (U_{qk} \cos(k\omega_0 t) + U_{qk} \Delta\omega k t \sin(k\omega_0 t)) \end{aligned} \tag{3.24}$$

where M is the number of harmonics considered in the model, U_k is the amplitude of the kth harmonic, U_{pk} and U_{qk} are the orthogonal components of the kth harmonic and δ is the damping of the DC component. The linear signal model can be rewritten as:

$$u(t) = \sum_{k=1}^{4M+2} h_k(t) x_k \tag{3.25}$$

$$\begin{bmatrix} h_1 \\ h_2 \\ h_{2+k} \\ h_{2+k+M} \\ h_{2+k+2M} \\ h_{2+k+3M} \end{bmatrix} = \begin{bmatrix} 1 \\ -t \\ \sin(k\omega_0 t) \\ kt\cos(k\omega_0 t) \\ \cos(k\omega_0 t) \\ -kt\sin(k\omega_0 t) \end{bmatrix} \quad \begin{bmatrix} x_1 \\ x_2 \\ x_{2+k} \\ x_{2+k+M} \\ x_{2+k+2M} \\ x_{2+k+3M} \end{bmatrix} = \begin{bmatrix} U_0 \\ U_0\delta \\ U_{pk} \\ U_{pk}\Delta\omega \\ U_{qk} \\ U_{qk}\Delta\omega \end{bmatrix} \quad k = 1, 2, \cdots, M \tag{3.26}$$

Now, assuming that the signal $u(t)$ is uniformly sampled over a period of time, the estimate of the unknown vector of parameters can be obtained using the LS approach:

$$\hat{\mathbf{x}} = (\mathbf{H}^T\mathbf{H})^{-1}\mathbf{H}^T\mathbf{u} \tag{3.27}$$

From (3.26) it is clear that the accuracy of estimation will depend on the selected ω_0. For this reason, ω_0 is updated at each step using the estimation of angular velocity deviation $\Delta\omega$:

$$f_p = f_{p-1} + \alpha\frac{\Delta\omega_p}{2\pi} \tag{3.28}$$

where f_p is the frequency estimation for the pth iteration (f_0 = 50Hz) and α is a tuning factor (3.30). So ω_0 for the pth iteration is equal to:

$$\omega_{0p} = 2\pi f_p \tag{3.29}$$

$$\alpha = E(\alpha_0, \alpha_1, R_0) = \alpha_0 + (\alpha_1 - \alpha_0)(1 - e^{-R/R_0}) \tag{3.30}$$

Where α_0, α_1 and R_0 are the tuning parameters and R is the sum of the residual error in the absolute values over the observation window. This strategy increases the convergence speed during a dynamic change and improves the accuracy in the steady state [65].

3.3.3. Unscented Kalman Filter

The concept behind the Unscented Kalman Filter was first proposed in [71], [72] to address the issues related to the implementation of the Extended Kalman Filter (EKF).

The inaccuracies introduced by the EKF could be overcome by utilizing a nonlinear transformation called the Unscented Transform (UT), which does not require the calculation of derivatives or linearization of the non-linear model [72].

3.3.3.1. Unscented Transform

The Unscented Transform exploits the ease with which one can approximate a Gaussian distribution, compared to an arbitrary nonlinear function or transformation [72]. Assuming a random variable $\mathbf{x} \in \Re^n$ with mean $\bar{\mathbf{x}}$ and covariance $\mathbf{P}_{\mathbf{xx}}$ and a nonlinear transformation **y = f(x)**, the main goal of the UT is to find the mean $\bar{\mathbf{y}}$ and the covariance $\mathbf{P}_{\mathbf{yy}}$ of the variable $\mathbf{y} \in \Re^m$. For this purpose a deterministically chosen set of *sigma points* is propagated through the nonlinear function **f(x)** [71]-[73].

The selection of the sigma points is based only on the knowledge of the variable **x** according to the following formula:

$$\begin{aligned} \boldsymbol{\chi}_0 &= \bar{\mathbf{x}} \\ \boldsymbol{\chi}_i &= \bar{\mathbf{x}} + (\sqrt{(n+\lambda)\mathbf{P}_{\mathbf{xx}}})_i \qquad i = 1,\ldots,n \\ \boldsymbol{\chi}_{i+n} &= \bar{\mathbf{x}} - (\sqrt{(n+\lambda)\mathbf{P}_{\mathbf{xx}}})_i \end{aligned} \tag{3.37}$$

where $\lambda = \alpha^2(n+\kappa)$ and $(\sqrt{(n+\lambda)\mathbf{P}_{\mathbf{xx}}})_i$ is the *i*-th column of the square root of a matrix $(n+\lambda)\mathbf{P}_{\mathbf{xx}}$, which can be calculated using the Cholesky factorization. Parameter α is a small constant, usually set to 10^{-3}, which combined with κ provides an extra degree of freedom to fine-tune the higher order moments of the approximation. This fine tuning can be used to reduce the overall approximation errors [72]. From (3.37) it is obvious that there are *2n+1* sigma points. In the next step the previously selected sigma points are propagated through the nonlinear function:

$$\boldsymbol{\gamma}_i = \mathbf{f}(\boldsymbol{\chi}_i) \tag{3.38}$$

The mean and covariance are calculated as follows:

$$\bar{\mathbf{y}} = \sum_{i=0}^{2n} W_i^{(m)} \boldsymbol{\gamma}_i \tag{3.39}$$

$$\mathbf{P}_{\mathbf{yy}} = \sum_{i=0}^{2n} W_i^{(c)} [(\boldsymbol{\gamma}_i - \bar{\mathbf{y}})(\boldsymbol{\gamma}_i - \bar{\mathbf{y}})^T] \tag{3.40}$$

where the weights $W_i^{(m)}$ and $W_i^{(c)}$ are defined as:

$$W_0^{(m)} = \frac{\lambda}{n+\lambda} \tag{3.41}$$

$$W_0^{(c)} = \frac{\lambda}{n+\lambda} + (1-\alpha^2+\beta) \tag{3.42}$$

$$W_i^{(m)} = W_i^{(c)} = \frac{1}{2(n+\lambda)} \qquad i = 1,\ldots,n \tag{3.43}$$

where β is another parameter used to incorporate prior knowledge of the higher order moments of the state distribution. The optimal value of this is 2 for a Gaussian distribution [73].

3.3.3.2. Unscented Kalman Filter

The UKF is a filtering algorithm that uses the Unscented Transform to solve nonlinear problems in the form of a state-space representation:

$$\mathbf{x}_k = \mathbf{f}(\mathbf{x}_{k-1}) + \mathbf{q}_k$$
$$\mathbf{y}_k = \mathbf{h}(\mathbf{x}_k) + \mathbf{r}_k$$

where $\mathbf{x} \in \Re^n$ is a discrete state vector, $\mathbf{y} \in \Re^m$ is a discrete measurement vector, containing the samples of the input signal, and **q** and **r** are a Gaussian process and measurement noise with the zero mean and covariance matrices **Q** and **R**, respectively.

The procedure is started by defining an initial state vector $\mathbf{x}_0$ (starting guess of the algorithm), its initial covariance $\mathbf{P}_0$, process-noise covariance **Q** and measurement-

noise covariance **R**. These parameters are chosen empirically based on the knowledge of the accuracy of the model and the noise level in the process and measurements. The value of $\mathbf{P}_0$ depends on the initial guess of **x**; the more accurate the initial state vector is expected to be the smaller its initial covariance should be. The situation is similar to the case of **Q** and **R**; a more accurate model and "cleaner" measurements will require smaller values of **Q** and **R**, respectively. In other words the more confidence that the user has in the model and the measurements, the smaller the covariance matrices **Q** and **R** should be.

In the next step – the time update - a prediction is calculated based on the previous state and information about noise in the following way:

$$\boldsymbol{\chi}_{k-1} = [\overline{\mathbf{x}}_{k-1}, \overline{\mathbf{x}}_{k-1} \pm \sqrt{(n+\lambda)\mathbf{P}_{k-1}}] \tag{3.44}$$

$$\boldsymbol{\chi}^{*}_{k|k-1} = \mathbf{f}(\boldsymbol{\chi}_{k-1}) \tag{3.45}$$

$$\overline{\mathbf{x}}_{k|k-1} = \sum_{i=0}^{2n} W_i^{(m)} \boldsymbol{\chi}^{*}_{i,k|k-1} \tag{3.46}$$

$$\mathbf{P}_{k|k-1} = \sum_{i=0}^{2n} W_i^{(c)} [(\boldsymbol{\chi}^{*}_{i,k|k-1} - \overline{\mathbf{x}}_{k|k-1})(\boldsymbol{\chi}^{*}_{i,k|k-1} - \overline{\mathbf{x}}_{k|k-1})^T] + \mathbf{Q} \tag{3.47}$$

$$\boldsymbol{\chi}_{k|k-1} = [\overline{\mathbf{x}}_{k|k-1}, \overline{\mathbf{x}}_{k|k-1} \pm \sqrt{(n+\lambda)\mathbf{P}_{k|k-1}}] \tag{3.48}$$

$$\boldsymbol{\gamma}_{k|k-1} = \mathbf{h}(\boldsymbol{\chi}_{k|k-1}) \tag{3.49}$$

$$\overline{\mathbf{y}}_{k|k-1} = \sum_{i=0}^{2n} W_i^{(m)} \boldsymbol{\gamma}_{i,k|k-1} \tag{3.50}$$

where λ and the weights $W_i^{(m)}$ and $W_i^{(c)}$ are calculated as in the previous subsection. The measurements are taken into account in the next step, which is called measurement update:

$$\mathbf{P}_{\mathbf{yy}} = \sum_{i=0}^{2n} W_i^{(c)} [(\boldsymbol{\gamma}_{i,k|k-1} - \overline{\mathbf{y}}_{k|k-1})(\boldsymbol{\gamma}_{i,k|k-1} - \overline{\mathbf{y}}_{k|k-1})^T] + \mathbf{R} \tag{3.51}$$

$$\mathbf{P}_{\mathbf{xy}} = \sum_{i=0}^{2n} W_i^{(c)} [(\boldsymbol{\chi}_{i,k|k-1} - \overline{\mathbf{x}}_{k|k-1})(\boldsymbol{\gamma}_{i,k|k-1} - \overline{\mathbf{y}}_{k|k-1})^T] \tag{3.52}$$

$$\mathbf{K}_k = \mathbf{P}_{xy} \mathbf{P}_{yy}^{-1} \tag{3.53}$$

$$\mathbf{P}_k = \mathbf{P}_{k|k-1} - \mathbf{K}_k \mathbf{P}_{yy} \mathbf{K}_k^T \tag{3.54}$$

$$\bar{\mathbf{x}}_k = \bar{\mathbf{x}}_{k|k-1} + \mathbf{K}_k (\mathbf{y}_k - \bar{\mathbf{y}}_{k|k-1}) \tag{3.55}$$

where $\mathbf{P}_{yy}$ is the measurement covariance, $\mathbf{P}_{xy}$ is the cross-covariance, $\mathbf{K}_k$ is the Kalman gain and $\mathbf{y}_k$ is the measurement taken during the kth step.

The strongest advantage of this approach is that it does not require the linearization of a nonlinear system model. The biggest benefit of this, except the ease of implementation, is the increased accuracy in comparison with the EKF. The method captures the posterior mean and covariance accurately to the 3rd order of any nonlinearity [73].

On the other hand, when the selected values for the covariance matrices are not appropriate, the filter can became unstable and diverge. An attempt to address this problem of tuning the method was successfully made in [67]. However, the authors do not mention the computational burden, which will certainly be significantly increased in the new approach. This is an important fact, taking into account that the UKF, even in its basic form, is already quite demanding, due to considerable number of operations (including Cholesky factorization) performed for each step.

3.4. Results

3.4.1. Static Test

The purpose of this test was to evaluate the steady-state performance of the UKF. Voltage (3.56) and current (3.57) signals have been generated to produce the instantaneous power signal.

$$u(t) = 1 \cdot \cos(\omega t) \text{ p.u.} \tag{3.56}$$

$$i(t) = 0.9 \cdot \cos(\omega t - \frac{\pi}{6}) \text{ p.u.} \tag{3.57}$$

$$\omega = 2\pi \cdot 50 \text{ rad/s} \tag{3.58}$$

In Figure 3-2 the instantaneous values of voltage $u(t)$, current $i(t)$ and the instantaneous power $p(t) = u(t) \cdot i(t)$, are presented. For clarity, only a selected time interval t = 0.2-0.26 s is shown.

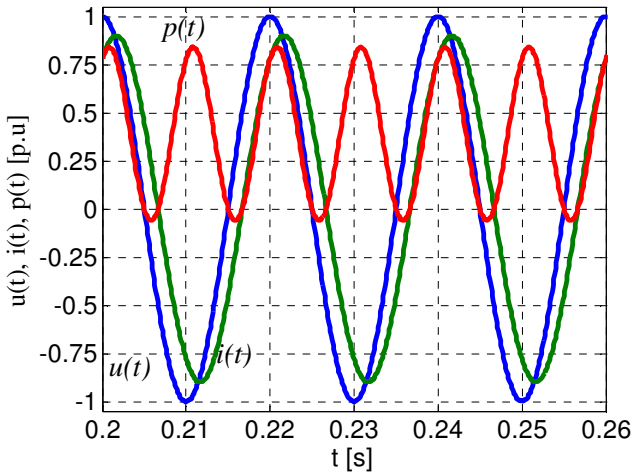

Figure 3-2: Instantaneous voltage, current and power signals

From (3.56)-(3.57) the exact values of the unknown power components can be obtained: S = 0.45 p.u., P = 0.3897 p.u., Q = 0.225 p.u. and $\cos\varphi = \cos\left(\pi/6\right) \approx 0.866$.

For the purposes of the estimation in this test example the measurement covariance **R** was set to a small value of 10^{-14}. Such a value was selected empirically, taking into account the noise-free conditions. The UKF algorithm successfully estimated the exact results, as can be concluded from Figure 3-3 and Figure 3-4. In both figures a short convergence period can be observed at the beginning of the estimation.

Using the same signals from the above test, the sensitivity to random noise is further investigated through a comparison with the interpolated DFT (Figure 3-5). The observation window used to evaluate the DFT was T_{dw} = 80ms (the smallest possible window that can ensure optimal results). The sampling frequency was f_s = 1600 Hz. In Figure 3-6 the algorithms sensitivity to random noise for a constant measurement covariance is presented. Figure 3-7 presents the results of the same test but with the measurement covariance adjusted according to information about the signal (measurement covariance **R** was manually decreased for less distorted measurements). In both cases the accuracy is acceptable; however, it should be noted that the measurement covariance matrix **R** is a crucial factor in influencing the accuracy of the estimation in noisy conditions. Note that the signal-to-noise ratio

(SNR) is defined as follows:

$$SNR = 20\log(A/(\sqrt{2}\sigma)) \tag{3.59}$$

where $A/\sqrt{2} = A_{RMS}$ is the root mean square value of the processed signal and σ is the standard deviation of the *white noise*. From Figure 3-6 and Figure 3-7 it can be concluded that by incorporating knowledge about the noise one can achieve better results and even without this adjustment the accuracy is still acceptable. The interpolated DFT has accuracy similar to that of the UKF when the measurement covariance is constant. However, this similarity only exists when the fundamental frequency is equal to the nominal value. For off-nominal frequency the accuracy of the interpolated DFT is worse, this is can be seen in Figure 3-8, which presents the sensitivity to frequency deviations for both the UKF and the DFT.

The errors presented here are defined as the maximum of the absolute differences between the estimated frequency (or active power) and its true values over a specified observation period (in this case the last 32 estimates were assessed). The relative frequency errors were calculated as follows (the equivalent formulas were used for the active power):

$$\varepsilon_f = \frac{\max\left|f_{estimate} - f_{exact}\right|}{f_{exact}} \cdot 100\ \% \tag{3.60}$$

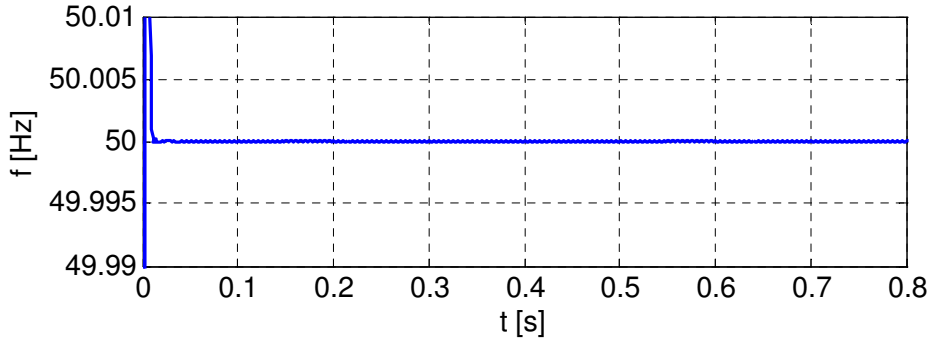

Figure 3-3: Estimated frequency

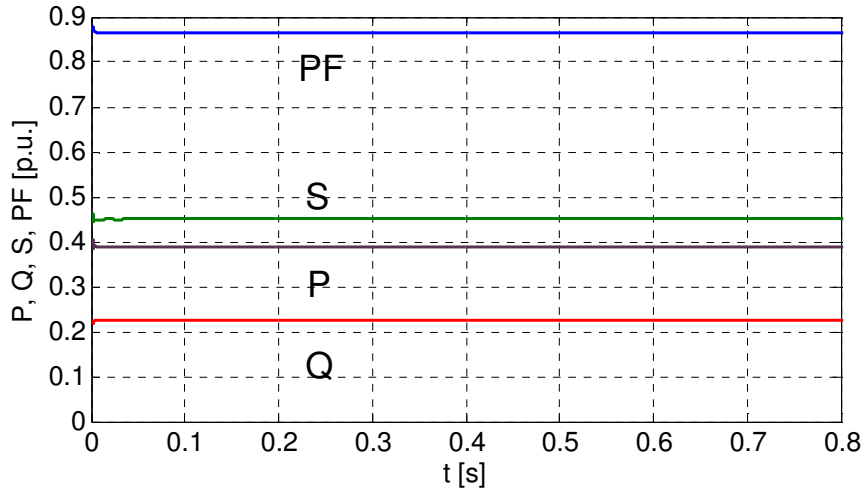

Figure 3-4: Estimated power components: active (*P*), reactive (*Q*) and apparent power (*S*) and power factor (*PF*)

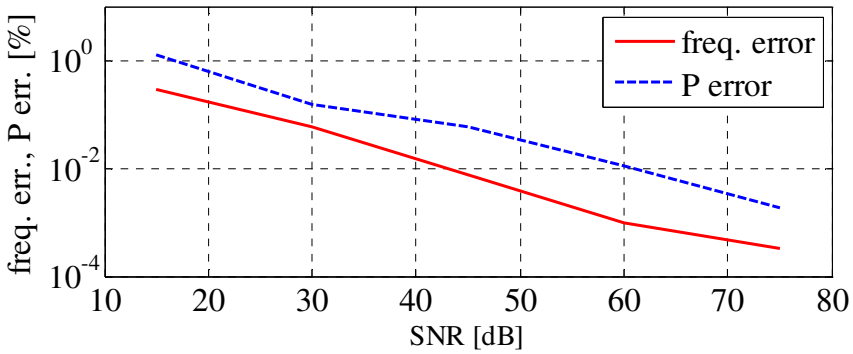

Figure 3-5: Maximal frequency and active power error versus signal to noise ratio for interpolated DFT

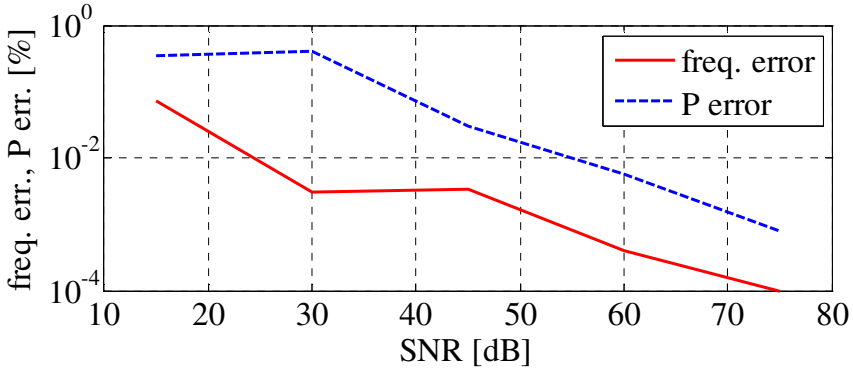

Figure 3-6: Maximal frequency and active power error versus signal to noise ratio for constant measurement covariance

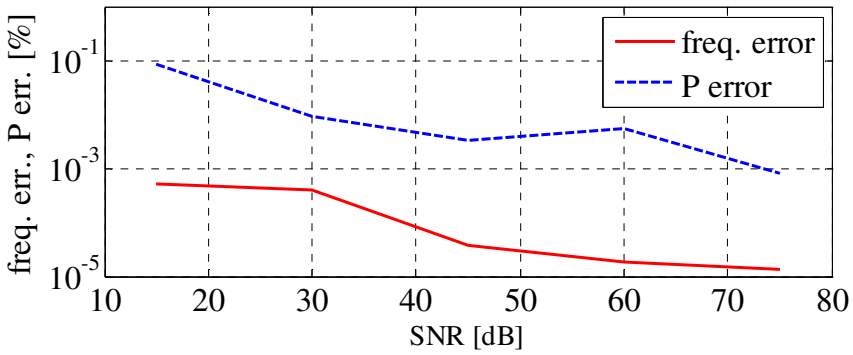

Figure 3-7: Maximal frequency and active power error versus signal to noise ratio for adjusted measurement covariance

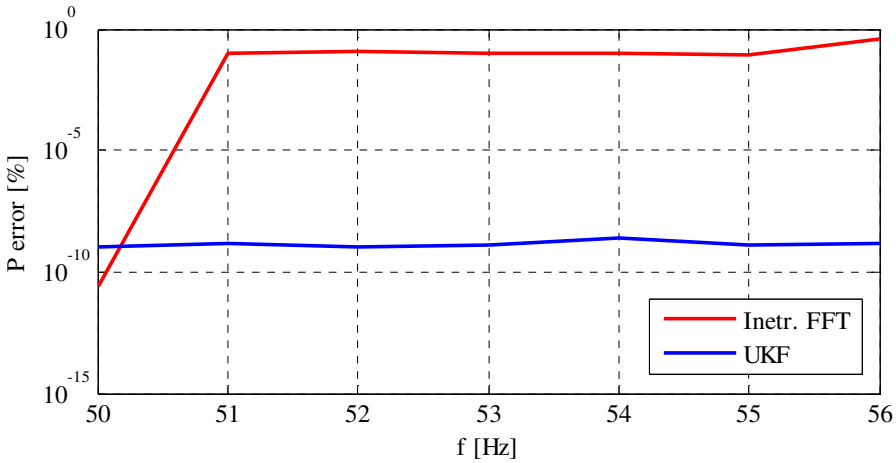

Figure 3-8: Sensitivity to frequency deviation

3.4.2. Cramer-Rao Lower Bound

The *estimation noise efficiency* was compared to the Cramer-Rao Lower Bound (CRLB), which provides information about the minimum variance of an estimator of a deterministic parameter:

$$\mathrm{var}(\hat{x}) \geq \frac{1}{I(x)} \tag{3.61}$$

$$I(x) = E\left[\left(\frac{\partial \log f(y;x)}{\partial x}\right)^2\right] \tag{3.62}$$

where $I(x)$ is the Fisher Information, $E[]$ is the expected value and $f(y;x)$ is the likelihood function of the parameter x for a given outcome y. The CRLB has been calculated according to the *zero-order approximation* [74].

Figure 3-9 presents a comparison of the RMS error of the angle estimation (first element of the vector of unknown parameters) and the root square of its CRLB. The RMS error was obtained in the following way:

$$E_{RMS,k} = \sqrt{1/M \sum_{m=1}^{M} (x_{k,m} - \hat{x}_{k,m})^2} \tag{3.63}$$

where M is the number of Monte Carlo simulations (M=100), $x_{k,m}$ is the true value of the parameter at the discrete time k and $\hat{x}_{k,m}$ is the estimated value of the parameter at the discrete time k. The results show that the variance of the estimator is very close to the CRLB for the different levels of noise, which indicates that the algorithm is efficient. Similar results were obtained for the three remaining unknown parameters.

In this application, the UKF has not demonstrated any gain instability. In practical applications, where the parameters of signals constantly change, the elements of the covariance matrix $\mathbf{P}_k$ do not become dangerously low, which ensures stable execution of the algorithm.

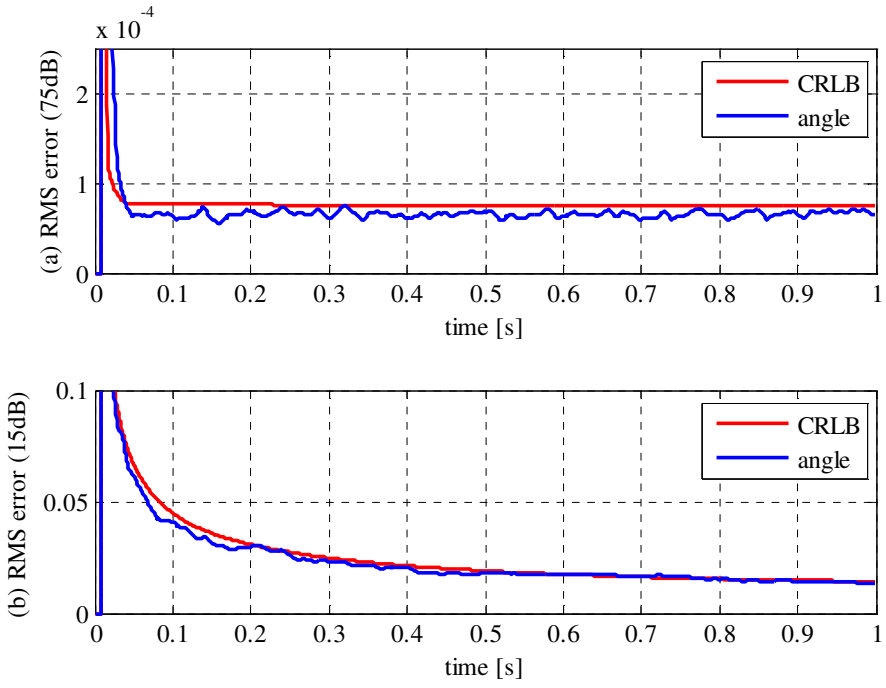

Figure 3-9: Angle estimation error versus its estimated CRLB: (a) SNR=75dB, (b) SNR=15dB

3.4.3. Sensitivity to Higher Harmonics

The parameter model (3.3) does not include the higher harmonics that could exist in a real instantaneous power signal $p(t)$. Let us analyse the case in which the following distorted voltage and current signals are processed:

$$u(t) = 1 \cdot \cos(\omega t) + U_3 \cdot \cos(3\omega t) + U_5 \cdot \cos(5\omega t) \tag{3.64}$$

$$i(t) = 1 \cdot \cos(\omega t - \frac{\pi}{6}) + I_3 \cdot \cos(3\omega t - \frac{\pi}{6}) + I_5 \cdot \cos(5\omega t - \frac{\pi}{4}) \tag{3.65}$$

where U_3 and U_5 are the amplitudes of two higher harmonics that exist in the voltage signal, whilst I_3 and I_5 are the higher harmonics components included in the current signal. Table 3-1 and Table 3-2 contain the results of the sensitivity analysis of frequency estimation and active power estimation for various current and voltage harmonic distortions. THD_I and THD_U are the current and voltage total harmonic distortion factors, respectively, ε_f is the relative error of the estimated frequency, and ε_P is the relative error for the active power. Table 3-5 presents the amplitudes of the higher harmonics that were used to achieve the desired THD levels. It is assumed that the current distortions are more severe than the voltage distortions. The errors are determined in the same way as in the previous subsections (3.60). From Table 3-1 and Table 3-2, it is obvious that the errors for the estimated frequency are significantly smaller than those for the estimated active power. Table 3-3 and Table 3-4 contain results of the same test but with the estimation performed using the interpolated DFT. Although the method does take into account the higher harmonics, the accuracy of the estimation of active power decreases significantly for higher THD levels. What is more, for off-nominal frequencies the accuracy of the estimation will decrease further (Figure 3-8).

The algorithm could be improved by introducing higher harmonics into the voltage and current models. Obviously, this would cause the model to become more complex and the number of unknown model parameters would increase.

Table 3-1: Relative errors versus signal distortions for estimated frequency (UKF)

ε_f [%]		THD_U [%]			
		0	**7.071**	**14.142**	**28.284**
THD_I [%]	**0**	4.79E-10	0.0035	0.0072	0.015
	14.142	0.0035	0.0044	0.007	0.0142
	28.284	0.0066	0.0054	0.0076	0.0152

Table 3-2: Relative errors versus signal distortions for estimated active power (UKF)

ε_P [%]		THD_U [%]			
		0	**7.071**	**14.142**	**28.284**
THD_I [%]	**0**	4.04E-10	0.0332	0.0617	0.1327
	14.142	0.0437	1.6165	3.2261	6.4289
	28.284	0.0944	3.2157	6.386	12.7325

Table 3-3: Relative errors versus signal distortions for estimated frequency (Interpolated DFT)

ε_f [%]		THD_U [%]			
		0	**7.071**	**14.142**	**28.284**
THD_I [%]	**0**	1.12E-11	1.25E-11	1.41E-11	1.74E-11
	14.142	1.61E-11	1.73E-11	1.89E-11	2.14E-11
	28.284	2.23E-11	2.34E-11	2.45E-11	2.68E-11

Table 3-4: Relative errors versus signal distortions for estimated active power (Interpolated DFT)

ε_P [%]		THD_U [%]			
		0	**7.071**	**14.142**	**28.284**
THD_I [%]	**0**	2.64E-11	2.77E-11	3.01E-11	3.72E-11
	14.142	3.40E-11	0.9082	1.8588	3.633
	28.284	4.37E-11	1.8165	3.633	7.266

Table 3-5: Harmonic composition of the test signal

THD [%]	A_3	A_5
0	0	0
7.071	0.05	0.05
14.142	0.1	0.1
28.284	0.2	0.2

3.4.4. Dynamic Test

To analyse the dynamic properties of the algorithm, in the following test example the signal parameters (amplitude and frequency) are dynamically changed in a wide range. Here, sinusoidal voltage and current signals were processed. In the steady state prior to the selected disturbance (e.g. dynamic change of signal parameters) the voltages and currents were pure sinusoidal signals, defined with V_m=1p.u. and I_m=0.8p.u., φ=30^0 and f=50Hz. At $t_d = 0.2$ s both current and voltage amplitudes were step changed. The new values were as follows: V_m=0.9p.u. (-10% step change) and I_m=0.96p.u. (+20% step change). Simultaneously to these step changes in the signal amplitudes, at $t_d = 0.2$ s, the frequency of both signals started to deviate from its nominal value, as follows:

$$f = 50 + 2\sin(2\pi \cdot 2 \cdot (t - t_d)) + 2 \cdot (t - t_d) \text{ [Hz]} \tag{3.66}$$

In Figure 3-10 the estimated and true frequencies are presented. It can be noted that the estimated frequency is practically the same as the true value, even during the dynamic variation of the frequency, which demonstrates the very fast response of the filter. However, some delay can be detected, as demonstrated in Figure 3-10b, in which the *absolute errors* caused by the delay are presented.

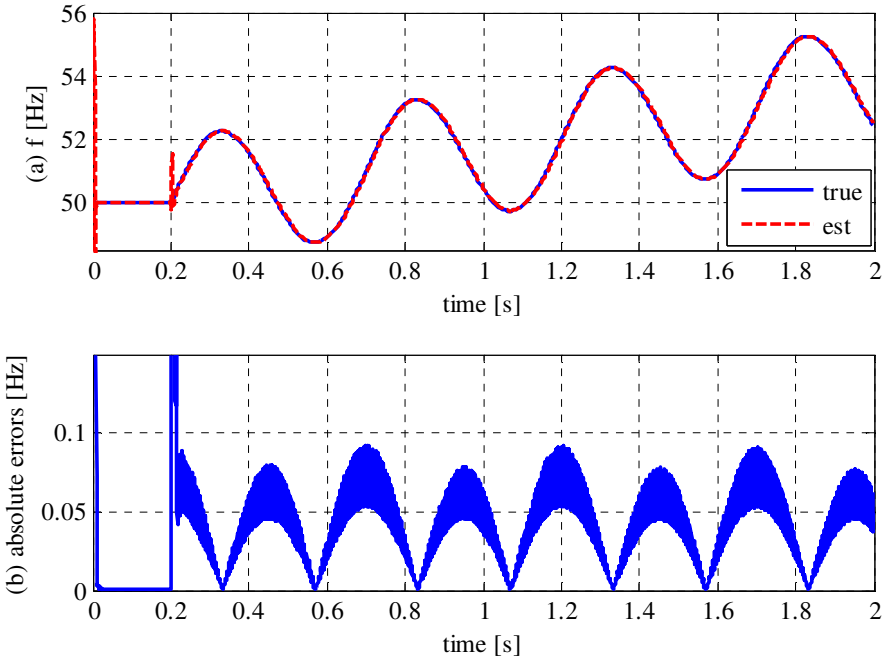

Figure 3-10: Estimated frequency: (a) true value versus estimated (b) absolute error of estimated frequency

In Figure 3-11 the estimated apparent power obtained using the UKF and the estimated apparent power obtained using the interpolated DFT are presented. The observation window used to evaluate the DFT was again T_{dw} = 80ms and the sampling frequency was f_s = 1600 Hz. The UKF estimates are more accurate and demonstrate superior convergence properties. Results of very similar quality were obtained for the remaining two power components – active and reactive power. It should be noted that the presented algorithm simultaneously estimates both the power components and the frequency, so it can also be used as an efficient frequency-meter.

To demonstrate the convergence properties of the UKF, Figure 3-12 presents the estimated active power P immediately after the step change. In the same figure the impact of the selection of the measurement covariance matrix $\mathbf{R} = diag\,(\mathbf{r}^2)$ is presented. It can be concluded that the reduced sensitivity to noise (larger values for **r**) reduces the speed of the algorithm's convergence and introduces delays.

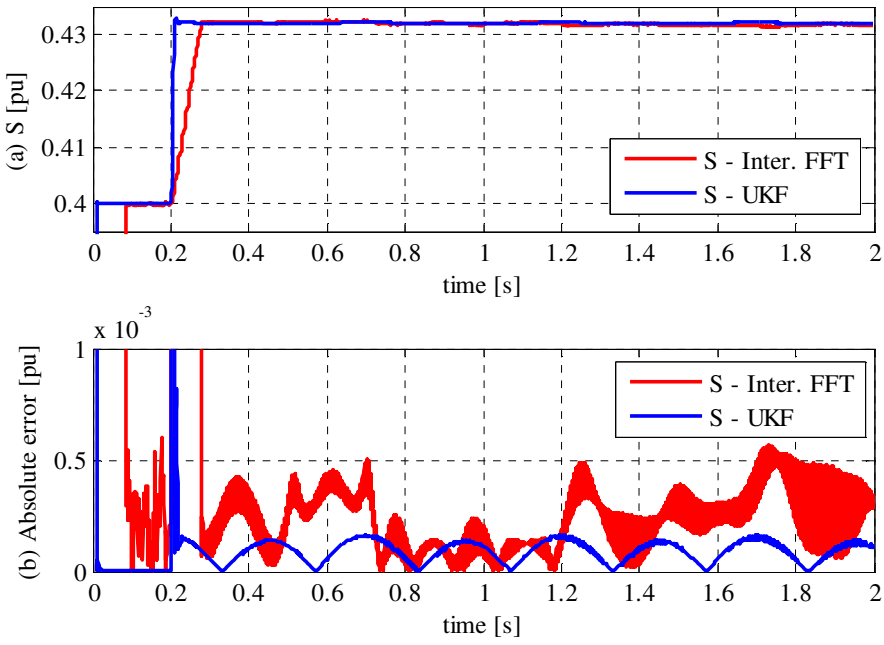

Figure 3-11: Estimated apparent power: (a) estimation result; (b) absolute error

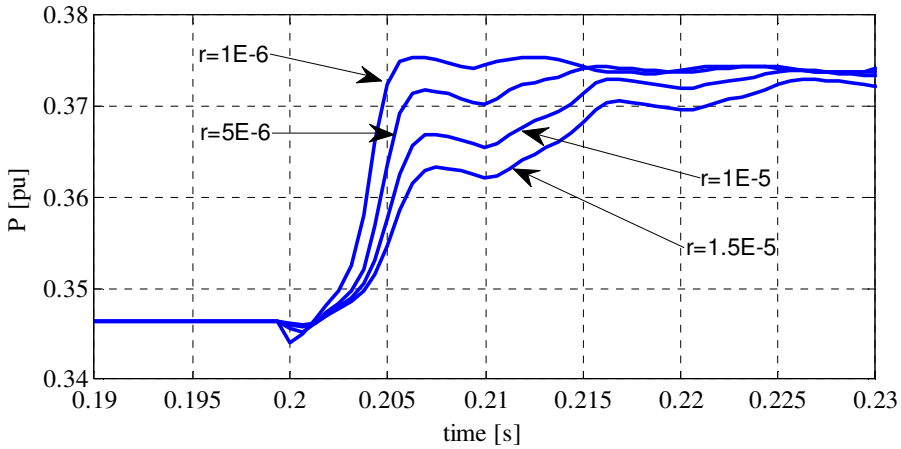

Figure 3-12: Estimated active power for different measurement covariance

3.4.5. Laboratory Tests

In this test, signals recorded from a physical network model under laboratory conditions have been used in the evaluation of the performance of the new algorithm. Here a synchronization of two active networks is used as an illustrative test example. In the experiment presented, data records were obtained by using a modern data acquisition digital system [75]. Voltages and currents were recorded with the sampling frequency f_s=1 kHz. In Figure 3-13, a single-line diagram of a synchronous generator SG connected over a block transformer T to the local load is presented. By closing the circuit breaker, CB, at t = 0 s the single generator system is connected over the line to the infinite bus U_{INF}. Before the synchronization, the SG had supplied only the local load. After the synchronization, the SG delivered electric power to the external network.

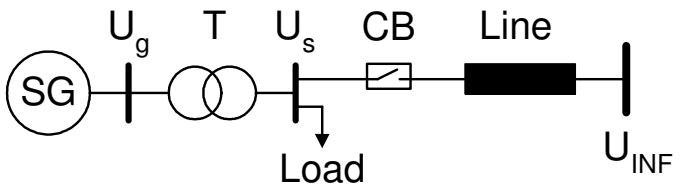

Figure 3-13: Laboratory setup

The synchronisation of two networks or a generator to an external grid is a standard procedure which must be carried out according to the synchronisation requirements. Essentially, a successful synchronisation can be achieved if the voltage phasors (the voltage amplitudes and phase angles) and frequencies of both networks are

approximately the same. If this is not the case, the synchronisation is followed by large currents, voltage drops and frequency oscillations. In real networks, the synchronisation of two networks is monitored by the *Synchro-Check device* [76]. If Synchro-Check identifies that conditions for the successful synchronisation are not fulfilled it will generate a blocking signal to the circuit breaker over which the synchronisation is being attempted.

In the test presented here, the corresponding phasors and frequencies of the two separated systems were not exactly the same at the instant of synchronization. As a consequence, an electromechanical transient process was initiated. During this transient process, currents and voltages were distorted and the frequency was oscillating. The measurement covariance in this case was increased to 10^{-1} to filter out the noise and harmonic distortion.

In Figure 3-14 the voltage and current signals during an arbitrarily selected period are presented. It is obvious that both signals are distorted. Thus, the estimation of power components was carried out during severe signal distortions and during off-nominal frequency conditions. In Figure 3-15 the input voltage and current signals during the entire observation interval are presented. Significant amplitude changes can be seen in both signals. They are particularly dominant in the current signal. Physically, the oscillations are a consequence of electromechanical oscillations between the generator and the large external network.

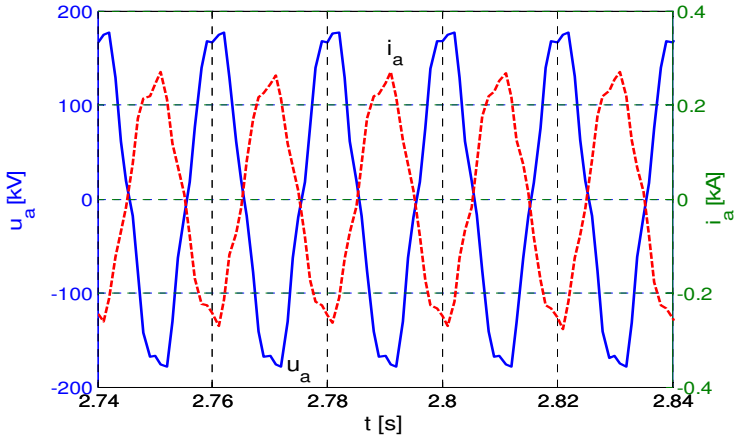

Figure 3-14: Phase *a* voltage and current during an arbitrarily chosen time period

As previously described, the instantaneous power signal was first obtained by multiplying the voltage and current signals together. The instantaneous power

obtained in this way was then processed using the UKF, which delivered the unknown power components and the power factor. In Figure 3-16 the estimated generator frequency is presented. After the synchronization, the generator frequency began to change so that it would match the system frequency. To offer a source of comparison, the frequency estimated by using the STLS method is also presented in Figure 3-16.

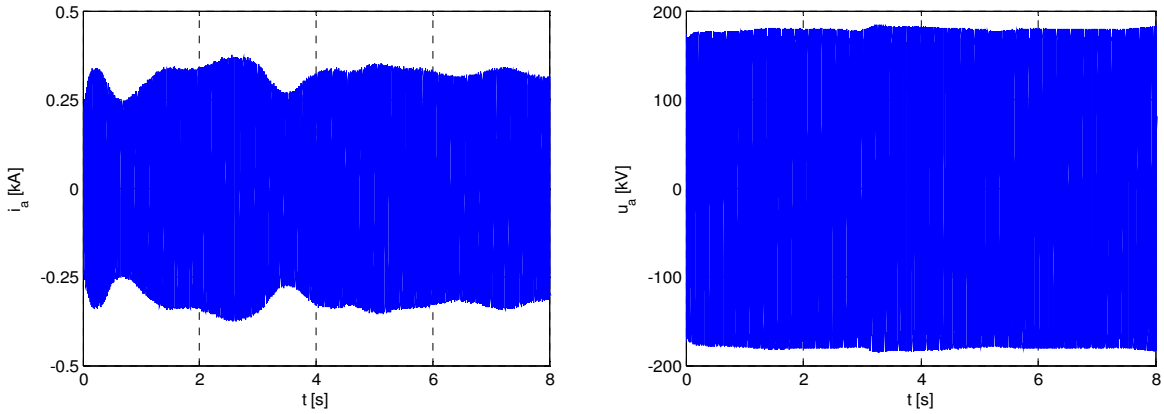

(a) (b)

Figure 3-15: Phase *a* instantaneous signals: (a) current; (b) voltage

From Figure 3-16 it can be concluded that both algorithms deliver very similar results. This is proof that the UKF is capable of precise frequency tracking during transient processes and severe signal distortions in power systems.

In Figure 3-17 to Figure 3-19 the estimated power components are presented. Again, a high level of correlation between the estimates obtained by using the STLS and the new algorithm has been achieved. After the synchronization, the generator starts to deliver electrical energy to the external grid. In terms of the estimation of power components the STLS algorithm has been designed according to the definitions given in the IEEE Standard 1459-2000 [77], [78].

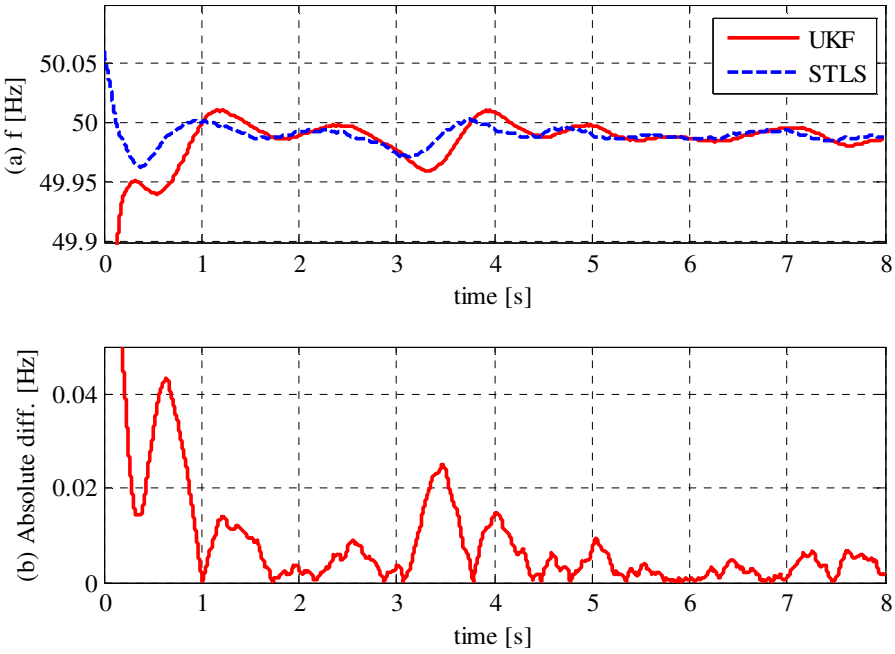

Figure 3-16: Estimated generator frequency: (a) estimation result; (b) absolute difference

During the laboratory testing a precise PQ monitoring device was not available, so an exact comparison and judgment of the results obtained was not possible. The steady-state estimated active powers were approximately the same as the values obtained by using the analogue power meter available in the laboratory.

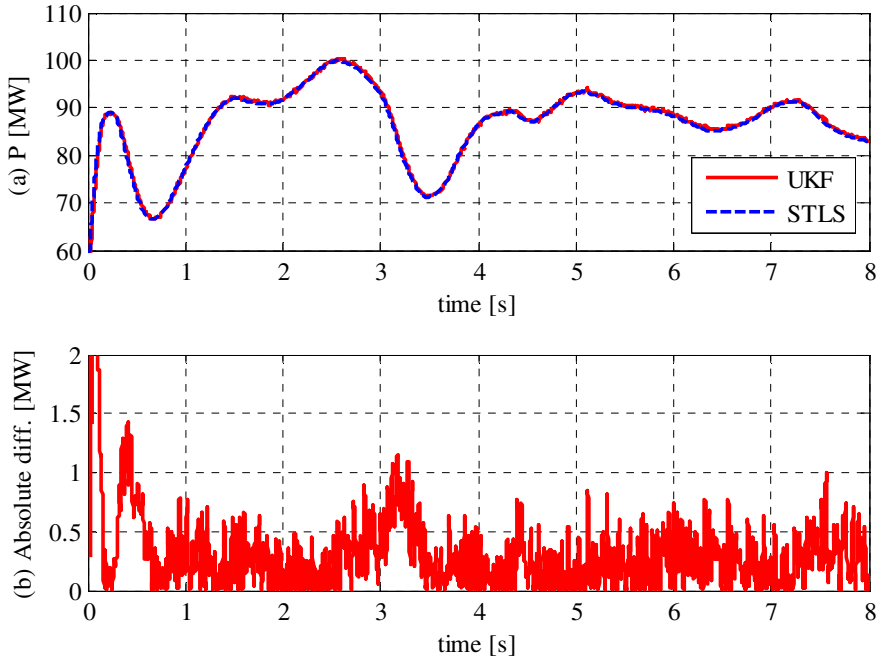

Figure 3-17: Active Power (P): (a) estimation result; (b) absolute difference

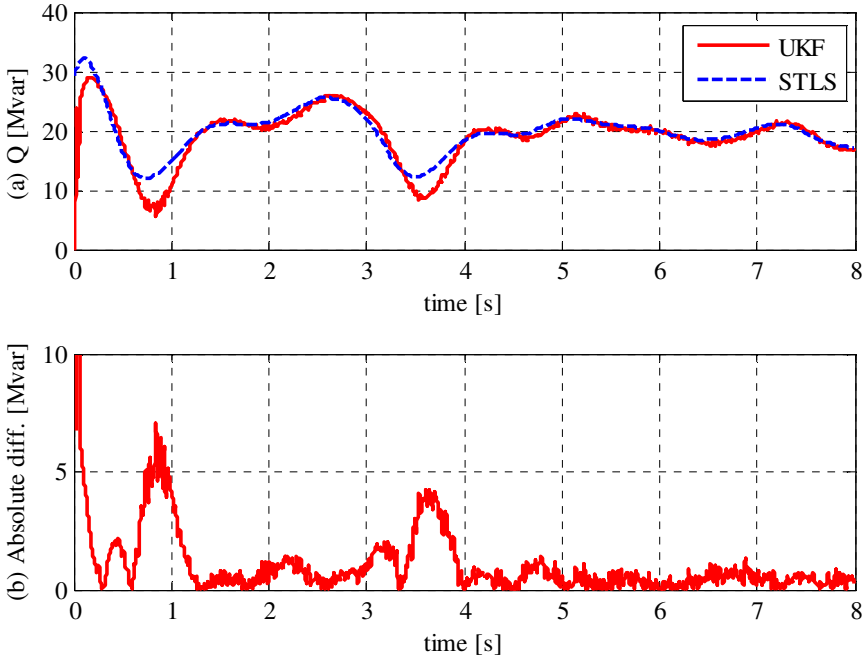

Figure 3-18: Reactive Power (Q): (a) estimation result; (b) absolute difference

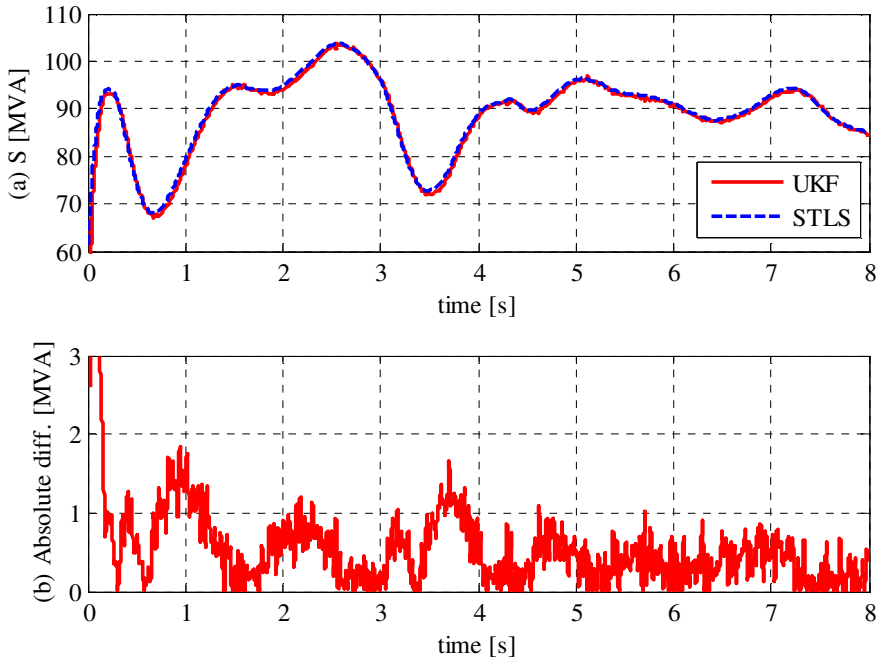

Figure 3-19: Apparent Power (S): (a) estimation result; (b) absolute difference

Figure 3-20 shows the THD values of current and voltage obtained using the STLS algorithm, which takes into account higher harmonics in the signal. From this figure it can be concluded that the UKF gives very good results even in cases when THD values of the current and voltage are around 10%.

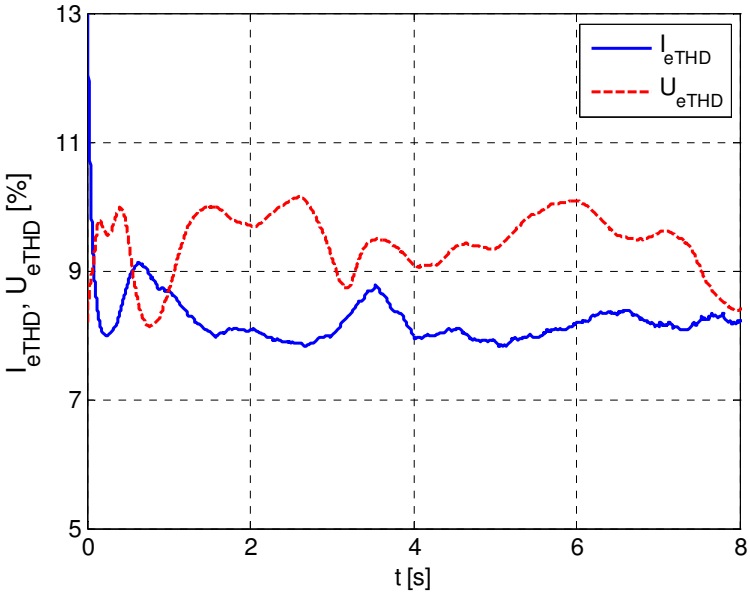

Figure 3-20: THD values of current and voltage obtained by the STLS

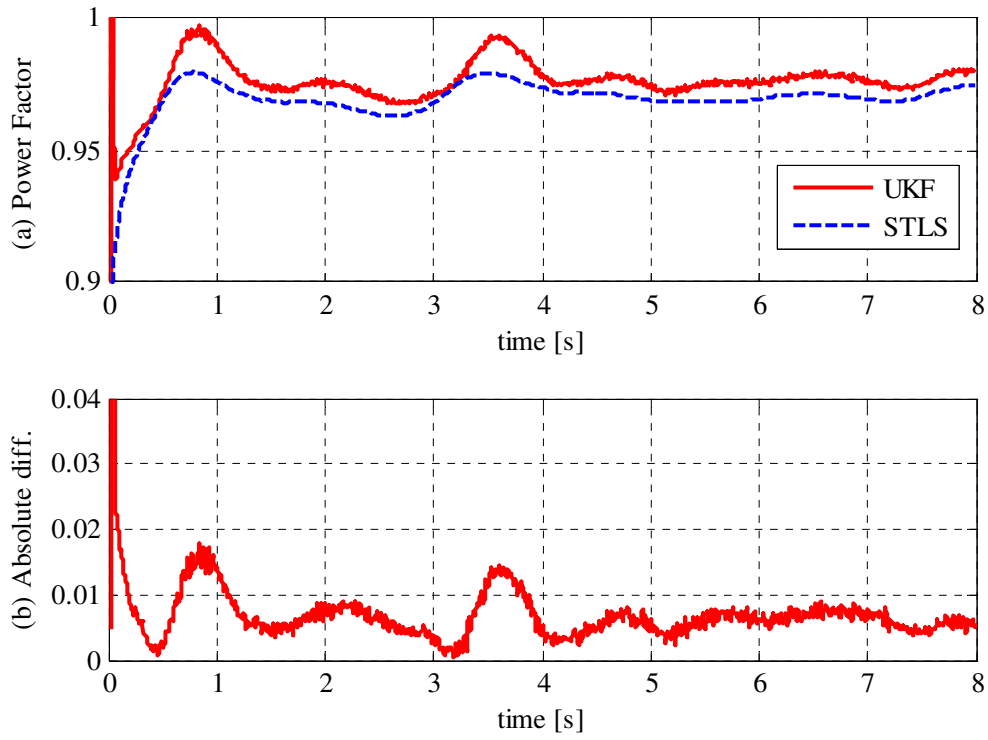

Figure 3-21: Power Factor: (a) estimation result; (b) absolute difference

As a by-product, the power factor *PF* can be easily calculated from the estimated power components: *PF* = *P*/*S*. The results of this are is presented in Figure 3-21.

In Figure 3-16 to Figure 3-21 a delay between the estimates obtained using the two methods can be noticed. It is known that different estimation methods introduce

different levels of delay. The delay depends on the convergence properties of the estimator used, as well as on the selection of the estimator parameters. The UKF is a recursive estimator, whereas the STLS method is a non-recursive one (in this case the sequence of samples belonging to the predetermined data window are simultaneously processed and the selection of the data window size affects the delay level). The parameters of the UKF were tuned to reduce the level of noise (here the harmonic distortions, which were not considered in the signal model are treated as random noise). This requirement affected the convergence properties of the UKF and introduced delays in the estimation process, the size of which depends on the selected value of the measurement covariance matrix **R** (Figure 3-12). The delay introduced by the STLS algorithm was compensated for in the presented figures by shifting the plots by the length of the selected data-window (80 ms).

3.4.6. Computational Burden

The UKF is a recursive method so it is suitable for real-time applications. For online algorithms the critical issue is the computational burden. In the case of the UKF estimator, the average execution time (based on 100 trials) for 1600 samples (1 s of data sampled at 1.6 kHz) is 0.2814 s (with standard deviation of 0.0016 s). This gives an upper limit of sampling frequency of approximately 5.6 kHz. This result has been obtained in MATLAB 7.10 on a Pentium class PC with a 2.4GHz processor and 3GB of RAM. Additionally, absolute performance has been assessed by estimating the number of Floating-Point Operations (FLOPS). Each iteration of the algorithm takes approximately 2500 FLOPS, which means that approximately 2500 adders/multipliers are required to implement the routine.

3.5. Conclusions

From the results presented in this section it is clear that the estimation of signal parameters will always be a trade-off between accuracy, speed and computational requirements. Depending on the type of application, the priorities may be very different. The Unscented Kalman Filter has been proven to be very accurate as its performance is very close to the Cramer-Rao Lower Bound. However, the overall

accuracy of the result will rely heavily on the level of detail included in the assumed signal model. In the case presented in this work the model contains only the fundamental component, so as to minimize the CPU burden. In this way a real-time implementation of the method is ensured at the cost of accuracy in the presence of heavy harmonic distortion. It is said that the higher harmonics are treated as noise and filtered out by the algorithm. However, due to the periodical, rather than random, nature of harmonics, this approach can minimize the impact of these components, but not fully eliminate it. The proposed signal model can be easily expanded to include any desired harmonics, but every time such a modification takes place the required computational resources need to be reassessed to ensure that one iteration of the procedure will be executed within one sampling period for real-time applications. This shows that the approach can be flexible in terms of the trade-off between accuracy and CPU demand.

Another important feature of the UKF is its recursive nature. Traditional approaches use a sliding window technique or they require pre-filtering, which is also based on a defined data window. This introduces a constant delay usually of at least one fundamental period. Additionally, signal dynamics can be smoothed due to averaging over the selected data window. It should be noted that this phenomenon may seem to be an advantage because of the noise-filtering effect, but it will also somewhat distort fast changes in the signal (compare the long ramp estimated by the Interpolated DFT and the step change estimated by the UKF in Figure 3-11). Both of the iterative methods used in this project as a source of comparison required data windows of 80ms to ensure optimal results. The UKF on the other hand, shows much better convergence properties, which enables fast and accurate tracking of dynamically changing signals.

The control over the described properties of the UKF is achieved by manipulating the covariance matrices **Q** and **R**. Selection of these two parameters is crucial to obtain stable and optimal results. The matrix **Q** allows the accommodation of model inaccuracies and the expected variations in the values of the estimated parameters, whereas matrix **R** reflects the expected variations in the measurements (noise). A disadvantage of this approach is related to the fact that some knowledge of the measured signal is necessary to tune the parameters optimally. In this work the

covariance matrices were selected empirically based on a number of tests (Appendix C). Some attempts have been made towards adaptive approaches, where the parameters are tuned using a separate optimization method. In [67] a Particle Swarm Optimization (PSO) is used to tune the UKF. However, the authors do not share any information about the computational burden of their algorithm, which will certainly be considerably increased by the use of PSO (PSO is rather a demanding technique). This leads to the conclusion that although the method can show very good performance, its tuning may become an issue or be costly in terms of CPU demand.

4. Estimation of Load Model Parameters

4.1. Introduction

Estimation of load model parameters, like any other estimation process, can be demanding and challenging. Problems of a nonlinear nature may present multiple local minima, which in turn may cause a premature convergence to the closest local optimum. Such behaviour is quite typical in the case of some of the more complex load models that have been described in [79]. This was the main reason why researchers looked for tools other than the traditional Nonlinear Least Squares (NLS) methods [28]-[33], which are known for their strong sensitivity to the initial guess. Artificial Intelligence (AI) techniques [19]-[22] were capable of finding the global solution to the problem but did not guarantee it. Finally, Hybrid methods [23]-[27], a combination of AI and NLS, showed the best results of all; however, their reliability still left room for improvement.

The biggest challenge in this field is to ensure, or at least increase, the probability of finding the global minimum. For this reason, the reliability of the existing methods should be assessed and a different, possibly better, method proposed and thoroughly tested. This is achieved with an Improved Particle Swarm Optimization (IPSO) algorithm – an AI type method, variations of which have been applied to other fields in power systems [80]-[83]. The evaluation and comparison of the methods have been carried out using two of the most widely used dynamic load models – the Exponential Recovery Load (ERL) model [3], [4], [7], [9], [28], [29], [31] and the Composite Load (CL) model [10], [21], [23]-[25], [35] and [39]. The former is mostly used to approximate loads that recover slowly over a time frame from several seconds to tens of minutes. The latter, on the other hand, is employed in cases where Induction Motors (IM) are a dominant component. Taking into account that these machines are responsible for consumption of approximately 60% to 70% of the total energy supplied by a power system, the CL model will quite often be applicable [1].

4.2. Load Models

4.2.1. Exponential Recovery Load Model

As mentioned before, the modelling of power system loads that tend to recover their power over time require the more sophisticated approach that is offered by dynamic models. A typical response of such a model to a voltage step change is given in Figure 4-1.

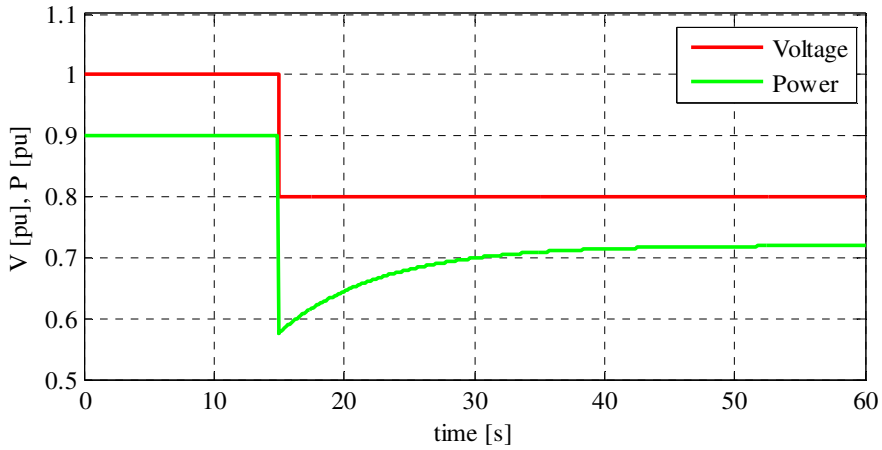

Figure 4-1: Typical response of a dynamic model to a voltage step change

The power demand of the ERL model is related to voltage and time through the following equations [3]:

$$T_P \dot{z}_P = \left(\frac{V}{V_0}\right)^{\alpha_s} - z_P \left(\frac{V}{V_0}\right)^{\alpha_t} \tag{4.1}$$

$$P_d = z_P P_0 \left(\frac{V}{V_0}\right)^{\alpha_t} \tag{4.2}$$

$$T_Q \dot{z}_Q = \left(\frac{V}{V_0}\right)^{\beta_s} - z_Q \left(\frac{V}{V_0}\right)^{\beta_t} \tag{4.3}$$

$$Q_d = z_Q Q_0 \left(\frac{V}{V_0}\right)^{\beta_t} \tag{4.4}$$

where z_P and z_Q are the state variables, T_P and T_Q are the recovery time constants, α_s and β_s are the static exponents and α_t and β_t are the transient exponents. The vectors of the unknown parameters to be estimated are as follows:

$$\begin{aligned}\theta_P &= [\alpha_s, \alpha_t, T_P] \\ \theta_Q &= [\beta_s, \beta_t, T_Q]\end{aligned} \tag{4.5}$$

The exponential recovery model can be understood as simply a static exponential model the characteristic of which will change over time.

4.2.2. Composite Load Model

The Composite Load (CL) model is a voltage dependant dynamic load model represented by a 3rd order Induction Motor (IM) model connected in parallel with a Static Load model. In [1] a comprehensive and thorough derivation of the most commonly used IM model is given. For representation in power system stability studies, the stator transients have been neglected, which results in the following three differential equations describing the model:

$$\begin{aligned}\frac{dv_d^{'}}{dt} &= -\frac{1}{T_0^{'}}\left[v_d^{'} + (X - X^{'})i_{qs}\right] + \frac{d\theta_r}{dt}v_q^{'} \\ \frac{dv_q^{'}}{dt} &= -\frac{1}{T_0^{'}}\left[v_q^{'} - (X - X^{'})i_{ds}\right] - \frac{d\theta_r}{dt}v_d^{'} \\ \frac{d\omega_r}{dt} &= \frac{1}{2H}(T_e - T_m)\end{aligned} \tag{4.6}$$

which are followed by two algebraic equations representing the stator currents:

$$\begin{aligned}i_{ds} &= \frac{1}{R_s^2 + X^{'2}}\left[R_s(v_d - v_d^{'}) + X^{'}(v_q - v_q^{'})\right] \\ i_{qs} &= \frac{1}{R_s^2 + X^{'2}}\left[R_s(v_q - v_q^{'}) - X^{'}(v_d - v_d^{'})\right]\end{aligned} \tag{4.7}$$

Where the *d* and *q* indices indicate the *d*-axis and *q*-axis of the *d-q* reference frame,

respectively, the *s* and *r* indices indicate the stator and rotor state/parameter, *v* is the stator voltage in pu, *v'* is the voltage behind the transient reactance in pu, *H* is the inertia constant in s, ω_r is the rotor speed in pu, T'_0 is the transient open circuit time constant (4.8) in s, X' is the transient reactance (4.9) in pu, R_s is the stator resistance in pu, *X* is a sum of the stator reactance X_s and the magnetizing reactance X_m, in pu, T_e is the electromagnetic torque in pu, T_m is the load torque in pu and $\frac{d\theta_r}{dt}$ is the slip speed (4.10) in rad/s.

$$T_0^{'} = \frac{X_r + X_m}{R_r \omega_s} \tag{4.8}$$

$$X^{'} = X_s + \frac{X_m X_r}{X_m + X_r} \tag{4.9}$$

$$\frac{d\theta_r}{dt} = \omega_s - \omega_r \tag{4.10}$$

where R_r and X_r are the rotor resistance and reactance, respectively (both in pu), ω_s and ω_r are the synchronous and rotor speed, respectively (both in rad/s) and θ_r is the angle by which the *d*-axis leads the phase *A* axis of the rotor.

The electromagnetic (T_e) and load (T_m) torques are calculated as follows:

$$T_e = v_d^{'} i_{ds} + v_q^{'} i_{qs} \tag{4.11}$$

$$T_m = (A\omega_r^2 + B\omega_r + C)T_0 \tag{4.12}$$

where T_0 is the nominal torque at nominal speed in pu, *A*, *B* and *C* denote the torque coefficients: proportional to the square of the speed, proportional to the speed and constant coefficient, respectively. In addition, the coefficients obey the following equality:

$$A + B + C = 1 \tag{4.13}$$

The active (P_{IM}) and reactive powers (Q_{IM}) are calculated as follows:

$$P_{IM} = v_d i_{ds} + v_q i_{qs} \tag{4.14}$$

$$Q_{IM} = v_q i_{ds} - v_d i_{qs} \tag{4.15}$$

The static part of the model can be described using the exponential load model introduced in Chapter 2. As it has been shown, the exponential model can give very similar results to the polynomial load model and it only has two parameters in total to be estimated. The total power output of the CLM is described as follows:

$$P_{CLM} = S_b P_{IM} + P_S \tag{4.16}$$

$$Q_{CLM} = S_b Q_{IM} + Q_S \tag{4.17}$$

where S_b is the induction machine power base in VA and P_s and Q_s are the active and reactive power consumed by the static part of the load in W and var, respectively.

Additionally, following [21], the parameter K_P defines the initial consumption of active power by the IM relative to the total initial active power:

$$K_P = \frac{P_{M0}}{P_0} \tag{4.18}$$

where P_{M0} is the initial active power consumed by the IM, in W, and P_0 is the pre-disturbance active power measured at the load bus in W.

To obtain an output from the model presented above (4.16)-(4.17), the following vector with 12 unknown parameters needs to be determined:

$$\boldsymbol{\theta}_{CL} = [H, R_s, X_s, R_r, X_r, X_m, A, B, K_P, T_0, \alpha, \beta] \tag{4.19}$$

Parameters C, S_b, P_{S0} and Q_{S0} are not included in (4.19) because they can be analytically determined as follows:

$$P_{M0} = K_P P_0 \tag{4.20}$$

$$S_b = \frac{P_{M0}}{P_{M0pu}} \tag{4.21}$$

where P_{M0pu} is the per unit pre-disturbance active power consumed by the IM and is obtained from its steady-state equivalent circuit (Figure 4-2) based on the parameters already included in (4.19) and the pre-disturbance voltage V_0.

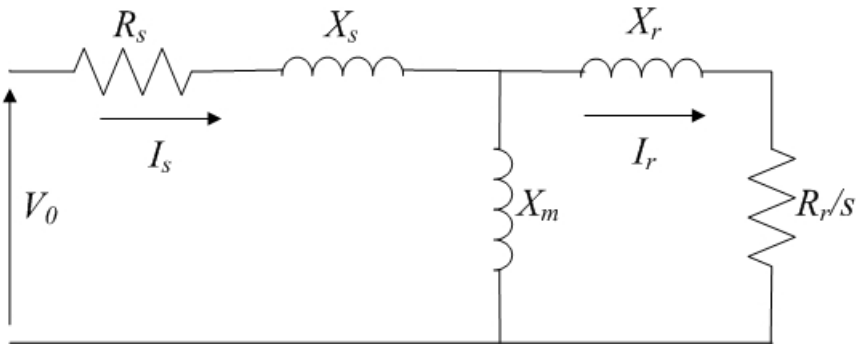

Figure 4-2: Equivalent circuit of an induction motor in the steady-state

The per unit pre-disturbance reactive power Q_{M0pu} can be calculated from the same equivalent circuit. Then the pre-disturbance reactive power consumed by the induction motor will be given by:

$$Q_{M0} = S_b Q_{M0pu} \tag{4.22}$$

It is then straightforward to obtain the pre-disturbance active and reactive power consumed by the static load:

$$\begin{aligned} P_{S0} &= P_0 - P_{M0} \\ Q_{S0} &= Q_0 - Q_{M0} \end{aligned} \tag{4.23}$$

where P_0 and Q_0 are the measured pre-disturbance active and reactive power, respectively, in W and var. Finally, parameter C can be calculated based on (4.13):

$$C = 1 - A - B \tag{4.24}$$

Now, the model output can be calculated for a given measured voltage, which means that (4.19) contains information sufficient to fully describe the presented composite

load model. A typical response of the model to a voltage step change is depicted in Figure 4-3.

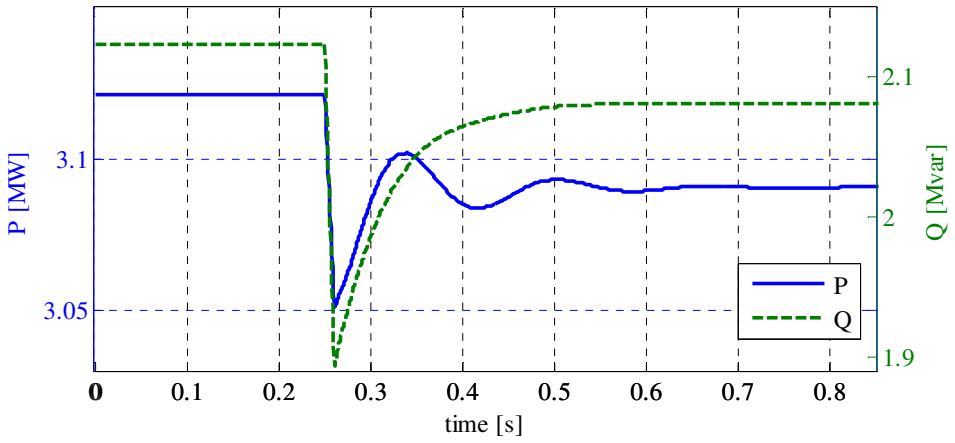

Figure 4-3: Typical *P* and *Q* responses of the composite load model to a negative voltage step change

4.2.3. Trajectory Sensitivity Analysis of the IM Model

The CL model contains a considerable degree of complexity. From the point of view of parameter estimation it is important to reasonably assess such a model and investigate the identifiability of its parameters. One way of achieving this is offered by sensitivity analysis, or more specifically by trajectory sensitivity analysis. This technique was introduced to power systems in [94] and [95] to evaluate network models that include discrete dynamics and switching events. Trajectory sensitivity is given as a derivative of the model's state evolving in time (trajectory) with respect to the initial conditions and/or parameters. This approach has an advantage over steady-state sensitivity analysis because it offers an insight into the model's behaviour during a dynamic transition. In [25] this technique has been applied to the IM model to reduce the number of parameters to be identified by evaluating the trajectory sensitivities of the active and reactive powers consumed by the motor with respect to the model's parameters. Then parameters with higher sensitivity would be considered more important during the parameter estimation process. The same approach was adopted in this project to investigate the identifiability of the IM model's parameters.

The general form of the IM model can be expressed as:

$$\dot{x} = f(x, y, p) \tag{4.25}$$

$$0 = g(x, y, p) \tag{4.26}$$

where x is the vector of dynamic states, y is the vector of algebraic states and p is the vector of model parameters. A detailed description of this model can be found in Appendix D. Then, following [25], the trajectory sensitivities with respect to the model's parameters can be obtained by solving the following system:

$$\frac{d}{dt}\left(\frac{\partial x}{\partial p}\right) = \frac{\partial f}{\partial x}\frac{dx}{dp} + \frac{\partial f}{\partial y}\frac{\partial y}{\partial p} + \frac{\partial f}{\partial p} \tag{4.27}$$

$$0 = \frac{\partial g}{\partial x}\frac{\partial x}{\partial p} + \frac{\partial g}{\partial y}\frac{\partial y}{\partial p} + \frac{\partial g}{\partial p} \tag{4.28}$$

where the elements $\frac{\partial x}{\partial p}$ and $\frac{\partial y}{\partial p}$ are the trajectory sensitivities with respect to the parameters. All of the remaining elements can be calculated in advance and they are given in Appendix D. The initial conditions for both $\frac{\partial x}{\partial p}$ and $\frac{\partial y}{\partial p}$ can be obtained from the steady-state equations:

$$0 = \frac{\partial f}{\partial x}\frac{dx}{dp} + \frac{\partial f}{\partial y}\frac{\partial y}{\partial p} + \frac{\partial f}{\partial p} \tag{4.29}$$

$$0 = \frac{\partial g}{\partial x}\frac{\partial x}{\partial p} + \frac{\partial g}{\partial y}\frac{\partial y}{\partial p} + \frac{\partial g}{\partial p} \tag{4.30}$$

Because the estimation procedure of the unknown model parameters is carried out based on the active and reactive powers measurements, trajectory sensitivities of these states will be of interest.

4.3. Estimation Methods

All iterative methods perform optimization tasks that are formulated as a curve fitting problem where the following objective function is to be minimized (4.25):

$$\varepsilon(\boldsymbol{\theta}) = \frac{1}{n}\sum_{i=1}^{n}\left[\left(f_i(\boldsymbol{\theta})\right)^2\right] \tag{4.25}$$

$$f_i(\boldsymbol{\theta}) = y_i - M(\boldsymbol{\theta}, u_i) \tag{4.26}$$

where $M(\boldsymbol{\theta},u_i)$ is the output of the assumed model for the i-th step, $\boldsymbol{\theta} \in \Re^m$ is the vector of unknown parameters governing the assumed model, u_i is the control input for the i-th step, y_i is the measurement for the i-th step and n is the number of samples belonging to the selected data set.

Techniques belonging to this group iterate over the whole set of data, applying a small correction $\Delta\boldsymbol{\theta}$ to the vector $\boldsymbol{\theta}$ at each step, until a termination condition is reached. This usually occurs when satisfactory accuracy is achieved or the algorithm reaches the maximum number of iterations. This gives a very general framework in which iterative methods operate. The main difference between specific methods lies in the way of obtaining the corrective vector $\Delta\boldsymbol{\theta}$.

4.3.1. Nonlinear Least Squares

Nonlinear Least Squares (NLS) is a group of methods that minimize (4.25) by using a first order linearization of the model. The simplest version of this technique, the Gauss-Newton method, is formulated as follows [84]:

$$(\mathbf{J}(\boldsymbol{\theta})^T \mathbf{J}(\boldsymbol{\theta}))\mathbf{h}_{gn} = -\mathbf{J}(\boldsymbol{\theta})^T \mathbf{f}(\boldsymbol{\theta}) \tag{4.27}$$

$$\boldsymbol{\theta}_{k+1} = \boldsymbol{\theta}_k + \mathbf{h}_{gn} \tag{4.28}$$

$$(\mathbf{J}(\boldsymbol{\theta}))_{ij} = \frac{\partial f_i}{\partial \theta_j}(\boldsymbol{\theta}) \qquad i = 1,\ldots,n \qquad i = 1,\ldots,m \tag{4.29}$$

where $\mathbf{J}$ is the Jacobi matrix of function $\mathbf{f}(\boldsymbol{\theta})$ (4.26) and $\mathbf{h}_{gn}$ is the Gauss-Newton corrective step. After solving (4.27), the h_{gn} gives just one step towards the solution and the operation has to be repeated (including the calculation of Jacobi matrix) until satisfactory accuracy is achieved or the maximum number of iteration is reached. The

solution is updated at each iteration according to (4.28) and the whole process is illustrated in Figure 4-4.

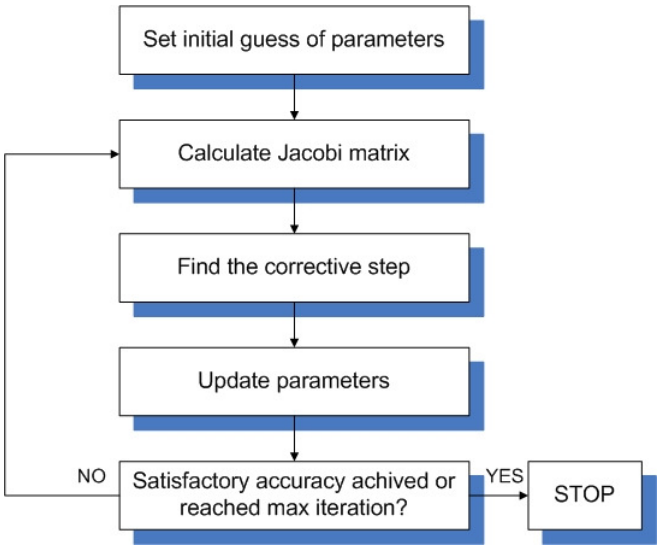

Figure 4-4: Flowchart of Gauss-Newton method

The classical Gauss-Newton algorithm is suitable for solving simple nonlinear problems, but when it comes to more complex models this method may often diverge. To prevent this, Levenberg in 1944 and later Marquardt in 1963 suggested using a damped Gauss-Newton method [84]. The Levenberg-Marquardt method introduces the damping parameter μ into (4.27):

$$(\mathbf{J}(\boldsymbol{\theta})^T \mathbf{J}(\boldsymbol{\theta}) + \mu \mathbf{I})\mathbf{h}_{lm} = -\mathbf{J}(\boldsymbol{\theta})^T \mathbf{f}(\boldsymbol{\theta}) \tag{4.30}$$

where $\mathbf{I}$ is the identity matrix ($m \times m$) and $\mathbf{h}_{lm}$ is the Levenberg-Marquardt corrective step.

Introduction of the damping factor has several effects [84]:

- for all $\mu > 0$ the coefficient matrix is positive definite, this ensures that $\mathbf{h}_{lm}$ is a descent direction,
- for large values of μ a short step in the steepest descent direction is applied, which is good when the current iteration is far from the solution,
- for small values of μ the algorithm becomes very close to the Gauss-Newton method, which is good when the current iterate is close to the solution.

Selection of the damping parameter is proposed as follows:

$$\mu = \tau \max\{(\mathbf{J}(\boldsymbol{\theta})^T \mathbf{J}(\boldsymbol{\theta}))_{ii}\} \tag{4.31}$$

where $(\mathbf{J}(\boldsymbol{\theta})^T \mathbf{J}(\boldsymbol{\theta}))_{ii}$ are the diagonal elements of $\mathbf{J}(\boldsymbol{\theta})^T \mathbf{J}(\boldsymbol{\theta})$ matrix and τ is an additional parameter selected by the user.

NLS methods are computationally efficient and accurate. However, this type of techniques requires a matrix inversion at each step, which, in some cases, can lead to divergence and unpredictable behaviour. Additionally, the algorithm is a local minimizer, which means that the final solution depends on the initial guess and it may not reach the global minimum, especially when the model is a complex nonlinear function.

4.3.2. Artificial Intelligence Methods

Artificial Intelligence is a vast branch of computer science that targets the creation of intelligent machines. Within this group there exists a subcategory, called evolutionary computation, which seeks to deal with difficult optimization problems by imitating biological mechanisms of evolution and other processes inspired by nature. As mentioned before, Genetic Algorithms are the AI technique most commonly used for the estimation of load model parameters. However, it has been found that other AI methods can also give very good results, sometimes showing higher efficiency than GA. Improved Particle Swarm Optimization has been proven through experimentation to be more reliable and accurate than traditional GA, especially in the case of more complex models.

The most important characteristic of all AI techniques is that, when properly tuned, they are capable of finding a global minimum of a highly nonlinear problem. This feature is a major advantage over the NLS methods and it also is the reason why AI techniques have become so popular. These algorithms do not rely on a single initial guess, but rather they use a set (*population*, *swarm*) of candidate solutions (*individuals*, *genomes*, *particles*) that provide a much broader penetration of the searching space. The whole set is iterated towards a better solution through so called

generations. Each generation is modified using a set of operators specific to the particular method and each individual is ranked. To assess the quality of each individual, a *fitness function* (4.32) is used, which is simply a reciprocal of the objective function (4.25). The process is terminated in a similar fashion to NLS techniques – when the satisfactory accuracy is obtained or the maximum number of generations is reached.

$$fitness = \frac{1}{\varepsilon(\boldsymbol{\theta})} \tag{4.32}$$

The biggest disadvantage of AI techniques is the CPU demand, which is much higher than that of NLS methods. The reason for this is the high number of model assessments performed during the process. For example, a population of 100 individuals passed through 100 generations will require 10000 calls to the fitness function. This time-consuming procedure usually makes it impossible to use these methods in real-time applications. However, in offline applications, where no decisive information is expected from the algorithm, these techniques are very well suited.

The character of AI algorithms is such that randomness plays an important role in it. For a given initial population the path of obtaining the final result (and possibly the result itself) may be different for every execution of the algorithm. For this reason it is important to perform statistical tests of reliability for a given method, because a single run can be very deceptive and thus cannot prove the true effectiveness of the method.

4.3.2.1. Genetic Algorithms

This technique is based on evolution theory and imitates the phenomenon of natural selection [85], [86]. A flowchart illustrating GA is presented in Figure 4-5. Following the natural processes, GA consists of three stages – forming of the population, selection and then reproduction. Each element is described in detail below.

Forming of the population. This is an initial stage which only takes place once during the procedure. The algorithm starts by producing an initial population with a defined size *N*. The population is filled with *N* genomes, each being an equivalent of

parameter vector **θ** defined in (4.25), containing randomly generated elements (called *genes*). Each gene is constrained according to the knowledge of the assumed model and the observed system. The role of this initial process is a uniform exploration of the searching space (*m*-dimensional) and the parameter *N* is found through empirical studies. However, it is obvious that this parameter will mostly depend on the complexity of the model (dimension of the searching space) and the range of each gene (size of the searching space).

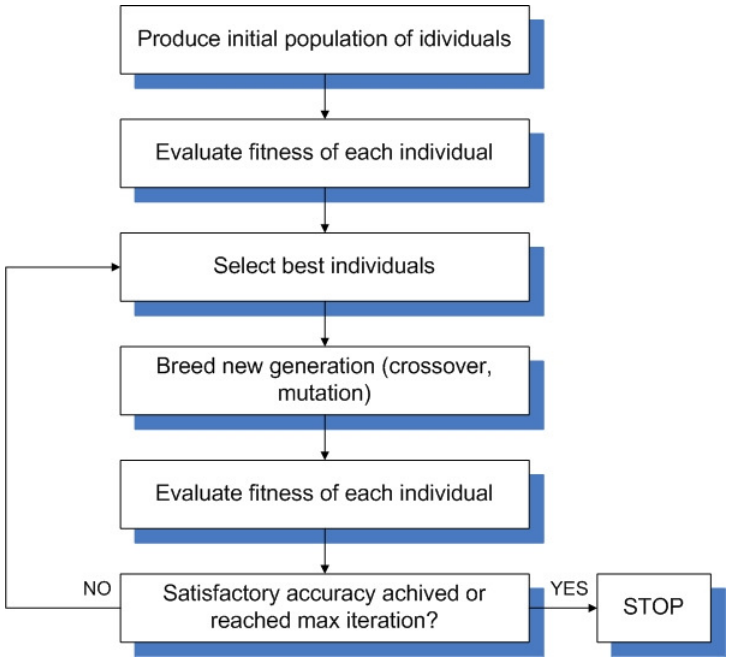

Figure 4-5: Flowchart of GA

Selection. This process takes place in each generation (iteration) of the algorithm. Firstly, the fitness of each genome is evaluated using the fitness function and the genomes are sorted, starting with those with the highest fitness. In the second stage of this process couples of genomes are selected for reproduction according to their fitness. Roulette wheel selection, a method commonly used in GA, selects genomes with a probability proportional to their rank in the population. This technique allows the new generation to be mostly built based on the best individuals, but also introduces some portion of weaker genomes (genomes with lower fitness) to preserve the variety of the population, so that the algorithm will not converge prematurely.

Reproduction. During this stage a new generation is formed using the previously selected genomes. Traditionally, several different genetic operators are incorporated to produce the next generation:

Crossover – this method produces children (new genomes) by combining parents (therefore this process is also called recombination). Figure 4-6 illustrates this strategy.

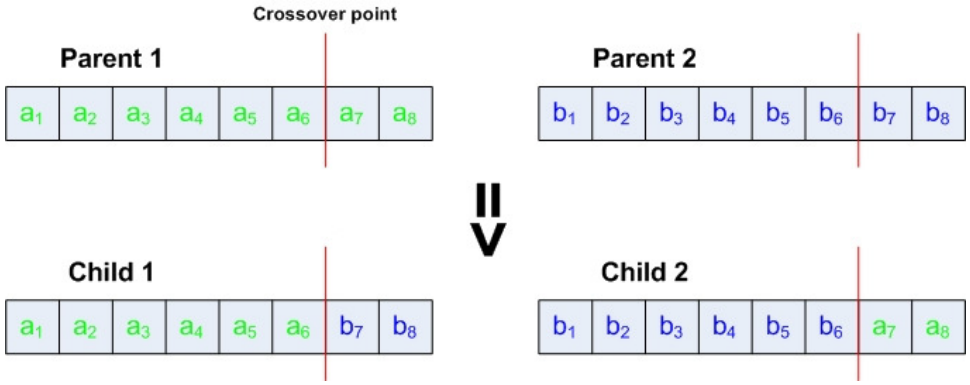

Figure 4-6: Reproduction by crossover: Parent 1, Parent 2 – selected genomes; Child 1, Child 2 – new genomes

Crossover is performed by splitting both selected genomes (parents) at a *crossover point* (a predefined parameter), which is equal to 0.75 in the example depicted in Figure 4-6. In the next step, the first part (from the beginning of the genome up to the crossover point) of the first parent is joined with the second part (from the crossover point until the end of the genome) of the second parent and vice versa. Additionally, a parameter called *crossover rate* defines the probability with which the crossover occurs. Its value is most often set below 1, which allows some of the selected couples of genomes to be transferred to the new generation unchanged.

Mutation – this genetic operator is used to accompany crossover and further increase the diversity of a population by changing randomly selected genes. In a simple binary representation, where a gene can only take a value of 0 or 1, the mutation operator randomly selects a gene and changes its value to the opposite, as depicted in the example in Figure 4-7.

Figure 4-7: Mutation in binary representation

However, using this type of representation to encode parameters of an assumed load model is at the very least inconvenient. For this reason a real number representation should be implemented. This change only requires a different definition of the mutation operator. In this work, the following formula has been used to apply mutation to a selected gene:

$$\theta_{New} = \theta_{Old} + 2(rand - 0.5)\frac{r}{100}\theta_{Old} \tag{4.33}$$

where θ_{Old} is the gene undergoing a mutation, θ_{New} is the new gene, *rand* is a uniformly distributed random number between 0 and 1 and r is the coefficient defining the magnitude of the potential change in %. It has been found that an optimal value for r is equal to 5, which means that every time a mutation occurs it will add a uniformly distributed random number from a range of ±5% of the actual value of the gene. An additional benefit gained from applying mutations is that it increases the fine-tuning capability of the algorithm. In the final stage of the procedure, when all of the genomes are very similar, the mutation operator creates diversity around the final solution and increases its accuracy.

Elitism – this simple operation is applied to prevent a regression of the algorithm. To achieve this, a pair of the best individuals from a population is always transferred to the next generation unchanged. This also ensures that those best genomes will not be lost during reproduction by combining with some weak individuals.

4.3.2.2. Improved Particle Swarm Optimization

Originally, Particle Swarm Optimization (PSO) was proposed by Kennedy and Eberhart [87]-[89] in 1995. This technique was inspired by bird flocks' social

behaviour [90] and it is similar to GA in that it also operates on a group of individuals that carry candidate solutions for a given problem. In fact the initialization and termination of the both algorithms are identical. The difference lies in the way the method progresses towards a better solution. A flowchart depicting the procedure is given in Figure 4-8.

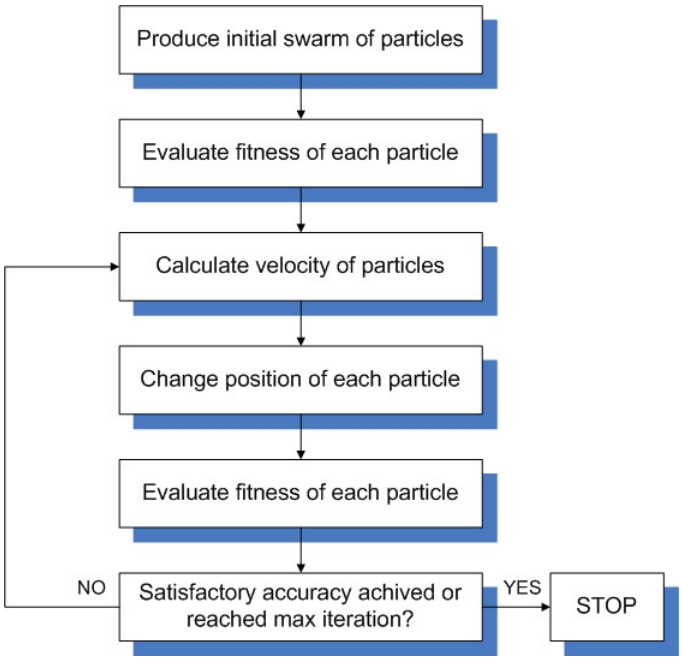

Figure 4-8: Flowchart of PSO

The whole process can be divided into three stages – forming initial swarm, calculating velocities, changing positions. Each stage is described below.

Forming initial swarm. As mentioned earlier, this stage of the algorithm is identical to that of GA. The terminology is slightly different, a population of individuals is called a swarm and each individual is called a particle. However the meaning is exactly the same.

Calculating velocities. This procedure is applied at each iteration of the algorithm. In PSO the particles are not combined to breed a new generation, instead they move around the searching space according to the formula shown below:

$$\mathbf{V}_i^{k+1} = \Phi \mathbf{V}_i^k + c_1 r_1 (\mathbf{P}_i^k - \boldsymbol{\theta}_i^k) + c_2 r_2 (\mathbf{P}_g^k - \boldsymbol{\theta}_i^k) \tag{4.34}$$

where $\mathbf{V}_i^k$ and $\mathbf{V}_i^{k+1}$ are the actual and next step velocity of the *i*th particle, Φ is the inertia weight, $\mathbf{P}_i^k$ is the best previous position of the *i*th particle, $\mathbf{P}_g^k$ is the best global position, $\boldsymbol{\theta}_i^k$ is the actual position of the *i*th particle, c_1 and c_2 are the acceleration coefficients, usually equal to 2, and r_1 and r_2 are uniformly distributed random numbers between 0 to 1. All particles are ranked according to the fitness function (4.32).

Changing positions. This procedure simply applies the previously calculated velocities to the corresponding particles according to the formula:

$$\boldsymbol{\theta}_i^{k+1} = \boldsymbol{\theta}_i^k + \mathbf{V}_i^{k+1} \tag{4.35}$$

The process of moving the particles around the searching space is repeated until it reaches a termination condition, which is the same as in GA.

To increase the reliability and accuracy of PSO researchers started looking for new strategies, which could be combined with the original algorithm. In this way a number of different versions of Improved Particle Swarm Optimization emerged in [80]-[82]. The most common strategy is related to the inertia weight Φ. Traditionally this parameter was fixed and in [81] a nonlinear function modulating Φ was proposed:

$$\Phi_k = \left\{ \frac{(k_{\max} - k)^n}{(k_{\max})^n} \right\} (\Phi_{initial} - \Phi_{final}) + \Phi_{final} \tag{4.36}$$

where $\Phi_{initial}$ is the initial inertia weight, Φ_{final} is the final inertia weight, $k_{\max}$ is the maximum number of iterations, k is the number of current iteration and n is the nonlinear modulation index. This operation improves the convergence properties of the algorithm and also increases its accuracy.

In [80] the inertia weight has been further improved by introducing chaotic behaviour. As proven in [91], chaotic sequences can improve the results obtained by evolutionary algorithms. A simple dynamic system called *logistic map* was used to improve the

traditional PSO algorithm. The system demonstrates chaotic behavior and is described by the following formula:

$$\gamma_k = \mu\gamma_{k-1}(1-\gamma_{k-1}) \tag{4.37}$$

where μ is a control parameter and γ_k is the chaotic parameter for the *k*th iteration. The system displays chaotic behavior for $\mu = 4.0$ and $\gamma_0 \notin \{0.0, 0.25, 0.50, 0.75, 1.00\}$. The chaotic parameter γ_k is then combined with the inertia weight Φ_k calculated from (4.36) in the following way:

$$\Phi_{Ck} = \gamma_k \Phi_k \tag{4.38}$$

where Φ_{Ck} is the new inertia weight that now includes chaotic behaviour for the *k*th iteration. Such an operation introduces chaotic behaviour into the inertia weight parameter and thus improves the searching capabilities of the traditional PSO. A visual comparison of the different strategies related to the inertia weight is depicted in Figure 4-9.

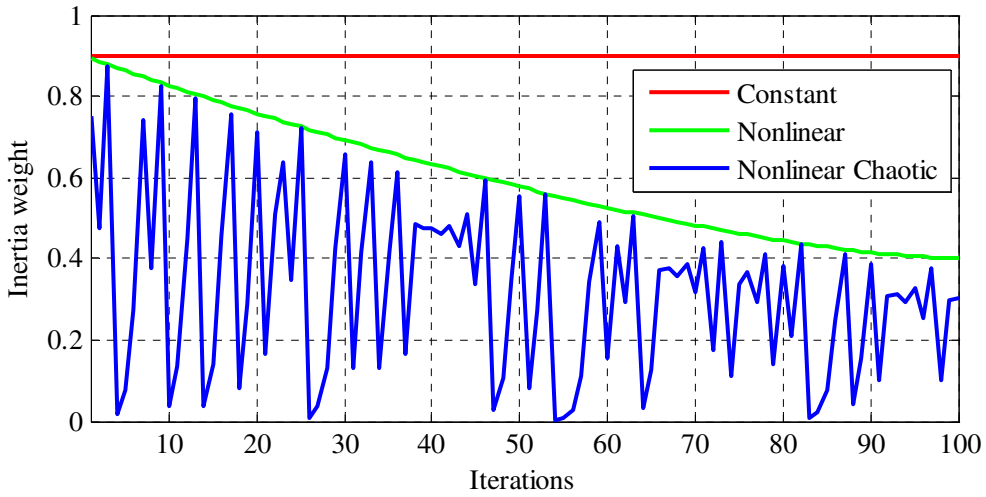

Figure 4-9: Examples of different types of inertia weight modulation

The last, but probably most crucial strategy, introduced to improve the traditional PSO is the crossover operation adopted for Genetic Algorithms. This technique allows a further increase in the speed of information exchange between the individuals in a population. Assuming that the particle undergoing a crossover operation and the

actual best global particle are expressed as:

$$\boldsymbol{\theta}_i = \left[\theta_{i1} \quad \theta_{i2} \quad \ldots \quad \theta_{in}\right] \tag{4.39}$$

$$\mathbf{P}_g = \left[P_{g1} \quad P_{g2} \quad \ldots \quad P_{gn}\right] \tag{4.40}$$

the crossover operation can be formulated as follows [80]:

$$\theta_{ij} = \begin{cases} \theta_{ij}, & \text{if } r_{ij} \le CR \\ P_{gj}, & \text{otherwise} \end{cases} \tag{4.41}$$

where *CR* is the Crossover Rate parameter that has a value between 0 and 1, r_{ij} is a uniformly distributed random number between 0 and 1, *i* is the number of a particle, $j=1\ldots n$ and *n* is the dimension of the searching space. In this way, whenever the random number r_{ij} is greater than the defined *CR* parameter, the selected information from the best global particle will be copied to the particle undergoing a crossover operation.

4.4. Results

4.4.1. Exponential Recovery Load Model

4.4.1.1. Measurement Data

To perform the estimation of load model parameters, *RMS* measurements of *V*, *P* and *Q* are necessary. In the first stage some data has been obtained through computer simulations performed in the DIgSILENT software [61]. The required signals are directly available through stability analysis simulation and can be easily exported outside the program in the form of a comtrade file or plain text file. Here, a simple 2-bus configuration has been used, where a programmable voltage source is feeding a dynamic load through a line (Figure 4-10). The sampling frequency in this case is equal to 1 Hz.

Figure 4-10: Single-line diagram of the two-bus system

In the remaining cases, recordings taken at two substations (35kV and 10kV levels) have been used [29]. The measurement configuration is depicted in Figure 4-11. To expose the characteristics and dynamics of loads a voltage change is required. Probably the easiest and most efficient way to achieve this is through a manual transformer tap change. Each single tap provides a voltage step change of 1.5% and each measurement taken used 2 to 5 tap changes to provide deeper steps. The time constants of the load responses usually exceeded one minute (up to several minutes) so the sampling period of 1s was sufficient for the purpose of this project. A number of cases have been captured with one example depicted in Figure 4-12.

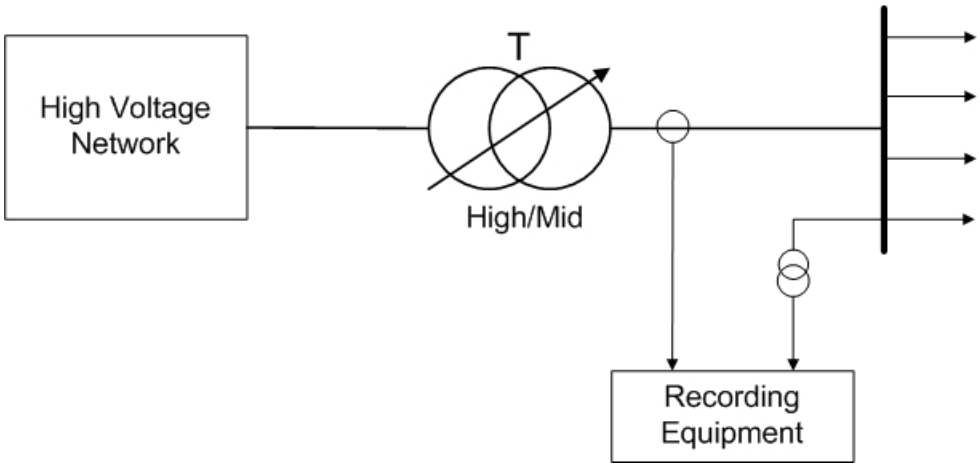

Figure 4-11: Single-line diagram of the measurement configuration

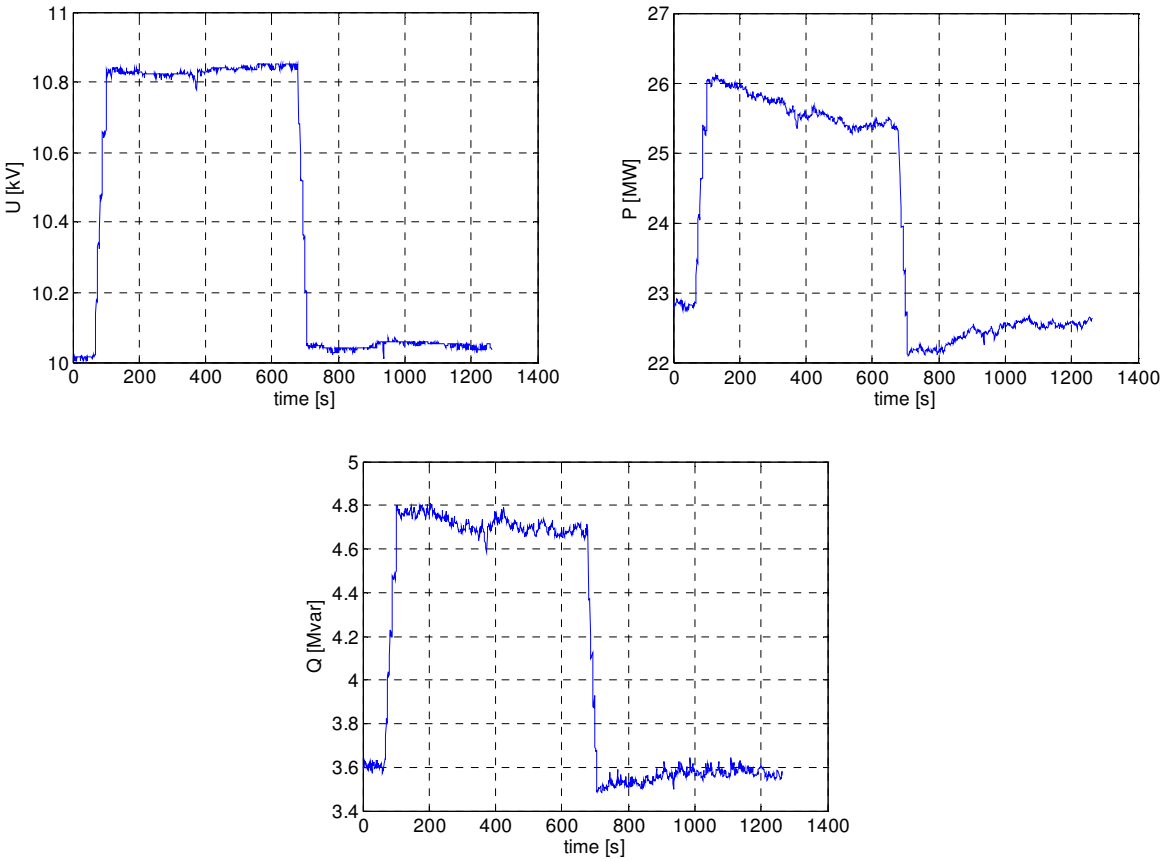

Figure 4-12: Measurements of *RMS* voltage, active and reactive power

4.4.1.2. Estimation Results

The numerical analysis presented here is based on comparison studies of different performance factors for the three aforementioned estimation methods. To achieve this, some appropriate conditions need to be established. First of all, a reference population of 100 individuals has been generated and used for all of the methods to ensure that the results are comparable. Secondly, the ranges of the parameters used to generate the initial population have been selected to cover all possible scenarios. The expected model parameters for the active and reactive powers have been set to the same values: the static and dynamic exponents are between 0 and 5 and the time constant is between 1s and 4000s. This selection covers a very wide range of load characteristics and should provide a good starting point for all of methods.

For the purpose of a statistical analysis of their reliability, both of the AI methods have been executed for 100 trials using the same reference population in every trial.

This operation allows the true effectiveness of both techniques to be exposed. To achieve a similar result with the NLS method, 100 trials have been executed using a different candidate from the reference population as an initial guess in each trial. Although the two approaches described above are different, they both provide a measure of reliability.

Preliminary results have been obtained through computer simulations using the 2-bus system (Figure 4-10). A summary of 4 simulations is given in Table 4-1, including reliability analysis and values of the estimated parameters in the best trial for each method. It should be noted that in all four cases IPSO and NLS achieved very high accuracy in every trial, which is also reflected in the very small standard deviation of the model error. The results obtained by GA are acceptable; however, the final accuracy could be improved. The size of the searching space would probably require a larger initial population to ensure the necessary diversity. Furthermore, it can be observed that when using idealized measurements the optimization process seems rather simple, with one strongly pronounced minimum. Otherwise, the reliability of NLS would probably be lower, with some of the initial guesses converging to local minima. The model error is defined by the objective function (4.25).

Table 4-1: Results of estimation based on computer simulations (ERL model)

	Model error (P)				Model Parameters (best trial)		
	min	avg	max	std. dev.	α_t	α_s	T_P
Simulation 1					**3**	**1**	**10**
IPSO	5.27E-26	2.76E-20	2.42E-18	2.42E-19	3.0000	1.0000	10.0000
GA	9.41E-11	1.32E-04	3.27E-04	7.18E-05	2.9989	0.9998	10.0115
NLS	5.23E-32	1.57E-23	6.60E-22	7.23E-23	3.0000	1.0000	10.0000
Simulation 2					**4**	**0**	**100**
IPSO	1.51E-20	2.25E-15	4.42E-14	5.96E-15	4.0000	1.40E-08	100.0000
GA	9.65E-07	6.78E-06	2.45E-05	6.58E-06	4.0486	0.0567	94.9118
NLS	1.98E-31	4.40E-21	6.32E-20	1.11E-20	4.0000	-1.09E-13	100.0000
Simulation 3					**3**	**2**	**500**
IPSO	6.01E-30	1.33E-24	3.43E-23	4.64E-24	3.0000	2.0000	500.0000
GA	5.43E-12	1.15E-07	6.16E-06	6.66E-07	3.0000	1.9999	500.0111
NLS	1.42E-30	6.22E-22	1.63E-20	2.85E-21	3.0000	2.0000	500.0000
Simulation 4					**2**	**1**	**1000**
IPSO	1.68E-27	1.88E-21	1.11E-19	1.20E-20	2.0000	1.0000	1000.0000
GA	4.88E-12	1.83E-10	1.21E-09	1.99E-10	2.0002	1.0002	999.3482
NLS	3.04E-30	4.59E-24	2.86E-22	2.97E-23	2.0000	1.0000	1000.0000

The remaining examples are based on the aforementioned real-data measurements obtained at a substation. These recordings are of course much more interesting from the point of view of estimation, because they include potential noise and spontaneous load changes. The first set of results is depicted in Figure 4-13 and Figure 4-14 and in Table 4-2.

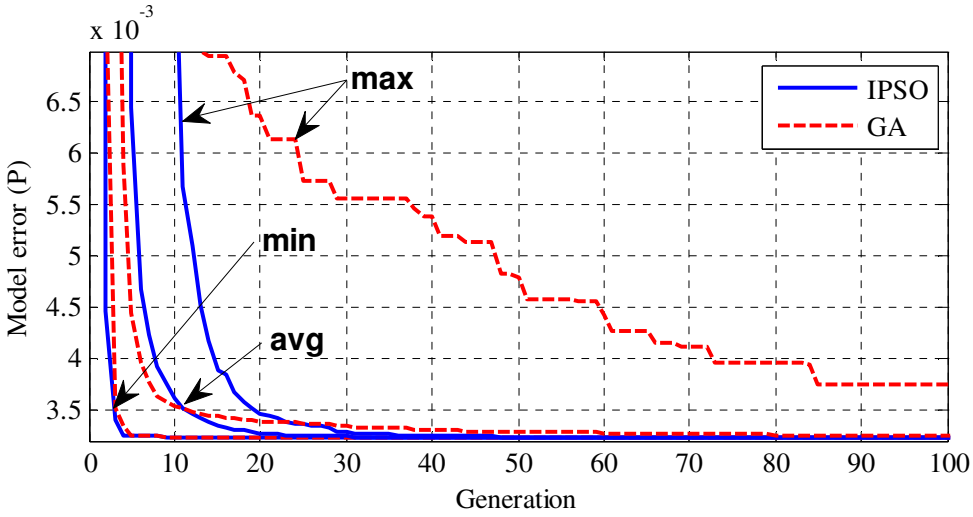

Figure 4-13: Convergence curves (*P*) for AI methods: min, average and max values: Case 1

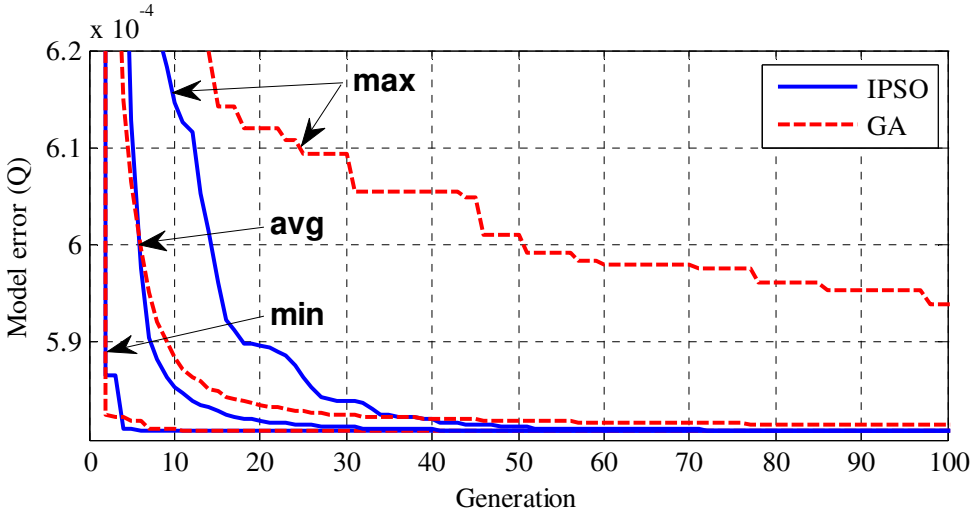

Figure 4-14: Convergence curves (*Q*) for AI methods: min, average and max values: Case 1

Table 4-2: Statistical analysis of the results obtained for case 1

Case 1	Model error (P)				Model error (Q)			
	min	avg	max	std. dev.	min	avg	max	std. dev.
IPSO	0.0032331	0.0032331	0.0032331	4.09E-11	0.0005809	0.0005809	0.0005809	3.04E-09
GA	0.0032331	0.0032477	0.0037132	6.86E-05	0.0005809	0.0005814	0.0005938	1.86E-06
NLS	0.0032331	0.0032384	0.0037696	5.37E-05	0.0005809	0.0005812	0.0005850	6.94E-07

Figure 4-13 and Figure 4-14 present the minimum, average and maximum model error for each generation, which is an effective depiction of the progression of both AI techniques over time for all of the 100 trials. Table 4-2 on the other hand summarizes the final results for all three methods. It is clear that in this case IPSO demonstrated the best performance in terms of reliability and accuracy. However, it should be noted that the differences are very small and are in fact negligible for the purpose of load modelling applications. This can be observed in Figure 4-15, where the curve-fitting results for all of the methods are presented and are virtually overlapping one another. The NLS method reached a very poor solution in one case, which has not been taken into account in Table 4-2. However, it should be considered as a first sign of the sensitivity of this method to the initial guess.

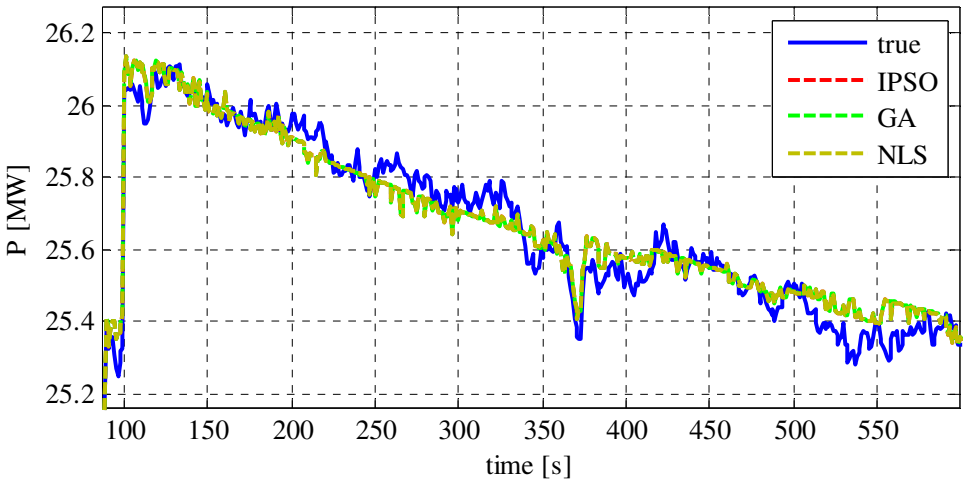

Figure 4-15: Estimation result for active power: Case 1

Similarly, in the second case the same population of individuals has been used and the convergence curves for the AI methods are presented in Figure 4-16 and Figure 4-17. Table 4-3 contains the results for all three techniques and this time the results are much more interesting. First of all, the problem of premature convergence of GA is clearly visible in estimations of both, active and reactive power. It should be noted that although IPSO slows down in the similar region, usually after several generations it then accelerates towards a better solution.

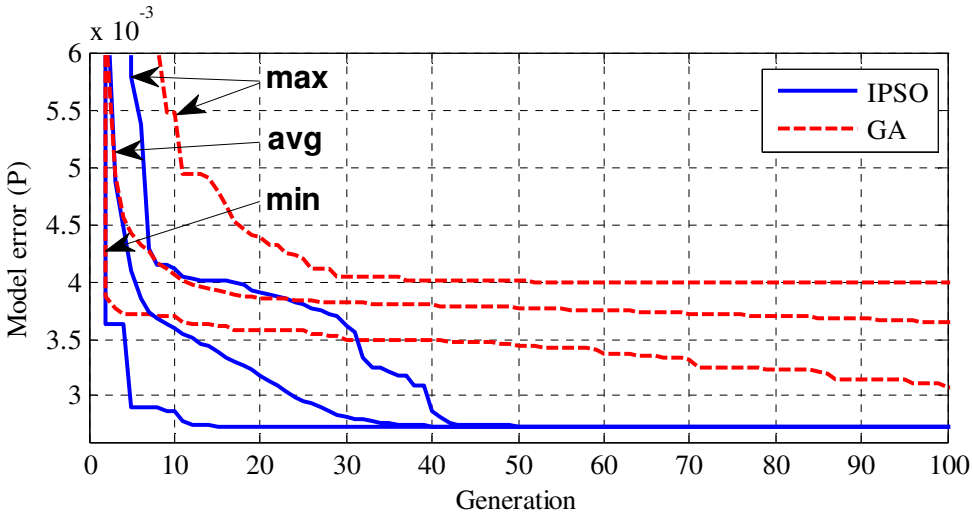

Figure 4-16: Convergence curves (*P*) for AI methods: min, average and max values: Case 2

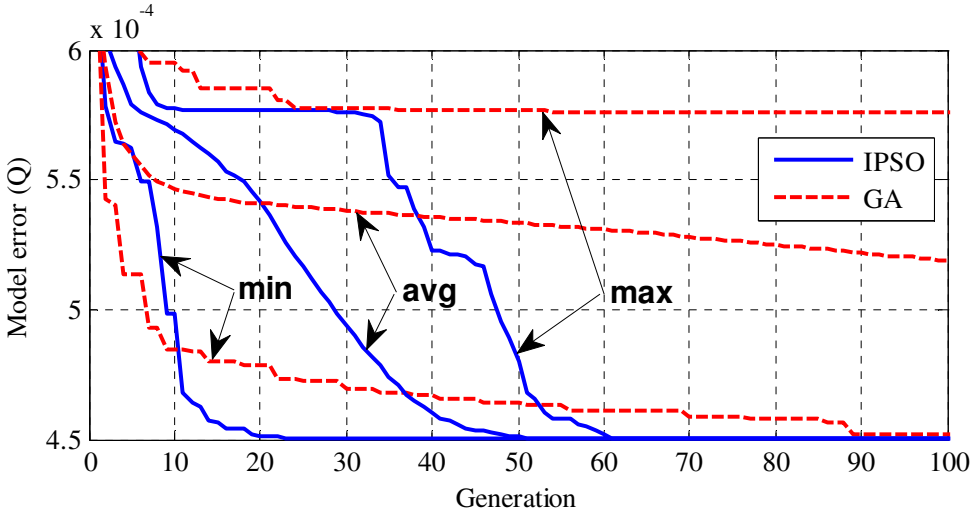

Figure 4-17: Convergence curves (*Q*) for AI methods: min, average and max values: Case 2

Table 4-3: Statistical analysis of the results obtained for case 2

Case 2	Model error (P)				Model error (Q)			
	min	avg	max	std. dev.	min	avg	max	std. dev.
IPSO	0.0027306	0.0027306	0.0027306	2.73E-14	0.0004501	0.0004501	0.0004501	5.88E-17
GA	0.0030829	0.0036448	0.0039961	2.87E-04	0.0004518	0.0005185	0.0005758	2.32E-05
NLS	0.0027306	0.0029120	0.0208677	1.81E-03	0.0004501	0.0005175	0.0005768	6.26E-05

A similar phenomenon occurs in case of the NLS. However, this methods dependence on the initial guess causes it to jump between solutions. For this reason it has the highest standard deviation in Table 4-3. Additionally, Figure 4-18 visualizes the behaviour of all three methods by presenting the final solutions for each trial for reactive power estimation. From the figure it is clear that there must be at least two

strong minima attracting the methods and the poorer convergence properties of GA cause it to produce results somewhere in between them.

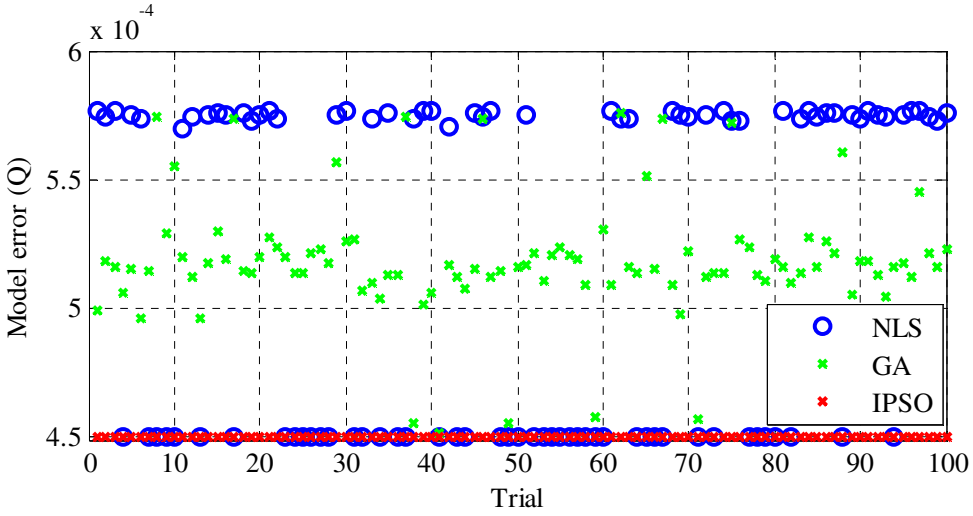

Figure 4-18: Model error of the final solutions: Case 2

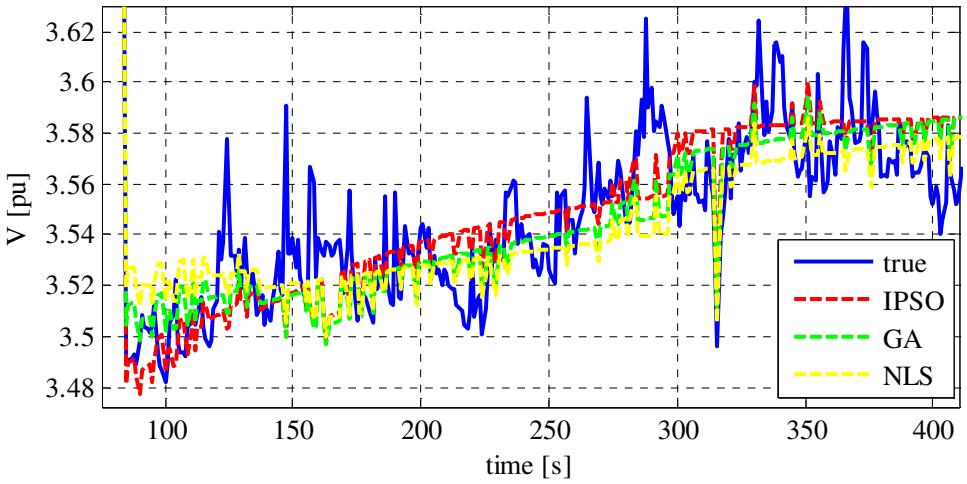

Figure 4-19: Estimation result for reactive power: Case 2

The difference between the two mentioned optima is shown in Figure 4-19. IPSO is able to capture precisely the recovery dynamics at the beginning of the curve, whereas the other two methods, in some trials, are missing this area and have concentrated on the rest of the shape. This is important, despite how small the difference may seem to be, as it has a dramatic impact on the values of the estimated parameters (Table 4-4). The first optimum is a quickly recovering example with a quite favourable static characteristic, whereas the second one is a slowly recovering example with a considerable difference between the transient and static demands. Obviously, the methods can extract only as much information as is observable from the captured data and in this case these very different solutions produce quite similar model errors.

Nonetheless, the task is to minimize the objective function with given measurements and so far IPSO is showing the best efficiency in this regard.

Table 4-4: Values of estimated model parameters (Q): Case 2

Optimum	β_t	β_s	T_Q
I (IPSO)	3.94	3.53	75.06
II (NLS)	3.75	1.60	3351.18

The remaining cases give very similar results to the previous two and the summary is presented in Table 4-5 to Table 4-10. The analysis simply confirms the typical behaviour of the estimation methods explained using the first two cases. IPSO is very accurate and reliable compared to the other two techniques. The NLS method, as expected, converges to the nearest local minimum, which in some cases is very poor. Finally, GA may suffer from premature convergence. From Figure 4-16 and Figure 4-17 it can be seen that the average convergence curves of GA are slowly decreasing, which means that better results could be achieved if the number of generations were increased. However, this would be very costly in terms of CPU demand. Another remedy, with very similar cost, would be to increase the population size.

Table 4-5: Statistical analysis of the results obtained for case 3

Case 3	Model error (P)				Model error (Q)			
	min	avg	max	std. dev.	min	avg	max	std. dev.
IPSO	0.0077474	0.0077474	0.0077474	1.12E-15	0.0025700	0.0025700	0.0025700	4.64E-10
GA	0.0077561	0.0132865	0.0139508	9.13E-04	0.0025866	0.0026136	0.0026192	5.90E-06
NLS	0.0077474	0.0077474	0.0077474	1.55E-11	0.0025700	0.0026008	0.0026209	2.14E-05

Table 4-6: Statistical analysis of the results obtained for case 4

Case 4	Model error (P)				Model error (Q)			
	min	avg	max	std. dev.	min	avg	max	std. dev.
IPSO	0.0059985	0.0059985	0.0059985	4.47E-16	0.0012055	0.0012055	0.0012055	1.98E-12
GA	0.0120929	0.0122851	0.0124505	7.06E-05	0.0013188	0.0013843	0.0013899	1.19E-05
NLS	0.0059985	0.0065882	0.012563	1.88E-03	0.0012055	0.0013441	0.0013910	7.84E-05

Table 4-7: Statistical analysis of the results obtained for case 5

Case 5	Model error (P)				Model error (Q)			
	min	avg	max	std. dev.	min	avg	max	std. dev.
IPSO	0.0048652	0.0048652	0.0048652	2.42E-12	0.0024113	0.0024113	0.0024113	3.06E-14
GA	0.0048668	0.0050443	0.0051557	7.21E-05	0.0024118	0.0024133	0.0024141	4.81E-07
NLS	0.0048652	0.0048652	0.0048652	1.21E-11	0.0024113	0.0024132	0.0024213	1.73E-06

Table 4-8: Statistical analysis of the results obtained for case 6

Case 6	Model error (P)				Model error (Q)			
	min	avg	max	std. dev.	min	avg	max	std. dev.
IPSO	0.0031274	0.0031274	0.0031274	2.45E-16	0.0017985	0.0017985	0.0017986	7.49E-09
GA	0.0068328	0.0077004	0.0083967	3.97E-04	0.0023724	0.0023886	0.0023927	5.46E-06
NLS	0.0031274	0.0031274	0.0031274	1.86E-12	0.0017985	0.0021534	0.0023929	2.91E-04

Table 4-9: Statistical analysis of the results obtained for case 7

Case 7	Model error (P)				Model error (Q)			
	min	avg	max	std. dev.	min	avg	max	std. dev.
IPSO	0.0082899	0.0082899	0.0082899	2.24E-11	0.0029691	0.0029691	0.0029691	1.01E-16
GA	0.0082901	0.0086336	0.0092657	3.23E-04	0.0035929	0.0037773	0.0038313	3.50E-05
NLS	0.0082899	0.0082899	0.0082899	6.81E-13	0.0029691	0.0029780	0.0038554	8.86E-05

Table 4-10: Statistical analysis of the results obtained for case 8

Case 8	Model error (P)				Model error (Q)			
	min	avg	max	std. dev.	min	avg	max	std. dev.
IPSO	0.0039138	0.0039138	0.0039138	5.21E-15	0.0015622	0.0015622	0.0015622	4.04E-17
GA	0.0059742	0.0084948	0.0102355	1.11E-03	0.0015629	0.0025615	0.0026095	1.21E-04
NLS	0.0039138	0.0039138	0.0039138	3.30E-13	0.0015622	0.0018878	0.0026168	4.88E-04

4.4.2. Composite Load Model

4.4.2.1. Measurement Data

This section uses synthetic data generated using the DIgSILENT software [61]. For preliminary testing a simple two-bus system has been used. The single-line diagram of this configuration is depicted in Figure 4-20. A programmable voltage source is connected to Bus 2 and supplies a group of load connected to Bus 1. The load consists of an Induction Motor model connected in parallel with a static load model. The dynamic load response is exposed by simulating a voltage step change at Bus 2.

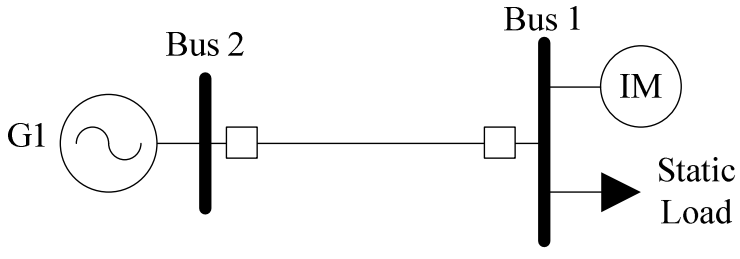

Figure 4-20: Single-line diagram of the two-bus system

In the second stage a much more complex network has been used – the IEEE 39-bus test system [92], the single-line diagram of which is depicted in Figure 4-21. A combination of dynamic and static load, similar to the one depicted in Figure 4-20,

has been connected to bus 4 through an additional transformer. The measurements of *V*, *P* and *Q* have been taken at the same bus.

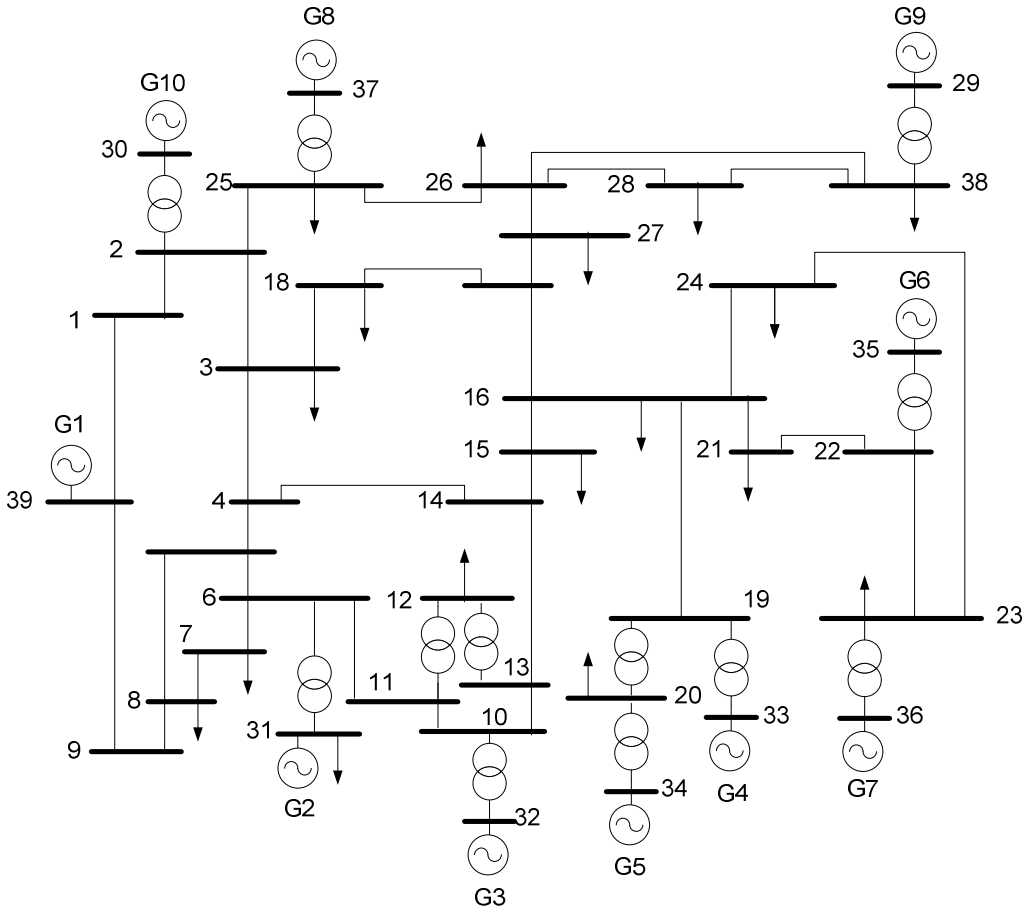

Figure 4-21: Single-line diagram of the IEEE 39-bus test system

The purpose of using a more complex system, where the measurements are only taken locally, is to imitate more realistic conditions and behaviour of the interconnected elements. The voltage in the simple network will behave exactly as programmed, producing a clear step change. However, this is not the case in a real power system, where the voltage at each point is affected by many elements. For this reason, the 39-bus system includes dynamic data of the connected generators as well as their Automatic Voltage Regulators (AVR). The voltage change at the load point is forced through a transformer step change. This has been found to be most effective because it allows the load dynamics to be exposed and at the same time two different steady states, pre- and post-disturbance, can be observed. This maximizes the amount of information contained in a single measurement.

4.4.2.2. Trajectory Sensitivity Analysis

Trajectory sensitivity analysis of active and reactive powers can give some practical insight into the identifiability of parameters of the IM model. For this purpose, a voltage measurement is taken and based on that the model's states are obtained for a given set of parameters. Then, the trajectory sensitivities can be obtained using the matrices given in Appendix D. This procedure has been repeated for different voltage disturbances and different sets of parameters. However, in all of the cases considered the results show very similar trends. Figure 4-22 to Figure 4-27 depicts trajectory sensitivities of active and reactive powers with respect to every parameter of the IM model.

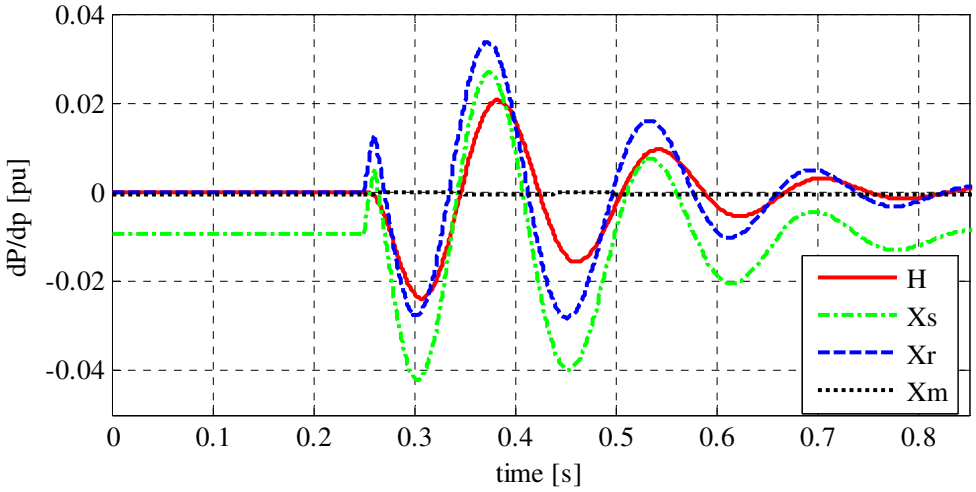

Figure 4-22: Trajectory sensitivities of active power with respect to *H*, *Xs*, *Xr* and *Xm*

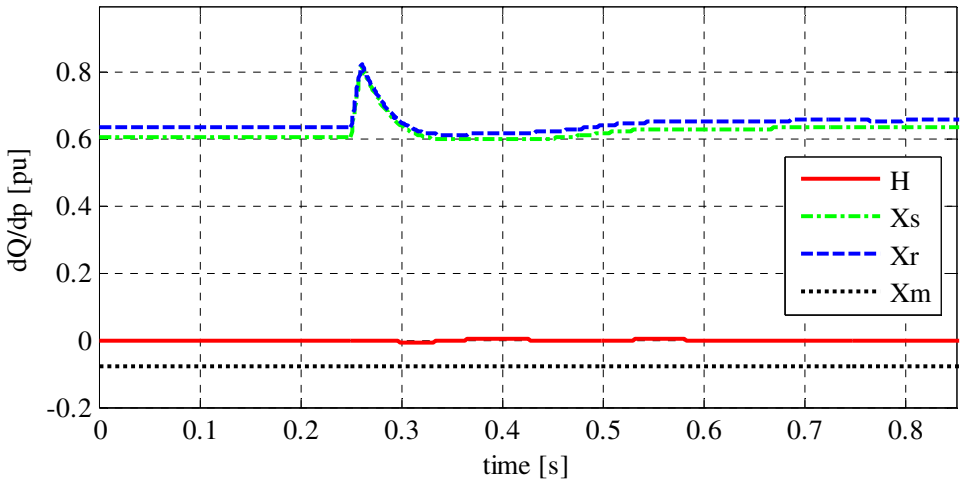

Figure 4-23: Trajectory sensitivities of reactive power with respect to *H*, *Xs*, *Xr* and *Xm*

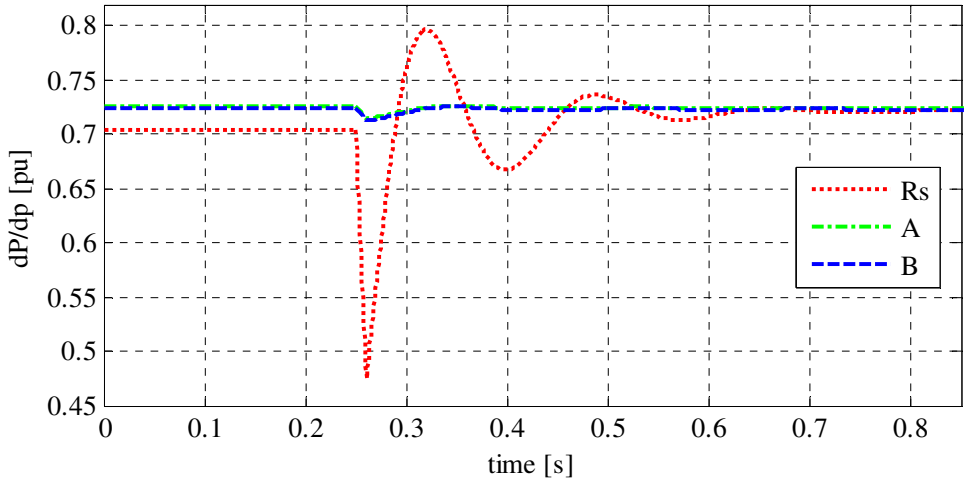

Figure 4-24: Trajectory sensitivities of active power with respect to *Rs*, *A* and *B*

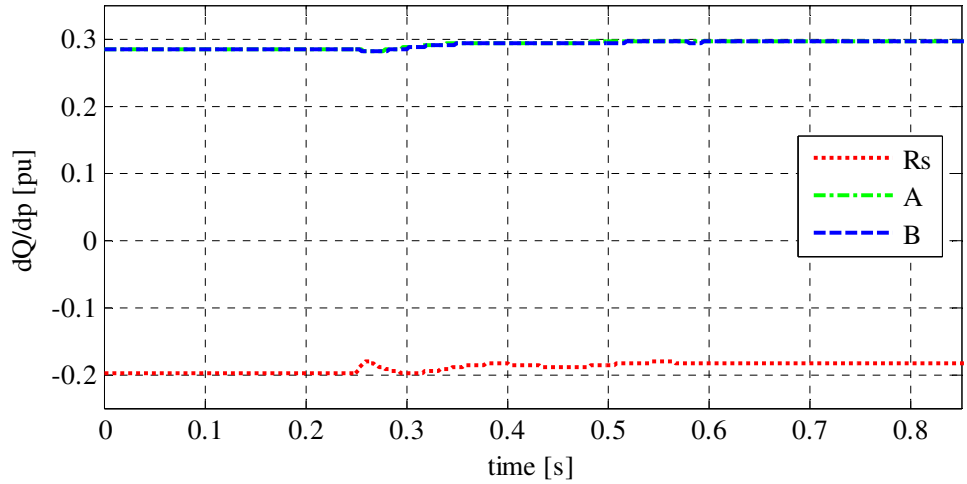

Figure 4-25: Trajectory sensitivities of reactive power with respect to *Rs*, *A* and *B*

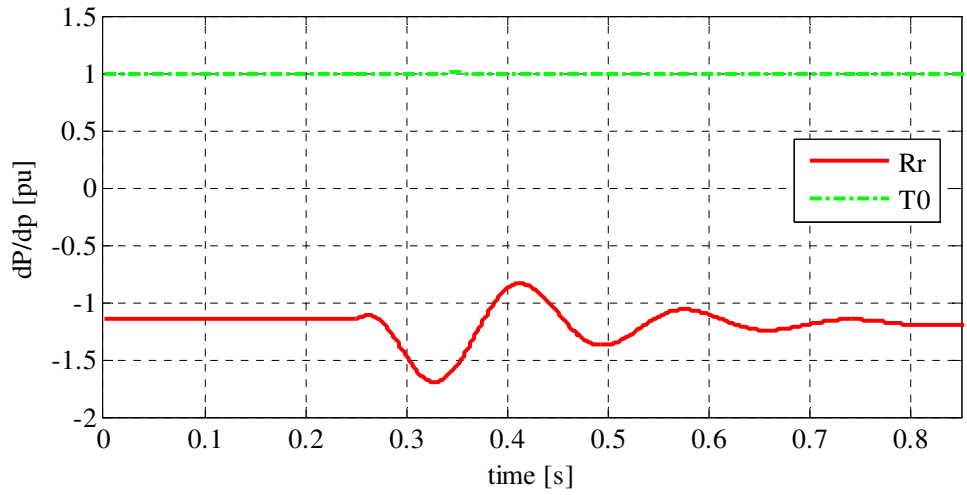

Figure 4-26: Trajectory sensitivities of active power with respect to *Rr* and T_0

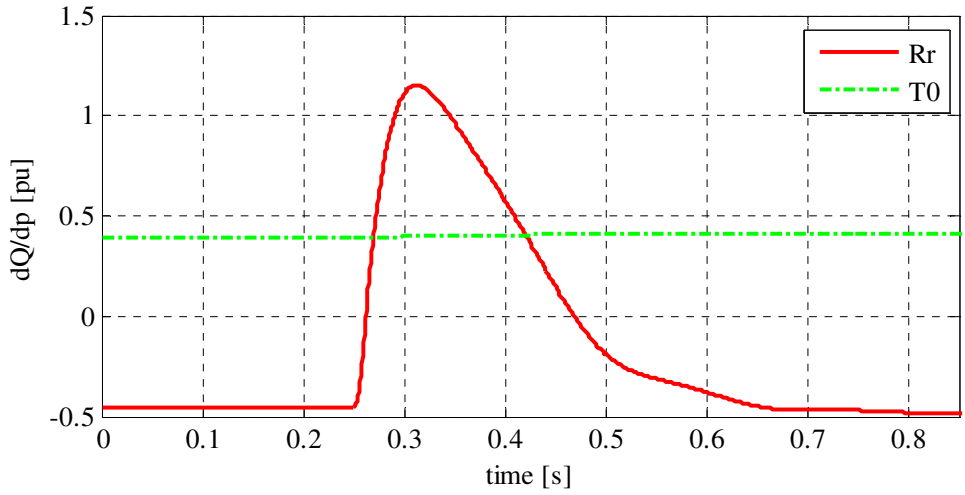

Figure 4-27: Trajectory sensitivities of reactive power with respect to *Rr* and T_0

After examining the plots, the parameters can be divided into several groups. Figure 4-22 shows that trajectory sensitivities of active power with respect to H, X_s, X_r and X_m are negligibly small, which means that it would be difficult to precisely identify these parameters from active power measurement. Figure 4-23 depicts the trajectory sensitivities of reactive power with respect to the same set of parameters. It is clear that the influence of H and X_m is still very small, so identifiability of these two parameters from the power measurements will be limited. However, trajectory sensitivities of reactive power with respect to X_s and X_r are better, especially during the dynamic transition. It should also be noted that H is a parameter that can only be estimated during a dynamic transition. Otherwise, static sensitivities of active and reactive powers with respect to this parameter are equal to 0.

Figure 4-24 and Figure 4-25 present trajectory sensitivities of active and reactive powers with respect to R_s, A and B. Sensitivities of active power with respect to all three parameters are significant and during the dynamic transition identifiability of R_s will vary more than A and B. In the case of reactive power the situation is worse, although the sensitivity is still noticeable, so the measurement of reactive power will provide additional information for the estimation process. The variation in the sensitivity during the dynamic transition is very small.

The last pair of plots given in Figure 4-26 and Figure 4-27 provides trajectory sensitivities of active and reactive powers with respect to R_r and T_0. These two

parameters have the strongest influence on both active and reactive power and for this reason they should present best identifiability. Additionally, sensitivity of reactive power with respect to R_r increases considerably during the dynamic transition, which should further improve identifiability of this parameter.

4.4.2.3. Tuning of the AI Methods

To ensure that both AI methods are optimally tuned for the estimation of the parameters of the CL model, a series of empirical studies has been carried out to find the best settings for this particular task. In each experiment one parameter has been changed in a predefined range, while the others were kept constant. In some cases, when a strong correlation between parameters was detected, two parameters were altered at once, whereas the rest were fixed. Table 4-11 contains all of the parameters together with their ranges for IPSO. In the case of GA, all three parameters, Crossover Rate, Crossover Point and Mutation Rate, are between 0 and 1.

Table 4-11: IPSO parameters

Parameter	Range
Crossover Rate	[0;1]
c_1, c_2	[0;4] $c_1 + c_2 \leq 4$
$\Phi_{initial}$	[0.5;1]
Φ_{final}	[0;0.5]
n	[0.5;1.5]

Starting with the Crossover Rate, it has been changed according to the range given in Table 4-11 in 0.1 steps. For each setting a 100 simulation has been carried out to obtain a mean value of the maximum fitness reached in each trial. Figure 4-28 presents a plot of these mean values for each setting of the Crossover Rate. Parameters c_1 and c_2 on the other hand have been tuned together, which produced the surface depicted in Figure 4-29. In this case each parameter has been varied in the defined range with a step of 0.4 with consideration of the inequality given in Table 4-11.

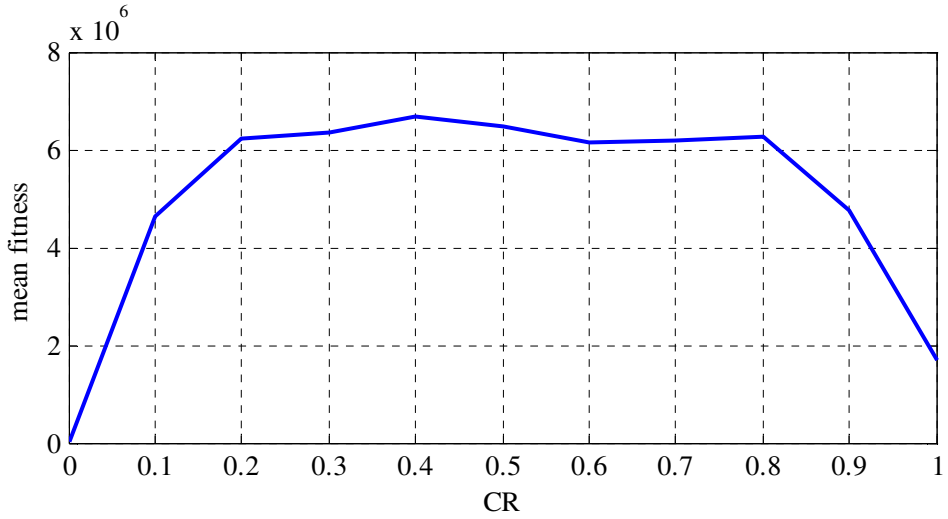

Figure 4-28: Tuning of the Crossover Rate for IPSO

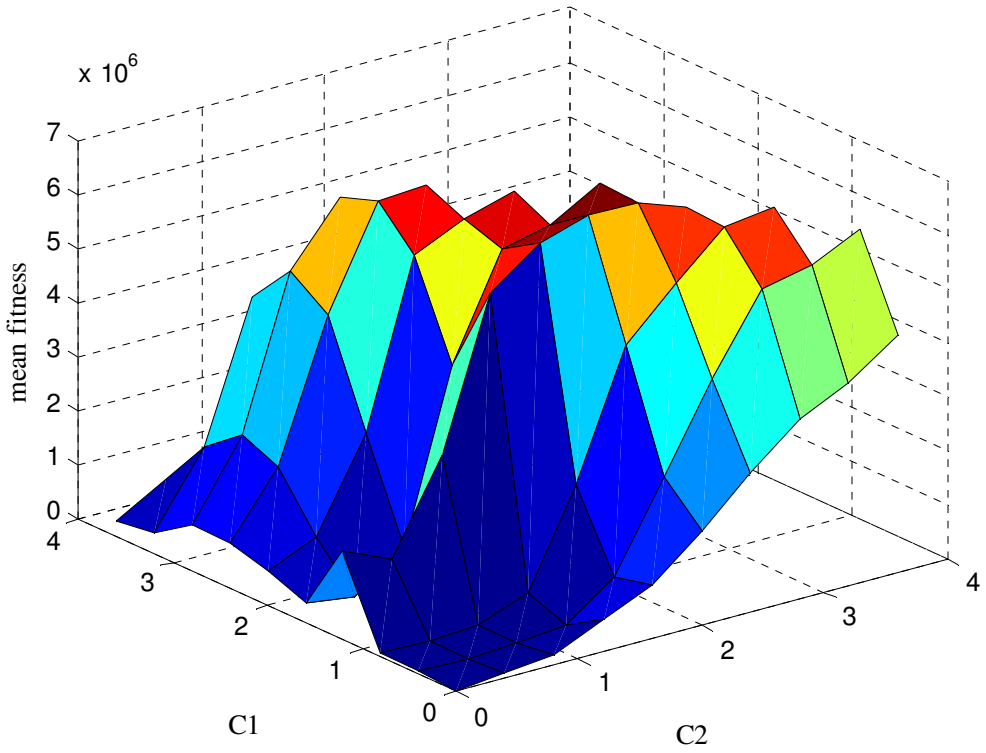

Figure 4-29: Tuning of the parameters c_1 and c_2 for IPSO

Figure 4-30 presents the tuning of the Mutation Rate for GA. All the remaining parameters have been tuned in a similar manner and Table 4-12 and Table 4-13 contain a summary of this procedure.

Table 4-12: Optimal values of IPSO parameters

Parameter	Value
Crossover Rate	0.4
c_1	1.6
c_2	2.4
$\Phi_{initial}$	0.9
Φ_{final}	0.4
n	1.1

Table 4-13: Optimal values of GA parameters

Parameter	Value
Crossover Rate	0.9
Crossover Point	0.25
Mutation Rate	0.1

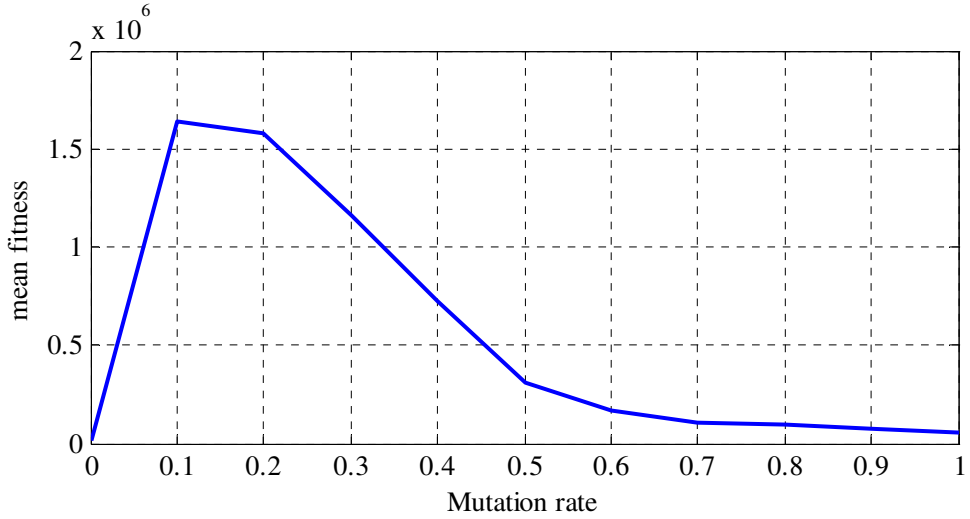

Figure 4-30: Tuning of the Mutation Rate for GA

4.4.2.4. Estimation Results

Similarly to the section devoted to the Exponential Recovery Load model, the results presented here are based on a set of 100 trials for each case. Additionally, selected runs are compared against the model parameters used in the simulation in the DIgSILENT software. Here, the time scale is much shorter due to the faster dynamics of the motor and for this reason the sampling frequency in all cases has been set to 1600Hz. The searching space (Table 4-14) for this part of the project was defined based on the typical values of Induction Motor model parameters that are presented in [1], [3] and [93]. This searching space has been used to generate the initial population of 100 individuals (candidate solutions).

Table 4-14: Searching space for the Composite Load model

Parameter	Searching space	
	min	max
H	0.2	2
R_s	0.001	0.1
X_s	0.05	0.2
R_r	0.01	0.1
X_r	0.1	0.3
X_m	2	4
A	0	1
B	0	1
K_p	0.2	0.8
T_0	0.5	1
α	0	4
β	0	4

The measurements for the first case were obtained using the simple 2-bus system (Figure 4-20). A step change of -1.5% has been applied to the voltage at t=0.25s, which in turn exposed the dynamic response of the load. Figure 4-31 depicts the P and Q measurements.

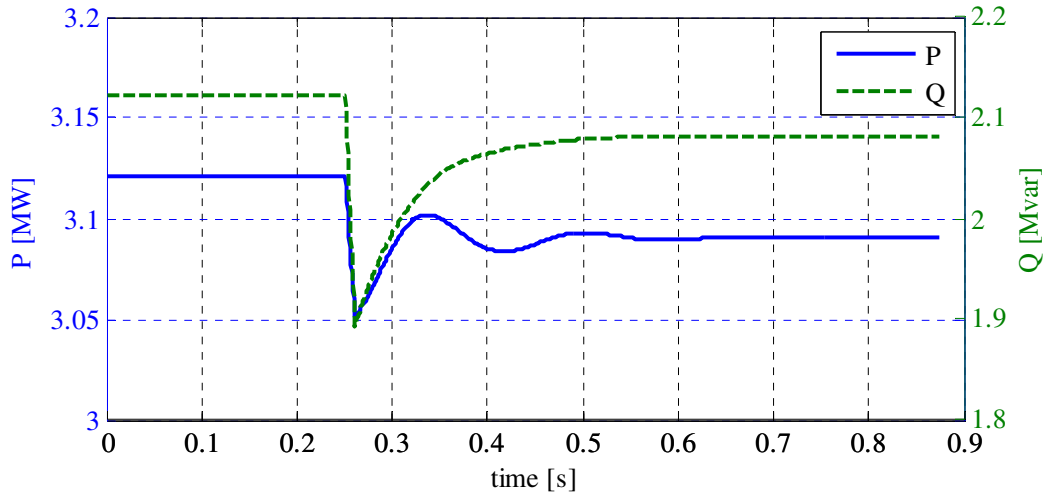

Figure 4-31: Measurements of active and reactive power: Case 1

It should be noted that P and Q are represented by a CL model that cannot be decoupled and estimated separately like in the case of the ERL model in the previous section. Here, the objective function needs to be slightly modified to include both quantities. To achieve this, the model output, denoted by $M()$ in (4.26), is formulated in the following way:

$$M(\theta_{CL}, V_m, P_m, Q_m) = (P_m - P_e(\theta_{CL}, V_m))^2 + (Q_m - Q_e(\theta_{CL}, V_m))^2 \quad (4.42)$$

where V_m, P_m and Q_m are the measured voltage, active and reactive power, respectively and P_e and Q_e are the estimated active and reactive power, respectively. Now, the second term in (4.26), denoted by y, can be set to a series of zeros, which will ensure minimization of (4.42) through (4.25).

Figure 4-32 shows the minimum, average and maximum convergence curves obtained based on 100 trials for the first case. Again, IPSO shows higher accuracy, speed and reliability when compared to GA. Detailed statistical analysis of the final results, including NLS, can be found in Table 4-15. Additionally, the table also includes analysis of the results obtained using the Hybrid approach (GA + NLS), in which the solutions reached by GA are used as the initial guess for NLS.

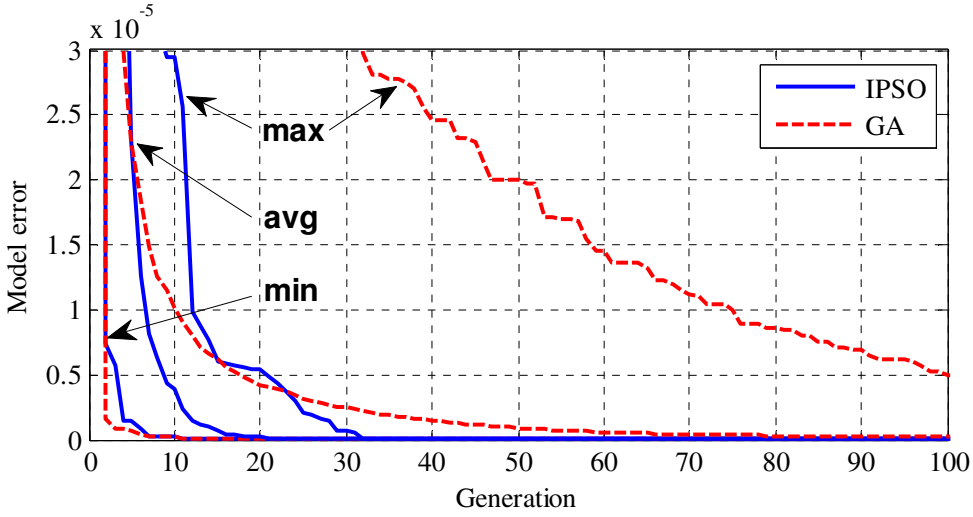

Figure 4-32: Convergence curves for AI methods: min, average and max values: Case 1

Table 4-15: Statistical analysis of the results obtained for case 1

Case 1	Model error			
	min	avg	max	std. dev.
IPSO	9.46E-10	1.11E-09	4.94E-09	4.88E-10
GA	1.31E-09	1.64E-07	4.99E-06	7.11E-07
NLS	9.95E-10	1.33E-03	3.03E-02	4.82E-03
Hybrid	1.25E-09	3.02E-08	9.53E-07	1.32E-07

The results obtained by using NLS demonstrate the high degree of complexity present in this problem. The difference between the best and the worst optimum is

considerable, which is also reflected in the high standard deviation. This means that a large number of local optima are present and a poorly selected initial guess will result in a high model error in most cases. Compared to both AI methods, the performance of the NLS is not acceptable. The situation is different for the Hybrid technique. From Table 4-15 it is clear that NLS can improve the accuracy of GA even though the difference is not dramatic. Statistically, IPSO still gives the best results.

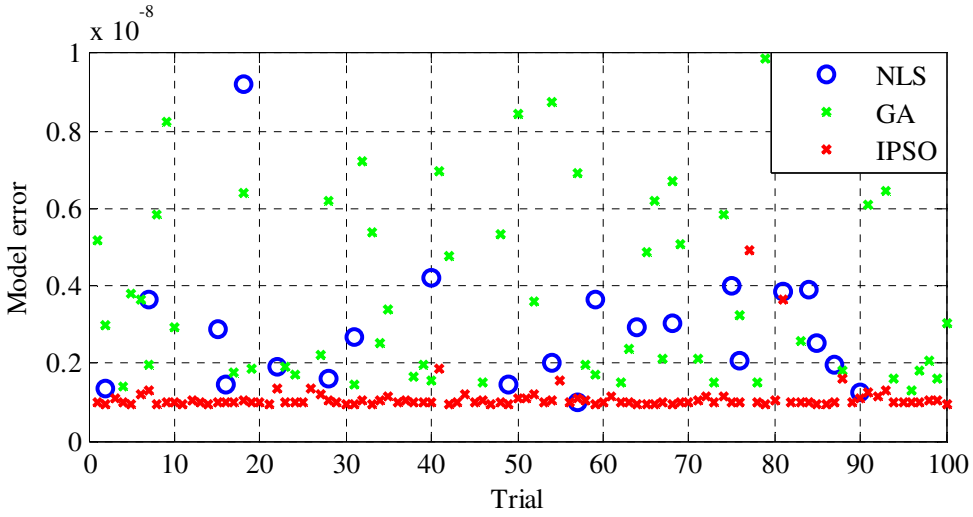

Figure 4-33: Model error of the final solutions: Case 1

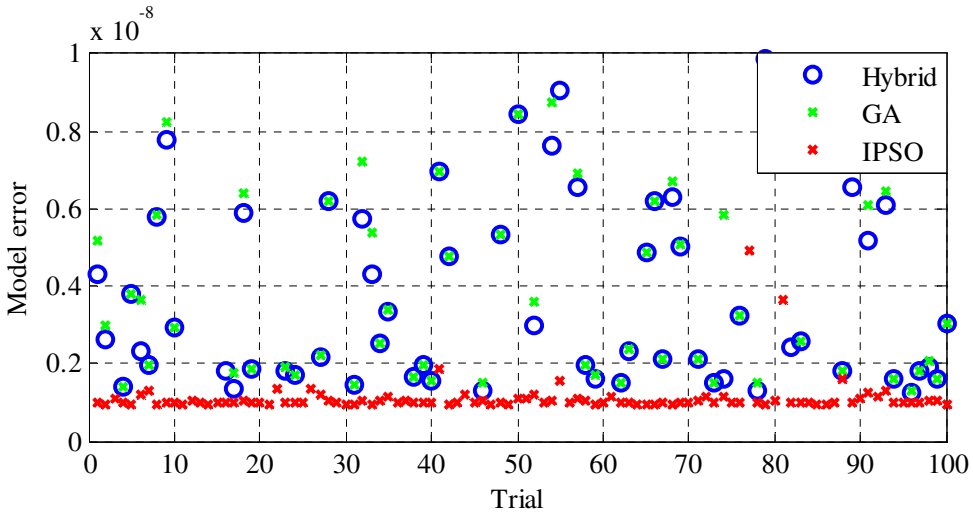

Figure 4-34: Model error of the final solutions including Hybrid approach: Case 1

Figure 4-33 and Figure 4-34 depict the model error for every trial of Case 1. The first plot includes the results obtained using NLS, compared against the AI methods, and the second one presents the results achieved using the Hybrid technique instead. The

actual improvement introduced by the combination of GA and NLS is not very significant. What is more, in some cases there is virtually no improvement, which means that the GA has already converged to one of the local minima. This shows a dangerous situation where different local optima give a very similar model error, which ensures that the task is difficult. Table 4-16 provides a comparison between the values of the model parameters used in DIgSILENT and their estimates obtained by each method in their best trial. The table also includes a relative error [31] of the *P* and *Q* fitting calculated according to the following formula:

$$\varepsilon(y) = 100 \frac{\sqrt{\frac{1}{n}\sum_{k=1}^{n}(y_{mk} - y_{ek})^2}}{\sqrt{\frac{1}{n}\sum_{k=1}^{n} y_{mk}{}^2}} \tag{4.43}$$

where y_m and y_e are the measured and estimated signals, respectively (active or reactive power) and n is the number of samples included in the measurement.

Table 4-16: Parameters obtained in the best trial: Case 1

Parameters	True	IPSO	GA	NLS	Hybrid
H	0.5883	0.4461	0.4713	0.5561	0.4710
R_s	0.01	0.0086	0.0108	0.0087	0.0104
X_s	0.1	0.0865	0.0828	0.1506	0.0828
R_r	0.01	0.0113	0.0114	0.0090	0.0113
X_r	0.08	0.1203	0.1230	0.0194	0.1223
X_m	3	2.9183	3.3447	2.7577	3.3447
A	1	0.9937	0.7631	0.7653	0.7631
B	0	0.0015	0.2161	0.3396	0.2161
K_p	0.6796	0.7047	0.6628	0.6645	0.6616
T_0	1	0.8281	0.7753	0.9242	0.7767
α	2	2.1903	1.8716	1.9522	1.8720
β	2	2.2354	1.9806	1.9742	1.9805
error P [%]	-	0.0115	0.0117	0.0113	0.0100
error Q [%]	-	0.0209	0.0200	0.0210	0.0214

Although the accuracy of the results presented in Table 4-16 is quite similar for all of the methods, the estimated parameters present some discrepancies. The actual fitting is very accurate, which is also confirmed by Figure 4-35, which shows the absolute differences between the true *P* and *Q* and the estimated ones. However, this phenomenon is not related to the estimation methods but to the model itself. It has been recognised, that some load models may present a plateau effect [79], which

means that under some conditions flat surfaces may exist in the solution space. This in turn will cause a region of solutions to produce very similar fitting error. Of course the difference between these solutions, in terms of estimated parameters, will not be dramatic, but definitely noticeable. It is suggested in [79] that one way overcome this is to reduce the number of parameters of the model, an approach investigated successfully in [25]. As it has also been shown in previous subsection, the sensitivity of the CL model with respect to some of its parameters is small, which means that the observability of these parameters is limited. This, on the other hand, will affect the accuracy of estimation of the unknown model parameters.

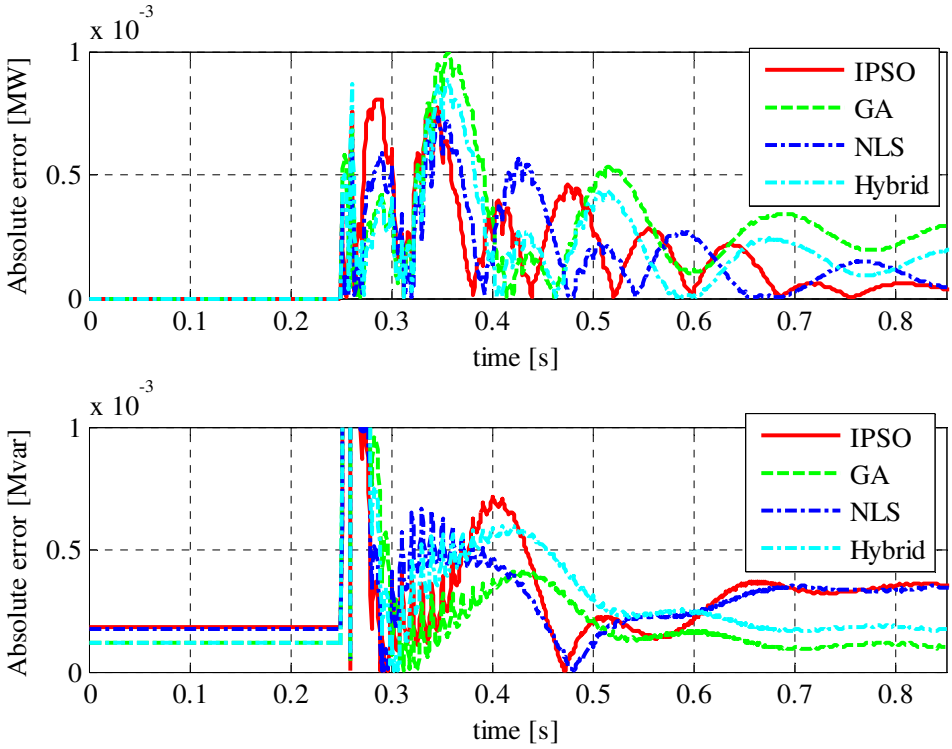

Figure 4-35: Absolute errors for the best estimates: Case 1

For comparison, Table 4-17 presents the values of the estimated parameters with accuracy close to the average for each method. Now, the discrepancies are more pronounced due to the bigger differences between the fitting accuracies achieved by each estimation method. Except NLS, all other methods show quite acceptable performance, which can be clearly seen in Figure 4-36. The curve estimated by IPSO virtually overlaps the true measurement of active power obtained from the simulation, the Hybrid technique follows quite closely and GA is slightly further away, but still

acceptable with a relative error below 0.1%. However, NLS has a relative error of almost 0.7%, which represents a very poor fitting that does not at all reflect the dynamic behaviour of the model.

Table 4-17: Parameters obtained in the average trial: Case 1

Parameters	True	IPSO	GA	NLS	Hybrid
H	0.5883	0.4402	0.3795	1.4397	0.4380
R_s	0.01	0.0137	0.0279	0.0404	0.0147
X_s	0.1	0.0929	0.1427	0.1524	0.1176
R_r	0.01	0.0123	0.0142	0.0092	0.0123
X_r	0.08	0.1308	0.1148	0.1734	0.1088
X_m	3	3.2498	2.8341	3.5546	3.1983
A	1	1.0000	0.8234	0.8466	0.7631
B	0	0.0000	0.1695	0.1878	0.0268
K_p	0.6796	0.6168	0.6979	0.4410	0.6105
T_0	1	0.6438	0.6188	0.5219	0.6244
α	2	1.7096	1.9303	2.0346	1.5084
β	2	1.7126	2.1133	2.0166	1.6208
error P [%]	-	0.0103	0.0784	0.6829	0.0488
error Q [%]	-	0.0210	0.0237	0.7291	0.0328

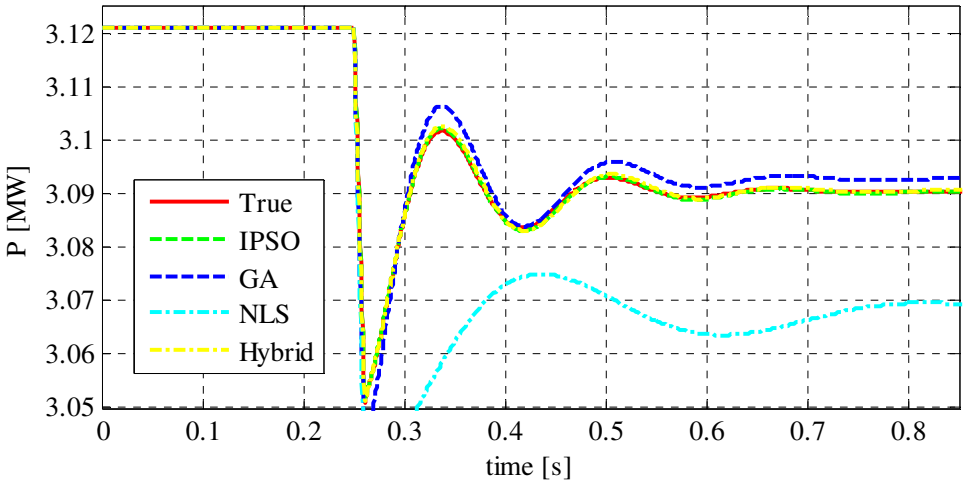

Figure 4-36: Estimated active power against the true measurement: Case 1

The remaining cases were produced using the IEEE 39-bus test system. The advantage of using such a system is a more realistic bus voltage response and this in turn has an impact on the response of the load. The second case investigated uses the same load model data as in the case of the simple 2-bus system. The voltage change has been provoked by using a transformer tap changer. Similarly to the previous case, the magnitude of the voltage step was -1.5%. Figure 4-37 presents the convergence

curves for the AI methods and Table 4-18 summarizes the results obtained by all of the methods in the 100 trials.

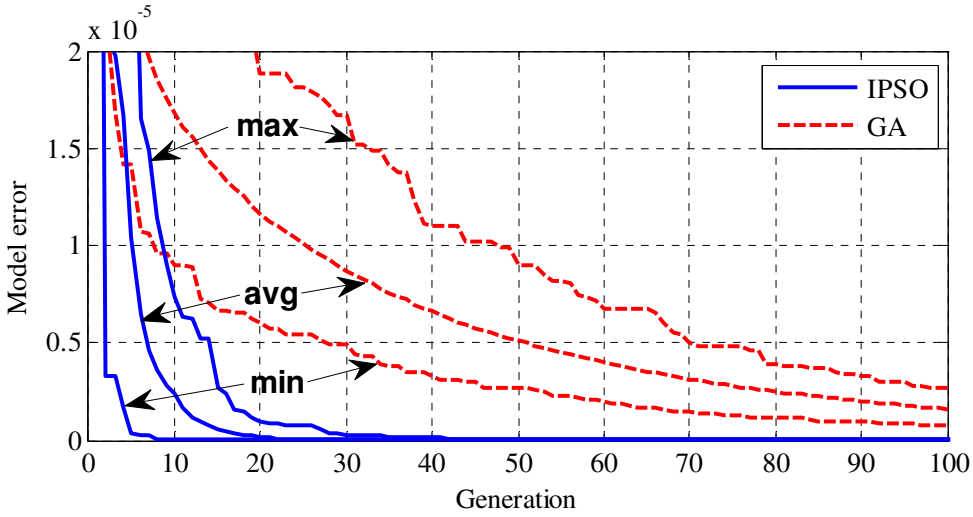

Figure 4-37: Convergence curves for AI methods: min, average and max values: Case 2

Table 4-18: Statistical analysis of the results obtained for case 2

Case 2	Model error			
	min	avg	max	std. dev.
IPSO	2.19E-11	1.29E-10	3.39E-09	3.66E-10
GA	7.21E-07	1.62E-06	2.72E-06	3.83E-07
NLS	2.61E-11	1.44E-03	3.80E-02	5.18E-03
Hybrid	2.72E-11	3.73E-07	2.21E-06	5.81E-07

The statistical results follow a similar trend to the previous case. Table 4-19 on the other hand, presents the values of estimated parameters in the best trial. When compared to the corresponding results from the previous case the behaviour here is different. For example, in Case 1 all of the methods usually underestimated the inertia constant *H*, whereas in Case 2 its value is overestimated. What is more, this trend is confirmed by the mean value of *H* obtained by IPSO in both cases. For comparison, Case 3 presents results obtained using the same parameters; however, this time the voltage change has been provoked by a transient fault on line 26-29 at *t*=0.35s. After 0.1s the fault has been cleared and the system returned to its previous state. Figure 4-38 shows the recorded active and reactive power.

Table 4-19: Parameters obtained in the best trial: Case 2

Parameters	True	IPSO	GA	NLS	Hybrid
H	0.5883	0.5451	0.7951	0.7437	0.6701
R_s	0.01	0.0094	0.0252	0.0068	0.0079
X_s	0.1	0.1188	0.1267	-0.0545	0.0396
R_r	0.01	0.0156	0.0162	0.0132	0.0135
X_r	0.08	0.1177	0.1011	0.2508	0.1624
X_m	3	2.1166	2.6123	2.7582	1.8835
A	1	0.9653	0.2848	0.5494	0.5491
B	0	0.0046	0.5950	0.5445	0.7248
K_p	0.6796	0.5913	0.7019	0.6018	0.5805
T_0	1	0.5603	0.7287	0.7921	0.6750
α	2	1.5584	1.6472	1.5983	1.5192
β	2	1.0969	2.3001	1.6920	1.1202
error P [%]	-	0.0044	0.1294	0.0063	0.0052
error Q [%]	-	0.0060	0.0609	0.0086	0.0075

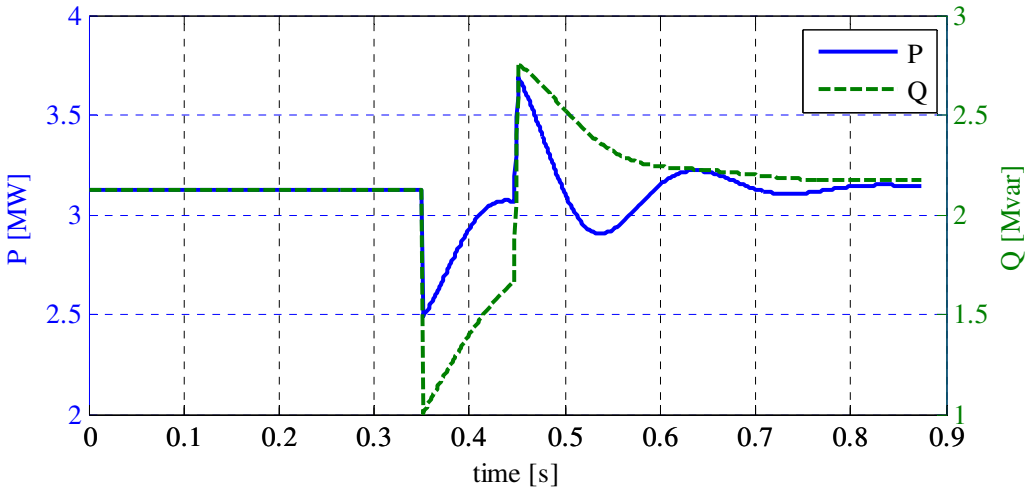

Figure 4-38: Measurements of active and reactive power: Case 3

Statistical analysis of the results follows a trend very similar to the previous two cases. Of more interest are the values of the estimated model parameters presented in Table 4-20. Considerable discrepancies can be observed in the table, with the NLS method reaching negative values in a few cases. The important fact is that, once again, the estimated parameters have different values compared to those estimated in the previous two cases. This is also confirmed by the mean values of the parameters estimated by IPSO in all three of the cases considered, this data is presented in Table 4-21. These results show that the estimated parameters oscillate, from trial to trial, around a value which is not necessarily the true one. These discrepancies should be attributed to the only factor which is changing in the three discussed cases – the measured voltage response (Figure 4-39).

Table 4-20: Parameters obtained in the best trial: Case 3

Parameters	True	IPSO	GA	NLS	Hybrid
H	0.5883	0.7395	0.5568	0.7969	0.7776
R_s	0.01	0.0859	0.0955	0.0628	0.0873
X_s	0.1	0.0605	0.1053	-0.2485	0.0772
R_r	0.01	0.0151	0.0167	0.0134	0.0151
X_r	0.08	0.1175	0.1033	0.4274	0.0983
X_m	3	3.9961	3.9447	4.6269	3.9029
A	1	0.0007	0.6188	-2.4462	0.2344
B	0	0.0179	0.1050	-0.8642	0.0207
K_p	0.6796	0.5209	0.5850	0.5902	0.4941
T_0	1	0.5181	0.5025	0.7809	0.4886
α	2	0.9561	1.3109	1.3722	0.9230
β	2	1.1720	1.2111	1.4482	1.1426
error P [%]	-	0.9184	0.8298	0.9161	0.8526
error Q [%]	-	1.1691	1.1826	1.1037	1.1759

Table 4-21: Mean values of model parameters obtained by IPSO: Cases 1, 2 and 3

Parameters	H	R_s	X_s	R_r	X_r	X_m	A	B	K_p	T_0	α	β
True	0.5883	0.01	0.1	0.01	0.08	3	1	0	0.6796	1	2	2
Case 1	0.3895	0.0119	0.1011	0.0134	0.1440	2.83	0.97	0.02	0.6663	0.65	1.98	2.01
Case 2	0.6270	0.0084	0.0983	0.0149	0.1249	2.91	0.89	0.10	0.5985	0.63	1.62	1.69
Case 3	0.5670	0.0912	0.0731	0.0165	0.1323	3.96	0.03	0.05	0.6213	0.56	1.22	1.23

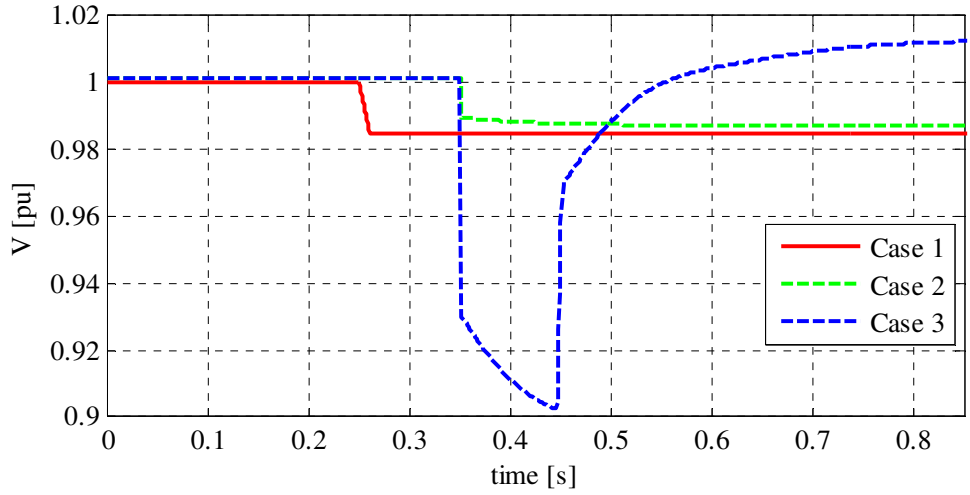

Figure 4-39: Measurements of voltage: Case 1, 2 and 3

The voltage signal is in fact the control input of the CL model and for this reason it will influence the model's response and this in turn may affect its observability. Table 4-21 shows how different types of voltage responses influence the estimated values of the parameters. It should be noted that the mean values were obtained using IPSO, because this method, in all three cases, gave very accurate and consistent curve fitting

results for each run. From the table it is clear that the most dramatic discrepancies in the estimated parameters can be found in Case 3, where R_s and X_m are significantly overestimated and parameters A, α and β are underestimated. In addition, a strong correlation can be observed between parameters A, α and β, which is understandable since they all have significant influence on the steady state behaviour of the model. From the results obtained, the best practice seems to be utilization of a transformer tap changer as a mechanism for provoking the voltage deviations. It could also be beneficial to combine several disturbances into one set of data to increase the amount of information included and minimize the number of possible solutions. Either way it should be kept in mind that the selection of measurement data will affect the results obtained, regardless of the selected estimation method.

In the final case presented, behaviour of the estimation techniques will be investigated for a more complex load composition. Maintaining the same network as in Case 2 and 3, the load now consists of a large industrial IM [93], a small industrial IM [93] and a static load in a proportion of 50%, 25% and 25%, respectively. However, the load model structure remains the same as in the previous cases, namely an IM model connected in parallel with a static load model. This means that the IM model will need to become an equivalent representation of the two types of motors connected to the bus. In reality this task may be even more complex as a wide range of induction motors may be used.

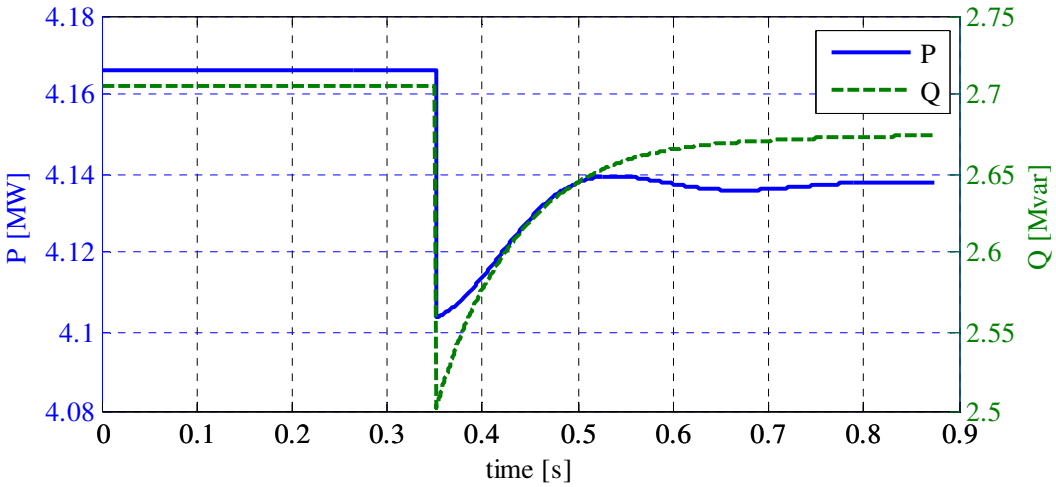

Figure 4-40: Measurements of active and reactive power: Case 4

Figure 4-40 shows the load response to a -1.5% voltage step change provoked by a transformer tap changer at t=0.35s, this is essentially the same disturbance as in Case 2. The convergence curves of the AI methods are depicted in Figure 4-41 and statistical analysis of all of the results obtained in the 100 trials for each technique is presented in Table 4-22. It is clear that IPSO is faster than GA as well as being more accurate and reliable than the other methods.

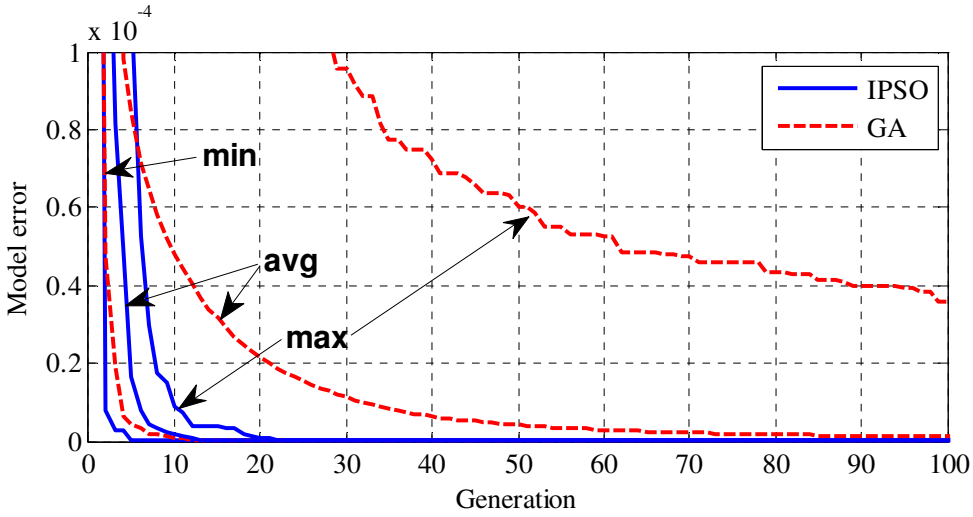

Figure 4-41: Convergence curves for AI methods: min, average and max values: Case 4

Table 4-22: Statistical analysis of the results obtained for case 4

Case 4	Model error			
	min	avg	max	std. dev.
IPSO	7.06E-11	2.88E-10	1.29E-09	2.12E-10
GA	1.21E-09	1.06E-06	3.58E-05	3.86E-06
NLS	5.74E-11	1.55E-03	3.85E-02	5.64E-03
Hybrid	3.08E-10	6.65E-07	3.11E-05	3.15E-06

Table 4-23 includes the parameter values estimated by each method in their best trial, which corresponds to the cases with best fitting. Although the dynamic behaviour of the load is reflected very well, the differences between the estimated parameters can be considerable and NLS reached negative values. The multiple solutions and plateau effects are even more pronounced here, which means that more training data may be required to increase the observability. Regardless of this fact, IPSO is still capable of obtaining consistent and accurate results.

Table 4-23: Parameters obtained in the best trial: Case 4

	True		Estimated			
Parameters	big IM	small IM	IPSO	GA	NLS	Hybrid
H	1.5	0.7	1.2375	0.8110	1.3353	0.6169
R_s	0.013	0.031	0.0119	0.0039	0.0107	0.0122
X_s	0.067	0.1	0.0623	0.1716	0.4702	0.1437
R_r	0.009	0.018	0.0122	0.0145	0.0075	0.0216
X_r	0.17	0.18	0.1761	0.1106	-0.2274	0.2608
X_m	3.8	3.2	2.4549	2.0714	1.8391	3.3358
A	1	1	0.6138	0.1186	-0.1568	0.9485
B	0	0	0.2428	0.5251	-0.2503	0.0245
K_p	0.764		0.6616	0.7467	0.6351	0.7459
T_0	1	1	0.7706	0.7462	0.7888	0.5247
α	2		1.3719	1.8500	1.3538	1.7222
β	2		0.7622	3.5019	0.5785	1.9836
error P [%]	-	-	0.0063	0.0100	0.0052	0.0078
error Q [%]	-	-	0.0099	0.0204	0.0104	0.0155

4.4.3. Computational Burden

The four estimation approaches presented in this chapter have rather different computational requirements. As before, it is a trade-off between speed and searching abilities. At this stage, estimation of load model parameters is not considered a critical real-time application, and for this reason the speed of the selected method is not a crucial factor. However, this does not change the fact that the AI techniques are very demanding when compared to the NLS. Table 4-24 presents a comparison of the computational performance based on 100 trials for an arbitrarily selected case.

Table 4-24: Mean time performance of the estimation methods

Method	IPSO	GA	NLS	Hybrid
Time [s]	10.24	10.17	1.16	11.06

It can be seen that the mean execution time is very similar for both AI methods. This is mostly due to the fact that most CPU resources are consumed during the repetitive calculation of the fitness function, which is the same for both algorithms. NLS is considerably faster and the Hybrid approach is the slowest since it combines the execution of two algorithms. This could be optimized by reducing the number of generations for GA. However, the execution time was not the main concern in this application of the method. Similarly, the execution time of IPSO could be reduced, at

least in some cases, but for comparison reasons the number of generations have been kept fixed at 100 for both AI techniques.

In general, the execution time of the AI methods is their biggest disadvantage, but as long as this factor is not critical for a particular application, it is still acceptable. It also should be noted that since the parameters of a selected model can be determined only after a disturbance that provides sufficient observability of the dynamic behaviour, the time between such events is usually long enough to perform the estimation before another possible event occurs. This still allows online monitoring of load parameters by tracking of the voltage behaviour. For example, it could be achieved through the use of Wide Area Monitoring System (WAMS) technology at the control centre level.

4.5. Conclusions

Results presented in this chapter prove that the application of IPSO to estimate unknown load model parameters can have several advantages over other popular methods. The primary aim of this part of the work presented here was to improve the reliability of results. Nonlinear dynamic load models, like the ERL model or the CL model, most often present the problem of multiple solutions, an issue which proved to have strong impact on the traditional NLS technique. Depending on the initial guess, this method would most likely converge to the closest optimum. In the case of the ERL model, the problem is not as serious as only a pair of minima would usually be identified. However, the situation is very different when it comes to the CL model. Looking at some of the cases it can be easily observed that the model error results in the 100 trials for the NLS were scattered in a wide range. The method is fast, and can be accurate, but it is also very unreliable when it is used to optimize complex nonlinear problems.

The local limitation of NLS was somewhat addressed through the introduction of GA. This AI technique improved the reliability of the results; however, it suffered from other issues. Premature convergence manifests itself similarly to the problem of local convergence in the case of NLS. This phenomenon is a result of GA not being able to

make further progression due to the lack of sufficient diversity in a population. After a number of generations the individuals in a population become very similar, which makes it impossible for the method to make a significant improvement. In some cases this will cause the technique to become stuck in a local minimum, although this is still less probable that in case of NLS. One way of limiting this phenomenon would be to increase the size of a population for complex tasks, but this in turn will increase the execution time and at some point may become impractical.

IPSO offered a considerable improvement in reliability over the other methods. It proved to have high efficiency by returning very consistent results. The model errors, from run to run, showed small differences which is confirmed by IPSO having the smallest standard deviation in each experiment.

Accuracy is another important factor that will determine whether a method is useful or not. NLS is very accurate, but only within the minimum it finds, which means that globally the accuracy will still be dependent on the initial guess. GA on the other hand has weaker fine tuning capabilities, but it is much better at finding more promising areas in the searching space. These specific characteristics led to the development of combining the advantages of both methods into a Hybrid approach. Through experiments with the CL model it has been proven that it is indeed beneficial to use the result obtained by GA as an initial guess for the NLS method, especially when GA suffers from premature convergence. It should be noticed however that if GA identifies one of the local minima, then NLS will only improve the accuracy within this region.

In terms of accuracy, IPSO again outperforms the other methods. With the same initial conditions as GA (initial population, population size and number of generations), the technique presented much better accuracy and higher speed of convergence. In most cases presented in this chapter, IPSO gives the best mean accuracy and also the smallest minimum model error.

Computational burden is the only area where IPSO is not superior to the other methods. It has computational requirements typical for AI techniques, where a high number of fitness function evaluations is required at each generation. On the other

hand, taking into account the other benefits offered by IPSO, it is not a high price to pay, especially for offline applications or applications without closed-loop control. In the end it is always a trade-off between computational cost and other desired features like accuracy and reliability.

Last, but not least, there are issues related directly to the model, which may strongly influence the results obtained. Trajectory sensitivity analysis showed that the impact of the parameters on the model's output can be very different. This in turn will influence the observability and the final accuracy of the estimated parameters. However, it should be noticed that since a given parameter has a very low impact on the model's output, the accuracy of its estimation should not be a concern. The issue of observability can also be related to the type of voltage disturbance. It has been shown that it is best when the measurements include two different steady states. Otherwise, the accuracy of the estimation of the parameters that belong to the static part of the model will be worse. However, the biggest problem to overcome is the issue of multiple solutions, particularly because, as the results obtained using IPSO show, different candidate solutions can produce very similar model error. Deviations of some parameters can be explained with limited identifiability, but in other cases discrepancies may still be a result of multiple optima attracting the estimation methods.

5. Conclusions and Future Work

5.1. Conclusions

This thesis focused on two topics: firstly, the simultaneous estimation of frequency and power components and secondly, the estimation of the parameters of dynamic load models. In both cases a new method has been applied and the results have been compared against traditional techniques in a number of tests based on computer simulations as well as measurements.

Through a literature review it has been identified that the estimation of the parameters of a sinusoidal signal is still a challenging task, especially in the presence of harmonic distortion and/or noise. Sensitivity to frequency deviations can be an issue, especially in the case of Fast Fourier Transform based methods. Additionally, methods based on signal filtering operate using a sliding data-window approach, which introduces delays and may possibly smooth some of the signal dynamics. In an attempt to overcome these issues a recursive approach has been proposed in this thesis. The Unscented Kalman Filter allows the tracking of the parameters of a nonlinear (dynamic) system without the necessity of calculating partial derivatives. To apply the method to the estimation of frequency and power components a simple state-space model of the instantaneous power signal has been proposed.

The results proved that the UKF demonstrate very good performance. First of all, the method is virtually insensitive to frequency deviations when estimating the power components. Secondly, due to the filtering properties of the UKF, sensitivity to noise is very small, which has been confirmed through a comparison with the Cramer-Rao Lower Bound. Whilst sensitivity to harmonic distortion is acceptable, it should be recognised that this feature can be strongly improved by extending the model to include selected harmonic components. Finally, the analysis of the computational burden showed that it should be possible to run the algorithm in real time, e.g. in a Phasor Measurement Unit or other monitoring device.

In the second part of this thesis a new technique, called Improved Particle Swarm Optimization, has been introduced to the task of estimating the parameters of dynamic load models. The method has been tested using two load models of different complexity and the results have been compared against traditional techniques. Additionally, the reliability of all of the methods has been investigated, because this feature has not been well documented in the literature devoted to load modelling so far.

In the case of the Exponential Recovery Load model, the proposed method showed very good performance in terms of accuracy and reliability. The results obtained in every set of the 100 trials were very consistent, as demonstrated by IPSO having the smallest standard deviation of the model error in the majority of cases. The traditional methods, Nonlinear Least Squares and Genetic Algorithms, suffered from convergence to a local minimum or premature convergence in several cases.

As expected, the estimation of the parameters of the Composite Load model has been most challenging. Its complexity proved to be too high for traditional methods, the accuracy of which has been very inconsistent in the set of 100 trials. The minimum model error achieved by both NLS and GA was acceptable. However, the probability of reaching it was rather small. The Hybrid approach offered a slight improvement in accuracy over that obtained by GA, but only within the local minimum already found by the latter. In this regard IPSO outperformed these methods by demonstrating much better reliability and accuracy, the performance of IPSO was very similar to that of the best trials of the NLS. This proved that IPSO is most suitable for the task of estimating the parameters of both types of load models. However, despite IPSO providing very consistent and accurate curve fitting, in the case of the CL model the estimated parameters tended to vary from run to run. It has been identified, through trajectory sensitivity analysis that, to at least some extent, this fact can be attributed to the limited identifiability of the model's parameters. Otherwise, the problem may be caused by the existence of multiple solutions that produce very similar model error. This issue is most difficult to overcome, and none of the tested methods can guarantee convergence to the global minimum. Some suggestions in this regard are given in the next section.

In terms of computational burden IPSO shows performance comparable to GA and the Hybrid technique, where most of the CPU resources are used for the multiple assessment of the fitness function. The NLS method, due to its deterministic nature, is the fastest. However, speed is not the key issue here, provided that the application does not involve the real-time response of the algorithm. In the case of load modelling it would be rather important to build a database of load parameters, which could be used later in online and offline applications. Such a database could be updated online, given that a monitoring device is providing measurements of voltage and power components.

5.2. Future work

This thesis investigated several aspects of the estimation of frequency and power components as well as the estimation of the parameters of dynamic load models, but it certainly did not exhaust either of these topics. There are still some challenges which need to be faced and this section provides some suggestions for the possible future avenues of research in this area.

The application of the UKF is intended to work in real-time and this means that the execution time will play a crucial role. For this reason the existing implementation of the algorithm should be revised and possibly optimized purely from the programming point of view. Ideally, the routine should be implemented in a relay, monitoring device or any other DSP unit with similar capabilities. This would allow the CPU resources necessary to run the UKF to be assessed accurately and finally prove the possibility of practical application of the method. Furthermore, an extended version of the instantaneous power signal model should be tested in a similar way. Inclusion of higher harmonics in the model will increase the accuracy of estimation when the measurements are heavily distorted, but at the cost of increased execution speed. An optimal solution should be found to meet the desired sampling rate without exceeding the available CPU resources.

Some issues have also been identified regarding the estimation of parameters of dynamic load models. First of all, the presented estimation methods should be tested against the real-data measurements of loads with a significant contribution of induction motors. Estimation of the parameters of the Exponential Recovery Load model has shown that the system measurements introduce additional uncertainty, which is difficult to include in a simulation. It has been proven to be more difficult to find the global minimum in such cases. This means that a similar situation should be expected when the Composite Load model is used. With a shorter timescale the impact of spontaneous load changes should be smaller; however, it should still be confirmed with real-data. Such recordings will require higher sampling frequency to capture the dynamic motor behaviour. Otherwise it will appear as if the demand consists purely of static load.

Another important factor that may affect the estimation results is the selection of the measurement data length. Data windows of different lengths will yield different results, an issue observed in [29]. This topic should be explored to find the optimal size of the data window. Such an approach should maximize the accuracy of the estimated parameters and minimize the impact of the spontaneous load variations. This should offer a particularly large increase in the accuracy of the static exponent and the time constant of the ERL model.

However, the biggest challenge is still the high complexity of the CL model. Nonlinearity, a high number of parameters and the vast searching space are the main sources of difficulties faced by the estimation methods. In this regard, there are several possible approaches that could be explored in the future.

Firstly, the number of local minima of the problem should be decreased by using more than one measurement in a single estimation process. However, in practice such training data should be gathered in a very short period of time to avoid considerable fluctuations of the load parameters and it is important that this data captures more than one steady-state of the observed load's response.

Secondly, it should be investigated whether it is possible (and beneficial) to analytically eliminate the two static exponents, that describe the static part of the

model, from the vector of unknown parameters and by doing so decrease the dimension of the problem. Theoretically, having measurements of two different steady-states, for a given set of parameters of the motor equivalent and the parameter K_p that quantifies the contribution of the motor to the total active power consumption, should make it possible to calculate the corresponding exponents of the static model. In practice, if such accurate measurements are not available, it should at least allow a more efficient initial population to be produced, where individuals with unrealistic combinations of parameters would be eliminated.

Finally, additional modifications of the estimation algorithms should be considered. In this project it has been identified that IPSO is a very good candidate for further development as a reliable and accurate method for the estimation of load model parameters. Currently, the algorithm is using only one thread during its progression. This means that at each step one individual is identified as the strongest and the rest of the population is following. It could be beneficial to modify the method and introduce a parallel approach in which the initial population would be divided into subgroups, possibly based on some clustering algorithms. Then, the estimation method would run several threads, one for each subgroup. The link between individuals inside a subgroup would be strong and the link to those outside that group should be much weaker. This could allow a more thorough exploration of the searching space, without attracting all of the individuals to one optimum too quickly. Additionally, a vast searching space could be divided into smaller subspaces, which could be explored separately.

5.3. Thesis Summary

The aim of this work was to improve the accuracy and reliability of power system analysis, with a particular consideration of Voltage Stability. This has been achieved through investigating the existing approaches to estimation of parameters of dynamic load models as well as estimation of frequency and power components and proposing alternative methods.

It has been shown, through a number of experiments, that the Unscented Kalman Filter can be used as a very efficient estimator of signal parameters. Virtually insensitive to frequency deviations, it proves to be very suitable for power system applications. Estimated parameters show to have a good correlation even with methods which are taking into account higher harmonics in their signal models (Self-Tuning Least Squares). Additionally, the recursive nature of the algorithm allows real-time implementation without the delay introduced by the sliding-window approaches.

In the second part it has been proved that the application of Improved Particle Swarm Optimization to the estimation of parameters of dynamic load models can increase the accuracy of the final result. Statistical analysis of the results also showed a significant increase of the reliability of estimation when compared to the traditional methods. This holds true for both the simple Exponential Recovery Load model and more complex Composite Load model.

6. References

[1] P. Kundur, *Power System Stability and Control*, McGraw-Hill, 1994

[2] D. Novosel, K. Vu, V. Centeno, S. Skok, M. Begovic, "Benefits of Synchronized-Measurement Technology for Power-Grid Applications", System Sciences, 2007. HICSS 2007. 40th Annual Hawaii International Conference on, January 2007

[3] T. Van Cutsem, C. Vournas, *Voltage Stability of Electrical Power System*, Kluwer Academic Publishers, 1998

[4] A. Borghetti, R. Caldon, C. A. Nucci, "Generic Dynamic Load Models in Long-Term Voltage Stability Studies", International Journal of Electrical Power & Energy System, vol. 22, no. 4, 2000

[5] M. M. Begovic, R. Q. Mills, "Load Identification and Voltage Stability Monitoring", Power Systems, IEEE Transactions on, vol. 10, no. 1, 109-116, Feb. 1995

[6] W. Xu, E. Vaahedi, Y. Mansour, J. Tamby, "Voltage Stability Load Parameter Determination from Field Tests on BC Hydro's System", Power Systems, IEEE Transactions on, vol. 12, no. 3, pp. 1290-1297, 1997

[7] D. J. Hill, "Nonlinear Dynamic Load Models with Recovery for Voltage Stability Studies", Power Systems, IEEE Transactions on, vol. 8, no. 1, pp. 166-176, 1993

[8] D. Chen, R. R. Mohler, "Neural-Network-Based Load Modeling and Its Use in Voltage Stability Analysis", Control Systems Technology, IEEE Transactions on, vol. 11, no. 4, pp. 460-470, 2003

[9] W. Xu, Y. Mansour, "Voltage Stability Analysis using Generic Dynamic Load Models", Power Systems, IEEE Transactions on, vol. 9, no. 1, pp. 479-493, 1994

[10] S.-H. Li, H.-D. Chiang, S. Liu, "Analysis of Composite Load Models on Load Margin of Voltage Stability", Power System Technology, 2006. PowerCon 2006. International Conference on, pp. 1-7, Oct. 2006

[11] S. Z. Zhu, J. H. Zheng, S. D. Shen, G. M. Luo, "Effect of Load Modeling on Voltage Stability", Power Engineering Society Summer Meeting, 2000. IEEE, vol. 1, pp. 395-400, July 2000

[12] K. Morison, H. Hamadani, L. Wang, "Load Modeling for Voltage Stability Studies", Power Systems Conference and Exposition, 2006. PSCE '06. 2006 IEEE PES, pp. 564-568, Oct. 2006

[13] Y. G. Zeng, G. Berizzi, P. Marannino, "Voltage Stability Analysis Considering Dynamic Load Model", Advances in Power System Control, Operation and Management, 1997. APSCOM-97. Fourth International Conference on, vol. 1, pp. 396-401, Nov. 1997

[14] R. M. Rifaat, "On Composite Load Modeling for Voltage Stability and Under Voltage Load Shedding", Power Engineering Society General Meeting, 2004. IEEE, vol. 2, pp. 1603-1610, June 2004

[15] T. Aboul-Seoud, J. Jatskevich, "Dynamic Modeling of Induction Motor Loads for Transient Voltage Stability Studies", Electric Power Conference, 2008. EPEC 2008. IEEE, pp. 1-5, Oct. 2008

[16] W.-S. Kao, C.-T. Huang, C.-Y. Chiou, "Dynamic Load Modeling in Taipower System Stability Studies", Power Systems, IEEE Transactions on, vol. 10, no. 2, pp. 907-914, 1995

[17] P. Ju, F. Wu, Z.-Y. Shao, X.-P. Zhang, H.-J. Fu, P.-F. Zhang, N.-Q. He, J.-D. Han, "Composite Load Models Based on Field Measurements and Their Application in Dynamic Analysis", Generation, Transmission & Distribution, IET, vol. 1, no. 5, pp. 724-730, Sept. 2007

[18] Y. Li, H.-D. Chiang, B.-K. Choi, Y.-T. Chen, D.-H. Huang, M. G. Lauby, "Representative Static Load Models for Transient Stability Analysis: Development and Examination", Generation, Transmission & Distribution, IET, vol. 1, no. 3, pp. 422-431, May 2007

[19] Q. Ai; D. Gu; C. Chen, "New Load Modeling Approaches Based on Field Tests for Fast Transient Stability Calculations", Power Systems, IEEE Transactions on, vol. 21, no. 4, pp. 1864-1873, Nov. 2006

[20] J.Y. Wen, L. Jiang, Q.H. Wu, S.J. Cheng, "Power System Load Modeling by Learning Based on System Measurements", Power Delivery, IEEE Transactions on, vol. 18, no. 2, pp. 364 – 371, April 2003

[21] J. Ma, Z.-Y. Dong, R. He, D.J. Hill, **"**Measurement-based Load Modeling using Genetic Algorithms", Evolutionary Computation, 2007. CEC 2007. IEEE Congress on, pp. 2909 – 2916, 25-28 Sept. 2007

[22] W.-H. Xu, C. Chen, Q. Ai, W. Wang, X.-B. Ling, B. Liu, Chong Wang, "Load Modeling During Asymmetric Disturbance in a Metropolitan Power Grid", Power Systems, IEEE Transactions on, vol. 24, no. 3, pp. 1191-1198, Aug. 2009

[23] H. Bai, P. Zhang, V. Ajjarapu, "A Novel Parameter Identification Approach via Hybrid Learning for Aggregate Load Modeling", Power Systems, IEEE Transactions on, vol. 24, no. 3, August 2009

[24] R. He, J. Ma, Member, IEEE, and D. J. Hill, Fellow, IEEE, "Composite Load Modeling via Measurement Approach", Power Systems, IEEE Transactions on, vol. 21, no. 2, May 2006

[25] J. Ma, D. Han, R. He, Z.-Y. Dong, D.J. Hill, **"**Reducing Identified Parameters of Measurement-Based Composite Load Model", Power Systems, IEEE Transactions on, vol. 23, no. 1, pp. 76 – 83, Feb. 2008

[26] D. Han, J. Ma, R. He, Z.-Y. Dong, "A Real Application of Measurement-Based Load Modeling in Large-Scale Power Grids and its Validation", Power Systems, IEEE Transactions on, vol. 24, no. 4, pp. 1756-1764, Nov. 2009

[27] J. Ma, R. He, D. J. Hill, "Load modeling by finding support vectors of load data from field measurements", Power Systems, IEEE Transactions on, vol. 21, no. 2, pp. 726-735, May 2006

[28] D. Karlsson, D.J. Hill, "Modelling and Identification of Nonlinear Dynamic Loads in Power Systems", Power Systems, IEEE Transactions on, vol. 9, no. 1, pp. 157-166, 1994

[29] Dobrivoje P. Stojanović, Lidija M. Korunović, J. V. Milanović, "Dynamic load modelling based on measurements in medium voltage distribution network", Electric Power Systems Research, vol. 78, no. 2, pp. 228-238, Feb. 2008

[30] L. M. Korunović, D. P. Stojanović, J. V. Milanović, "Identification of Static Load Characteristics Based on Measurements in Medium-Voltage Distribution Network", IET Generation, Transmission & Distribution, vol. 2, no. 2, pp. 227-234, March 2008

[31] B.-K. Choi, H.-D. Chiang, Y. Li, H. Li, Y.-T. Chen, D.-. Huang, M.G. Lauby, "Measurement-based dynamic load models: derivation, comparison, and

validation", Power Systems, IEEE Transactions on, vol. 21, no. 3, pp. 1276 – 1283, Aug. 2006

[32] J.-C. Wang, H.-D. Chiang, C.-L. Chang, A.-H. Liu, C.-H. Huang, C.-Y. Huang, "Development of a frequency-dependent composite load model using the measurement approach", Power Systems, IEEE Transactions on, vol. 9, no. 3, pp. 1546-1556, Aug. 1994

[33] C.-J. Lin, A.Y.-T. Chen, C.-Y. Chiou, C.-H. Huang, H.-D. Chiang, J.-C. Wang, L. Fekih-Ahmed, "Dynamic load models in power systems using the measurement approach", Power Systems, IEEE Transactions on, vol. 8, no. 1, pp. 309-315, Feb. 1993

[34] Y. Xu, R. He, D. Han, "Validation of measurement-based load modeling for large-scale power grid", Power and Energy Society General Meeting - Conversion and Delivery of Electrical Energy in the 21st Century, 2008 IEEE, pp. 1-6, 20-24 July 2008

[35] J. H. Shi, R. He, "Measurements-based load modeling – model structure", Power Tech Conference Proceedings, 2003 IEEE Bologna, vol. 2, 23-26 June 2003

[36] D. Han, R. He, Y. Xu, J. Ma, "Measurement-based Load Modeling Validation by Artificial Three-phase Short Circuit Tests in North East Power Grid", Power Engineering Society General Meeting, 2007. IEEE, pp. 1-6, 24-28 June 2007

[37] A. Maitra, A. Gaikwad, P. Pourbeik, D. Brooks, "Load model parameter derivation using an automated algorithm and measured data", Power and Energy Society General Meeting - Conversion and Delivery of Electrical Energy in the 21st Century, 2008 IEEE, pp. 1-7, 20-24 July 2008

[38] F. T. Dai, J. V. Milanovic, N. Jenkins, V. Roberts, "The influence of voltage variations on estimated load parameters", Electricity Distribution, 2001. Part 1: Contributions. CIRED. 16th International Conference and Exhibition on, vol. 2, 18-21 June 2001

[39] B.-K. Choi, H.-D. Chiang, Y. Li, Y.-T. Chen, D.-H. Huang, M. G. Lauby, "Development of composite load models of power systems using on-line measurement data", Power Engineering Society General Meeting, 2006. IEEE

[40] A. Maitra, A. Gaikwad, P. Zhang, M. Ingram, D. L. Mercado, W. D. Woitt, "Using System Disturbance Measurement Data to Develop Improved Load

Models", Power Systems Conference and Exposition, 2006. PSCE '06. 2006 IEEE PES, pp. 1978-1985, Oct. 2006

[41] K. Yamashita, M. Asada, K. Yoshimura, "A development of dynamic load model parameter derivation method", Power & Energy Society General Meeting, 2009. PES '09. IEEE, 26-30 July 2009

[42] V. Terzija, G. Valverde, D. Cai, P. Regulski, V. Madani, J. Fitch, S. Skok, M.M. Begovic, A. Phadke, "Wide-Area Monitoring, Protection and Control of Future Electric Power Networks", Proceedings of IEEE, vol. 99, no. 1, pp. 88-93, 2011

[43] S.Chakrabarti, E.Kyriakides, Bi Tianshu, C.Deyu and V.Terzija, "Measurements get together", IEEE Power and Energy Magazine, vol. 7, no. 1, pp. 41-49, January-February 2009

[44] F. Wang, M. Bollen, "Frequency response characteristics and error estimation in RMS measurement", Power Delivery, IEEE Transactions on, vol. 19, no. 4, 1569-1578, Oct. 2004

[45] M. Wang, Y. Sun, "A practical, precise method for frequency tracking and phasor estimation", Power Delivery, IEEE Transactions on, vol. 9, no. 4, pp. 1547-1552, Oct. 2004

[46] L. Wang, "Frequency response of phasor-based microprocessor relaying algorithms", Power Delivery, IEEE Transactions on, vol. 14, no. 1, pp. 98-109, Jan. 1999

[47] M. S. Sachdev, M. Nagpal, "A recursive least error squares algorithm for power system relaying and measurement application", Power Delivery, IEEE Transactions on, vol. 6, no. 3, pp. 1008-1015, July 1991

[48] A. A. Girgis, W. L. Peterson, "Adaptive estimation of power system frequency deviation and its rate of change for calculating sudden power system overloads", Power Delivery, IEEE Transactions on, vol. 5, no. 2, pp.585–594, Apr. 1990

[49] V.K. Jain, W.L. Collins, D.C. Davis, "High-Accuracy Analog Measurements via Interpolated FFT", Instrumentation and Measurements, IEEE Transactions on, vol. 28, no. 2, pp. 113-122, 1979

[50] D. Agrez, "Weighted multipoint interpolated DFT to improve amplitude estimation of multifrequency signal", Instrumentation and Measurements, IEEE Transactions on, vol. 51, no. 2, pp. 287-292, 2002

[51] V. V. Terzija, M. B. Djuric, B. Kovacevic, "Voltage phasor and local system frequency estimation using Newton type algorithm", Power Delivery, IEEE Transactions on, vol. 9, no. 3, pp. 1358-1374, July 1994

[52] V. V. Terzija, V. Stanojevic, M. Popov, L. van der Sluis, "Digital metering of power components according to IEEE Standard 1459-2000 using the Newton-type algorithm", Instrumentation and Measurements, IEEE Transactions on, vol. 56, no. 6, pp. 2717-2724, Dec. 2007

[53] R.Chudamani, K.Vasudevan, C.S.Ramalingam, "Real-Time Estimation of Power System Frequency Using Nonlinear Least Squares", IEEE Trans. on Power Delivery, Volume: 24, Issue: 3, July 2009 pp.1021-1028

[54] M. D. Kusljevic, "A Simple Recursive Algorithm for Frequency Estimation", Instrumentation and Measurements, IEEE Transactions on, vol. 53, no. 2, 335-340, April 2004

[55] M. D. Kusljevic, "A Simple Recursive Algorithm for Simultaneous Magnitude and Frequency Estimation", Instrumentation and Measurements, IEEE Transactions on, vol. 57, no. 6, 1207-1214, June 2008

[56] M. D. Kusljevic, "Adaptive resonator-based method for power system harmonic analysis", Science, Measurement and Technology, IET, vol. 2, no. 3, pp. 177-185, 2008

[57] J.J.Tomic, M.D.Kusljevic, D.P.Marcetic,' An Adaptive Resonator-Based Method for Power Measurements According to the IEEE Trial-Use Standard 1459–2000',IEEE Transactions on Instrumentation and Measurement, vol. 59, no. 2, pp.250-258, Feb. 2010

[58] M.D.Kusljević, 'A Simultaneous Estimation of Frequency, Magnitude, and Active and Reactive Power by Using Decoupled Modules', IEEE Transactions on Instrumentation and Measurement, vol. 59 , no. 7, pp.1866-1873, July 2010

[59] M.D.Kusljevic, J.J.Tomic, L.D.ovanovic, 'Frequency Estimation of Three-Phase Power System Using Weighted-Least-Square Algorithm and Adaptive FIR Filtering', IEEE Transactions on Instrumentation and Measurement, vol. 59 , no. 9, pp.322-329, Feb. 2010

[60] W. Rebizant, J. Szafran, A. Wiszniewski, *Digital Signal Processing in Power System Protection and Control*, Springer, 2011

[61] DIgSILENT, "DIgSILENT PowerFactory," 15.0.525.1. Gomaringen/ Germany, ©1986-2011

[62] IEEE Standard C37.111-1999, IEEE Standard for Transient Data Exchange (COMTRADE) for Power Systems, 1991

[63] Mathworks, "Mathworks MATLAB®", 7.12.0.635 (R2011a). ©1994-2008. USA. The MathWorks, Inc.

[64] A. A. Girgis, F. M. Ham, "A qualitative study of pitfalls in FFT," IEEE Trans. Aerosp. Electron. Syst., vol. AES-16, pp. 434–439, July 1980

[65] V.Terzija, M.Djurić, B.Kovačević, "A New Self-Tuning Algorithm for the Frequency Estimation of Distorted Signals", IEEE Trans. on Power Delivery, vol.10, no.4, pp 1779-1785, Oct. 1995

[66] V.Terzija, V.Stanojevic "STLS Algorithm for Power-Quality Indices Estimation", IEEE Trans. on Power Delivery, vol. 23, no. 2, pp. 544 – 552, April 2008

[67] J. Reddy, P. K. Dash, R. Samantaray,A. K. Moharana, „Fast Tracking of Power Quality Disturbance Signals Using an Optimized Unscented Filter", IEEE Transactions on Instrumentation and Measurement, vol. 58, no. 12, pp. 3943-3952, 2009

[68] G.Valverde, V.Terzija, "Unscented Kalman Filter for Power System Dynamic State Estimation", IET Generation, Transmission and Distribution, vol. 5, no. 1, pp. 29-37, 2010

[69] V. Terzija, D. Cai, V. Stanojević, G. Strbac, „Frequency and Power Components Estimation from Instantaneous Power Signal", Instrumentation and Measurements, IEEE Transactions on, vol. 60, no. 11, pp. 3640-3649, 2011

[70] Z.Jian, A.Swain, N.K.C.Nair, and J.J.Liu, "Estimation of power quality using an unscented Kalman filter," in TENCON 2007 - 2007 IEEE Region 10 Conference, 2007

[71] S. J. Julier, J. K. Uhlmann, H. F. Durrant-Whyte, A New Approach for Filtering Nonlinear Systems, American Control Conference, 1995. Proceedings of the, vol. 3, pp. 1628-1632, 21-23 June 1995

[72] S.J.Julier and J. K. Uhlmann, "Unscented filtering and nonlinear estimation", Proceedings of the IEEE, Volume 92, pp. 401-422, 2004

[73] E.A.Wan, R. Van Der Merwe, "The unscented Kalman filter for nonlinear estimation", Adaptive Systems for Signal Processing, Communications, and Control Symposium 2000. AS-SPCC. The IEEE, pp. 153-158, 2000

[74] M.Lei, B.J. van Wyk, Y.Qi, "Online Estimation of the Approximate Posterior Cramer-Rao Lower Bound for Discrete-Time Nonlinear Filtering", Aerospace and Electronic Systems, IEEE Transactions on, vol. 47, no. 1, 2011

[75] IMC-μ-Musycs, http://www.imc-berlin.de/en/messtechnik/

[76] "Multifunction Protection and Switchgear Control Unit REF542*plus*, Operator's Manual" 1VTA100172-Rev 4, ABB - PTMV, 04.04.2005

[77] Definitions for the Measurement of Electric Quantities Under Sinusoidal, Nonsinusoidal, Balanced, or Unbalanced Conditions, IEEE Std. 1459-2000, Jan. 2000

[78] J.L.Willems, J.A.Ghijseln, A.E.Emanuel, "The Apparent Power Concept and the IEEE Standard 1459-2000", IEEE Transactions On Power Delivery, vol. 11, no. 1, pp.73-78, Jan. 1996

[79] B.-K. Choi, H.-D. Chiang, "Multiple Solutions and Plateau Phenomenon in Measurement-Based Load Model Development: Issues and Suggestions", Power Systems, IEEE Transactions on, vol. 24, no. 2, pp. 824-831, May 2009

[80] J.-B. Park, Y.-W. Jeong, J.-R. Shin, K. Y. Lee, "An Improved Particle Swarm Optimization for Nonconvex Economic Dispatch Problems", Power Systems, IEEE Transactions on, vol. 25, no. 1, pp. 156-166, 2010

[81] C. Guangyi, G.Wei, H. Kaisheng, "On Line Parameter Identification of an Induction Motor Using Improved Particle Swarm Optimization", Proceedings of the 26th Chinese Control Conference, 26-31 July 2007

[82] W. Liu, M. Li, X. Wang, "An Improved Particle Swarm Optimization Algorithm for Optimal Power Flow", Power Electronics and Motion Control Conference, 2009. IEEE 6th International, pp. 2448-2450, 17-20 May 2009

[83] F. Yang, X. Zi-Li, H. Rong, C. Jia-Lin, "A Heuristic Particle Swarm Optimization and its Application in Power Network Planning", Intelligent Network and Intelligent Systems, 2008. First International Workshop on, pp. 107-110, 1-3 Nov. 2008

[84] K. Madsen, H.B. Nielsen, O. Tingleff, *Methods for Non-linear Least Squares Problems*, 2nd Edition, Technical University of Denmark, 2004

[85] Randy L. Haupt, Sue Ellen Haupt, Practical Genetic Algorithms, Second Edition, John Wiley & Sons, 2004

[86] M. Mitchell, An Introduction to Genetic Algorithms, MIT, 1998

[87] R. C. Eberhart, J. Kennedy, "A New Optimizer Using Particle Swarm Theory", Micro Machine and Human Science, 1995. Proceedings of the Sixth International Symposium on, pp. 39-43, 4-6 Oct. 1995

[88] J. Kennedy, R. C. Eberhart, "Particle Swarm Optimization, Neural Networks", 1995. Proceedings of IEE International Conference on, vol. 4, pp. 1942-1948, 27 Nov.-1 Dec. 1995

[89] R. C. Eberhart, Y. Shi, "Particle Swarm Optimization: Developments, Applications and Resources", Evolutionary Computation, 2001. Proceedings of the 2001 Congress on, vol. 1, pp. 81-86, 27-30 May, 2001

[90] M. Clerc, *Particle Swarm Optimization*, ISTE Ltd., 2006

[91] R. Caponetto, L. Fortuna, S. Fazzino, M. G. Xibilia, "Chaotic Sequences to Improve the Performance of Evolutionary Algorithms", Evolutionary Computation, IEEE Transactions on, vol. 7, no. 3, pp. 289-304, 2003

[92] M. A. Pai, *Energy Function Analysis for Power System Stability*, Norwell, MA: Kluwer, 1989

[93] IEEE Task Force, "Standard Load Models for Power Flow and Dynamic Performance Simulation", *Power Systems, IEEE Transactions on*, vol. 10, no. 3, pp. 1302-1313, 1995

[94] I. A. Hiskens, M. A. Pai, "Trajectory Sensitivity Analysis of Hybrid Systems – Part I: Fundamental Theory and Applications". *Circuit Systems, IEEE Transactions on*, vol. 47, no. 2, pp. 204-220, 1997

[95] I. A. Hiskens, "Nonlinear Dynamic Model Evaluation from Disturbance Measurements", Power Systems, IEEE Transactions on, vol. 16, no. 4, pp. 702-710, 2001

7. Appendices

7.1. Appendix A

7.1.1. A-1: 10-bus Test System Parameters and Data

Table 7-1: Line and transformer data (rated to 100MVA)

From	To	R [pu]	X [pu]	B [pu]	Ratio
4	5	0.0000	0.0040	0.0000	-
4	6	0.0015	0.0288	1.1730	-
8	9	0.0010	0.0030	0.0000	-
1	4	0.0000	0.0020	0.0000	0.8857
2	5	0.0000	0.0045	0.0000	0.8857
3	6	0.0000	0.0125	0.0000	0.9024
6	7	0.0000	0.0030	0.0000	1.0664
6	8	0.0000	0.0026	0.0000	1.0800
9	10	0.0000	0.0010	0.0000	0.9750

Table 7-2: Generation, loads and compensation data

		Generation	Load		Compensation
Bus	V [pu]	P [MW]	P [MW]	Q [Mvar]	Q [Mvar]
1	0.98	3981	-	-	-
2	0.9646	1736	-	-	-
3	1.04	1154	-	-	-
6	-	-	-	-	763
7	-	-	3271	1015	600
8	-	-	-	-	1710
10	-	-	3384	971	-

Table 7-3: Parameters of generators (on respective MVA rating)

Bus	H	MVA Rating	Ra	Xd	Xq	Xl	Xd'	Xq'	Xd''	Xq''	Td0'	Tq0'	Td0''	Tq0''
1	Infinite	-	-	-	-	-	-	-	-	-	-	-	-	-
2	2.09	2200	0.0046	2.07	1.99	0.155	0.28	0.49	0.215	0.215	4.1	0.56	0.033	0.062
3	2.33	1400	0.0046	2.07	1.99	0.155	0.28	0.49	0.215	0.215	4.1	0.56	0.033	0.062

7.1.2. A-2: 10-bus Test System Controllers

Both generators 2 and 3 have the same AVR systems (Figure 7-1) with the K_A = 400, T_R = 0.02, E_{FMAX} = 10 and E_{FMIN} = -10.

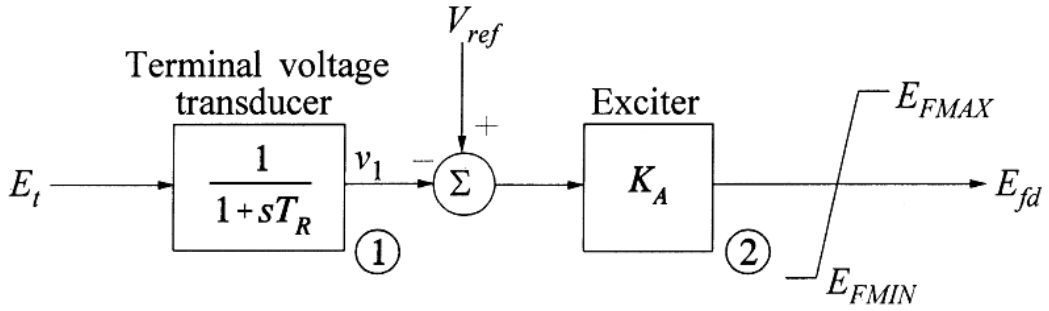

Figure 7-1: Block diagram of the AVR system [1]

OXL (Figure 7-2) is only installed at generator 3 and it has the following parameters: I_{fdmax1} = 3.02pu, I_{fdmax2} = 4.60pu, I_{LIM} = 3.85pu, K_1 = 0.248 and K_2 = 12.6.

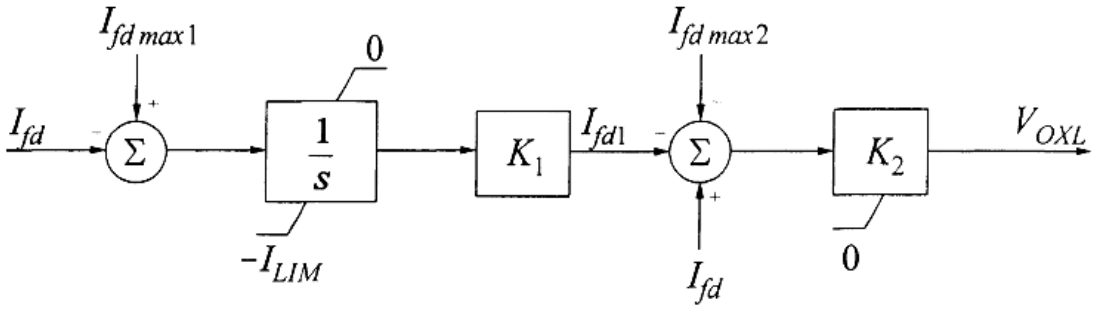

Figure 7-2: Block diagram of the OXL system [1]

7.2. Appendix B

7.2.1. B-1: IEEE 39-bus Test System Parameters and Data

Table 7-4: Line and transformer data (rated to 100MVA)

From	To	R	X	B	Ratio	From	To	R	X	B	Ratio
1	2	0.0035	0.0411	0.6987	0	16	24	0.0003	0.0059	0.068	0
1	39	0.001	0.025	0.75	0	17	18	0.0007	0.0082	0.1319	0
2	3	0.0013	0.0151	0.2572	0	17	27	0.0013	0.0173	0.3216	0
2	25	0.007	0.0086	0.146	0	21	22	0.0008	0.014	0.2565	0
3	4	0.0013	0.0213	0.2214	0	22	23	0.0006	0.0096	0.1846	0
3	18	0.0011	0.0133	0.2138	0	23	24	0.0022	0.035	0.361	0
4	5	0.0008	0.0128	0.1342	0	25	26	0.0032	0.0323	0.513	0
4	14	0.0008	0.0129	0.1382	0	26	27	0.0014	0.0147	0.2396	0
5	6	0.0002	0.0026	0.0434	0	26	28	0.0043	0.0474	0.7802	0
5	8	0.0008	0.0112	0.1476	0	26	29	0.0057	0.0625	1.029	0
6	7	0.0006	0.0092	0.113	0	28	29	0.0014	0.0151	0.249	0
6	11	0.0007	0.0082	0.1389	0	12	11	0.0016	0.0435	0	1.006
7	8	0.0004	0.0046	0.078	0	12	13	0.0016	0.0435	0	1.006
8	9	0.0023	0.0363	0.3804	0	6	31	0	0.025	0	1.07
9	39	0.001	0.025	1.2	0	10	32	0	0.02	0	1.07

10	11	0.0004	0.0043	0.0729	0	19	33	0.0007	0.0142	0	1.07
10	13	0.0004	0.0043	0.0729	0	20	34	0.0009	0.018	0	1.009
13	14	0.0009	0.0101	0.1723	0	22	35	0	0.0143	0	1.025
14	15	0.0018	0.0217	0.366	0	23	36	0.0005	0.0272	0	1
15	16	0.0009	0.0094	0.171	0	25	37	0.0006	0.0232	0	1.025
16	17	0.0007	0.0089	0.1342	0	2	30	0	0.0181	0	1.025
16	19	0.0016	0.0195	0.304	0	29	38	0.0008	0.0156	0	1.025
16	21	0.0008	0.0135	0.2548	0	19	20	0.0007	0.0138	0	1.06

Table 7-5: Generation and Load Data

Bus	Type	Voltage [PU]	Load		Generation		
			MW	MVar	MW	MVar	Unit No.
1	PQ	-	0	0	0	0	
2	PQ	-	0	0	0	0	
3	PQ	-	322	2.4	0	0	
4	PQ	-	500	184	0	0	
5	PQ	-	0	0	0	0	
6	PQ	-	0	0	0	0	
7	PQ	-	233.8	84	0	0	
8	PQ	-	522	176	0	0	
9	PQ	-	0	0	0	0	
10	PQ	-	0	0	0	0	
11	PQ	-	0	0	0	0	
12	PQ	-	7.5	88	0	0	
13	PQ	-	0	0	0	0	
14	PQ	-	0	0	0	0	
15	PQ	-	320	153	0	0	
16	PQ	-	329	32.3	0	0	
17	PQ	-	0	0	0	0	
18	PQ	-	158	30	0	0	
19	PQ	-	0	0	0	0	
20	PQ	-	628	103	0	0	
21	PQ	-	274	115	0	0	
22	PQ	-	0	0	0	0	
23	PQ	-	247.5	84.6	0	0	
24	PQ	-	308.6	-92	0	0	
25	PQ	-	224	47.2	0	0	
26	PQ	-	139	17	0	0	
27	PQ	-	281	75.5	0	0	
28	PQ	-	206	27.6	0	0	
29	PQ	-	283.5	26.9	0	0	
30	PV	1.0475	0	0	250	-	Gen10
31	PV	0.982	9.2	4.6	-	-	Gen2
32	PV	0.9831	0	0	650	-	Gen3
33	PV	0.9972	0	0	632	-	Gen4
34	PV	1.0123	0	0	508	-	Gen5
35	PV	1.0493	0	0	650	-	Gen6
36	PV	1.0635	0	0	560	-	Gen7
37	PV	1.0278	0	0	540	-	Gen8
38	PV	1.0265	0	0	830	-	Gen9
39	PV	1.03	1104	250	1000	-	Gen1

Table 7-6: Parameters of generators (on 1000 MVA rating)

Unit No.	H	Ra	X'd	X'q	Xd	Xq	T'do	T'qo	X1
1	50	0	0.06	0.08	0.2	0.19	7	0.7	0.3
2	3.03	0	0.697	1.7	2.95	2.82	6.56	1.5	3.5
3	3.58	0	0.531	0.876	2.495	2.37	5.7	1.5	3.04
4	2.86	0	0.436	1.66	2.62	2.58	5.69	1.5	2.95
5	2.6	0	1.32	1.66	6.7	6.2	5.4	0.44	5.4
6	3.48	0	0.5	0.814	2.54	2.41	7.3	0.4	2.24
7	2.64	0	0.49	1.86	2.95	2.92	5.66	1.5	3.22
8	2.43	0	0.57	0.911	2.9	2.8	6.7	0.41	2.8
9	3.45	0	0.57	0.587	2.106	2.05	4.79	1.96	2.98
10	4.2	0	0.31	0.08	1	0.69	10.2	0	1.25

7.2.2. B-2: IEEE 39-bus Test System Controllers

Table 7-7: Parameters of AVRs

Unit No.	TR	KA	TA	TB	TC	VREF	EfdMax	EfdMin
1	0.01	200	0.015	10	1	1.03	5	-5
2	0.01	200	0.015	10	1	0.982	5	-5
3	0.01	200	0.015	10	1	0.9831	5	-5
4	0.01	200	0.015	10	1	0.9972	5	-5
5	0.01	200	0.015	10	1	1.0123	5	-5
6	0.01	200	0.015	10	1	1.0493	5	-5
7	0.01	200	0.015	10	1	1.0635	5	-5
8	0.01	200	0.015	10	1	1.0278	5	-5
9	0.01	200	0.015	10	1	1.0265	5	-5
10	0.01	200	0.015	10	1	1.0475	5	-5

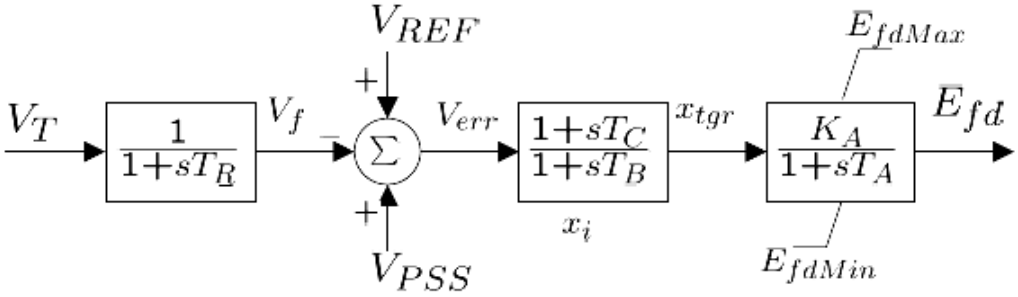

Figure 7-3: Block diagram of the AVR system

7.3. Appendix C

7.3.1. C-1: UKF Parameters

Q = *diag(***q**^{2}*)* and **R** = *diag(***r**^{2}*)*

Table 7-8: UKF parameters

Parameter	Value
α	0.001
β	2
κ	1

Table 7-9: Covariance matrices in different tests

Test	q	r
Static test (clean)	[10^{-6} 10^{-6} 10^{-6} 10^{-6}]	[10^{-6}]
Static test (noise I)	[10^{-6} 10^{-6} 10^{-6} 10^{-6}]	[$5*10^{-3}$]
Static test (noise II)		
15-45dB	[10^{-6} 10^{-6} 10^{-6} 10^{-6}]	[10^{-2}]
60-75dB		[10^{-3}]
Sensitivity to harmonics	[10^{-6} 10^{-6} 10^{-6} 10^{-6}]	see Table 7-10
Dynamic Test	[10^{-6} 10^{-6} 10^{-6} 10^{-6}]	[10^{-6}]
Laboratory Test	[10^{-4} $5*10^{-6}$ $3.5*10^{-3}$ $3.5*10^{-3}$]	[10^{-1}]

Table 7-10: Measurement covariance for Sensitivity to Higher Harmonics test

r		THDU [%]			
		0	7.071	14.142	28.284
THDI [%]	0	[10^{-4}]	[10^{-3}]	[10^{-3}]	[10^{-2}]
	14.142	[10^{-3}]	[10^{-3}]	[10^{-2}]	[10^{-2}]
	28.284	[10^{-2}]	[10^{-2}]	[10^{-2}]	[10^{-1}]

7.4. Appendix D

7.4.1. D-1: Matrices for Trajectory Sensitivity Analysis of the IM Model

$$x = \begin{bmatrix} v'_d \\ v'_q \\ \omega_r \end{bmatrix} \qquad y = \begin{bmatrix} i_d \\ i_q \\ P \\ Q \end{bmatrix}$$

$$f(x,y,p)=\begin{bmatrix} -\frac{1}{T'}(x_1+(X-X')y_2)-(x_3-1)x_2 \\ -\frac{1}{T'}(x_2-(X-X')y_1)+(x_3-1)x_1 \\ \frac{1}{2H}((x_1y_1+x_2y_2)-(Ax_3^2+Bx_3+C)T_0) \end{bmatrix}$$

$$g(x,y,p)=\begin{bmatrix} y_1-\frac{1}{R_s^2+X'^2}(R_s(v_d-x_1)-X'x_2) \\ y_2+\frac{1}{R_s^2+X'^2}(R_sx_2+X'(v_d-x_1)) \\ y_3-v_dy_1 \\ y_4+v_dy_2 \end{bmatrix}$$

$$\frac{\partial f}{\partial x}=\begin{bmatrix} -\frac{1}{T'} & -(x_3-1) & -x_2 \\ (x_3-1) & -\frac{1}{T'} & x_1 \\ \frac{y_1}{2H} & \frac{y_2}{2H} & -\frac{T_0}{2H}(2Ax_3+B) \end{bmatrix} \qquad \frac{\partial f}{\partial y}=\begin{bmatrix} 0 & -\frac{1}{T'}(X-X') & 0 & 0 \\ \frac{1}{T'}(X-X') & 0 & 0 & 0 \\ \frac{x_1}{2H} & \frac{x_2}{2H} & 0 & 0 \end{bmatrix}$$

$$\frac{\partial g}{\partial x}=\begin{bmatrix} \frac{1}{R_s^2+X'^2}R_s & \frac{1}{R_s^2+X'^2}X' & 0 \\ -\frac{1}{R_s^2+X'^2}X' & \frac{1}{R_s^2+X'^2}R_s & 0 \\ 0 & 0 & 0 \\ 0 & 0 & 0 \end{bmatrix} \qquad \frac{\partial g}{\partial y}=\begin{bmatrix} 1 & 0 & 0 & 0 \\ 0 & 1 & 0 & 0 \\ -v_d & 0 & 1 & 0 \\ 0 & v_d & 0 & 1 \end{bmatrix}$$

$$\frac{\partial f}{\partial H}=\begin{bmatrix} 0 & 0 & -\frac{1}{2H^2}((x_1y_1+x_2y_2)-(Ax_3^2+Bx_3+C)T_0) \end{bmatrix}^T$$

$$\frac{\partial f}{\partial R_s}=\frac{\partial f}{\partial X_s}=\begin{bmatrix} 0 & 0 & 0 \end{bmatrix}^T \qquad \frac{\partial f}{\partial R_r}=\begin{bmatrix} -\frac{x_1+(X-X')y_2}{X_r+X_m} & -\frac{x_2-(X-X')y_1}{X_r+X_m} & 0 \end{bmatrix}^T$$

$$\frac{\partial f}{\partial X_r}=\begin{bmatrix} \frac{R_rx_1}{(X_r+X_m)^2}-y_2\left(\frac{1}{T'}\left(\frac{X_mX_r}{(X_r+X_m)^2}-\frac{X_m}{X_r+X_m}\right)-\frac{R_r(X-X')}{(X_r+X_m)^2}\right) \\ \frac{R_rx_2}{(X_r+X_m)^2}+y_1\left(\frac{1}{T'}\left(\frac{X_mX_r}{(X_r+X_m)^2}-\frac{X_m}{X_r+X_m}\right)-\frac{R_r(X-X')}{(X_r+X_m)^2}\right) \\ 0 \end{bmatrix}$$

$$\frac{\partial f}{\partial X_m}=\begin{bmatrix} \dfrac{R_r x_1}{(X_r+X_m)^2}-y_2\left(\dfrac{1}{T'}\left(1+\dfrac{X_m X_r}{(X_r+X_m)^2}-\dfrac{X_r}{X_r+X_m}\right)-\dfrac{R_r(X-X')}{(X_r+X_m)^2}\right) \\ \dfrac{R_r x_2}{(X_r+X_m)^2}+y_1\left(\dfrac{1}{T'}\left(1+\dfrac{X_m X_r}{(X_r+X_m)^2}-\dfrac{X_r}{X_r+X_m}\right)-\dfrac{R_r(X-X')}{(X_r+X_m)^2}\right) \\ 0 \end{bmatrix}$$

$$\frac{\partial f}{\partial T_0}=\begin{bmatrix} 0 & 0 & -\dfrac{1}{2H}(Ax_3^2+Bx_3+C) \end{bmatrix}^T$$

$$\frac{\partial f}{\partial A}=\begin{bmatrix} 0 & 0 & -\dfrac{T_0}{2H}x_3^2 \end{bmatrix}^T \qquad \frac{\partial f}{\partial B}=\begin{bmatrix} 0 & 0 & -\dfrac{T_0}{2H}x_3 \end{bmatrix}^T$$

$$\frac{\partial g}{\partial H}=\begin{bmatrix} 0 & 0 & 0 & 0 \end{bmatrix}^T \quad \frac{\partial g}{\partial R_s}=\begin{bmatrix} -(v_d-x_1)\left(\dfrac{1}{R_s^2+X'^2}-\dfrac{2R_s^2}{(R_s^2+X'^2)^2}\right)-\dfrac{2R_s X' x_2}{(R_s^2+X'^2)^2} \\ x_2\left(\dfrac{1}{R_s^2+X'^2}-\dfrac{2R_s^2}{(R_s^2+X'^2)^2}\right)-(v_d-x_1)\dfrac{2R_s X'}{(R_s^2+X'^2)^2} \\ 0 \\ 0 \end{bmatrix}$$

$$\frac{\partial g}{\partial X_s}=\begin{bmatrix} (v_d-x_1)\dfrac{2R_s X'}{(R_s^2+X'^2)^2}+x_2\left(\dfrac{1}{R_s^2+X'^2}-\dfrac{2X'^2}{(R_s^2+X'^2)^2}\right) \\ -x_1\dfrac{2R_s X'}{(R_s^2+X'^2)^2}+(v_d-x_1)\left(\dfrac{1}{R_s^2+X'^2}-\dfrac{2X'^2}{(R_s^2+X'^2)^2}\right) \\ 0 \\ 0 \end{bmatrix} \quad \frac{\partial g}{\partial R_r}=\begin{bmatrix} 0 & 0 & 0 & 0 \end{bmatrix}^T$$

$$\frac{\partial g}{\partial X_r}=\begin{bmatrix} \left((v_d-x_1)\dfrac{2R_s X'}{(R_s^2+X'^2)^2}+x_2\left(\dfrac{1}{R_s^2+X'^2}-\dfrac{2X'^2}{(R_s^2+X'^2)^2}\right)\right)\left(\dfrac{X_m}{X_r+X_m}-\dfrac{X_m X_r}{(X_r+X_m)^2}\right) \\ \left(-x_2\dfrac{2R_s X'}{(R_s^2+X'^2)^2}+(v_d-x_1)\left(\dfrac{1}{R_s^2+X'^2}-\dfrac{2X'^2}{(R_s^2+X'^2)^2}\right)\right)\left(\dfrac{X_m}{X_r+X_m}-\dfrac{X_m X_r}{(X_r+X_m)^2}\right) \\ 0 \\ 0 \end{bmatrix}$$

$$\frac{\partial g}{\partial X_m} = \begin{bmatrix} \left((v_d - x_1)\frac{2R_s X'}{(R_s^2 + X'^2)^2} + x_2\left(\frac{1}{R_s^2 + X'^2} - \frac{2X'^2}{(R_s^2 + X'^2)^2} \right) \right)\left(\frac{X_r}{X_r + X_m} - \frac{X_m X_r}{(X_r + X_m)^2} \right) \\ \left(-x_2\frac{2R_s X'}{(R_s^2 + X'^2)^2} + (v_d - x_1)\left(\frac{1}{R_s^2 + X'^2} - \frac{2X'^2}{(R_s^2 + X'^2)^2} \right) \right)\left(\frac{X_r}{X_r + X_m} - \frac{X_m X_r}{(X_r + X_m)^2} \right) \\ 0 \\ 0 \end{bmatrix}$$

$$\frac{\partial g}{\partial T_0} = \frac{\partial g}{\partial A} = \frac{\partial g}{\partial B} = \begin{bmatrix} 0 & 0 & 0 & 0 \end{bmatrix}^T$$

7.5. Appendix E

7.5.1. E-1: Published Journal Papers

E.1. P. Regulski and V. Terzija, "Estimation of Frequency and Fundamental Power Components Using an Unscented Kalman Filter," IEEE Transactions on Instrumentation and Measurement, vol. 61, no. 4, pp. 952-962, 2012

7.5.2. E-2: Published Conference Papers

E.2. P. Regulski, F. Gonzalez-Longatt, P. Wall, V. Terzija, “Induction Generator Model Estimation Using Improved Particle Swarm Optimization and On-line Response to a Change in Frequency”, IEEE Power and Energy Society General Meeting, 2011

E.3. P. Regulski, F. Gonzalez-Longatt, V. Terzija, “Estimation of Load Model Parameters from Instantaneous Voltage and Current”, IEEE International Conference on Fuzzy Systems, 2011